

Clip-on Wings

Final Design report

CHESTA

Version 1.1, January 30, 2018

Blanke, Mathieu	Gudaal, Sakariye
Huistra, Mark	Veldkamp, Lindsay
Keijer, Wessel	Jongbloed, Julienne
Nelissen, Myra	Ponson, Martin
van Zelst, Pieter	van der Heijden, Lars



Distribution List

	Name	Organisation	Version
Student TA	Myrthe Gillis	TU Delft	1.1
Tutor	René van Paassen	TU Delft	1.1
Coaches	Dries Visser	TU Delft	1.1
	Francesco Avallone	TU Delft	1.1
Systems Engineering	Erwin Mooij	TU Delft	1.1
	Wim Verhagen	TU Delft	1.1
1397788	Lindsay Veldkamp	TU Delft	1.1
4143361	Martin Ponson	TU Delft	1.1
4224388	Mathieu Blanke	TU Delft	1.1
4278542	Myra Nelissen	TU Delft	1.1
4308581	Julienne Jongbloed	TU Delft	1.1
4341856	Wessel Keijer	TU Delft	1.1
4353196	Sakariye Gudaal	TU Delft	1.1
4362829	Mark Huistra	TU Delft	1.1
4367251	Pieter van Zelst	TU Delft	1.1
4367286	Lars van der Heijden	TU Delft	1.1

Preface

We are a group of ten dedicated Aerospace Engineering students trying to realise the dream of combining personal air and road transport through detachable hardware(s). This report is the technical design report of the CHESTA. Calculations on the major subsystems have been done and non-technical tasks have been performed such as conducting a business case and determining the operations of the vehicle.

We would like to thank the following people for their time, expertise, and valuable advice. Without them, the report would not compare to what is currently in your possession.

- Dr. ir. René van Paassen
- Dr. ir. Dries Visser
- Dr. Francesco Avallone
- Dr. ir. Wim Verhagen
- Dr. ir. Erwin Mooij
- Myrthe Gillis
- Ir. Joris Melkert
- Dr. Fabrizio Oliviero
- Dr. Christos Kassapoglou
- Dr. ir. Julien van Campen
- Dr. ir. Otto Bergsma
- Dr. ir. Roelof Vos

CHESTA
Delft, January 2018

Summary

Multiple concepts for hybrid vehicles capable of both road and flight transport are becoming a reality. However, through incorporation of both flight and road hardware into one vehicle these designs become inefficient. The aim of this project is to design an alternative strategy for realising optimised hybrid vehicles. The objective of this project is to "Develop a personal transport vehicle suitable for commuter use on which flight hardware can be attached within 5 minutes, by 10 students within 10 weeks". This was derived from the mission statement which was to "Develop a faster and cheaper personal transport vehicle for the European market with detachable flight/road hardware that combines the advantages of road transport with flight capability". From this objective, the three most key requirements are that the vehicle shall have a road and flight configuration, that the flight hardware shall be separable from the road hardware and that the flight hardware shall be attached/detached from the road hardware within 5 minutes.

When analysing the performance of the vehicle, typical flight stages and stalling configurations were investigated in terms of speed and power setting. At cruise speed, the 12 DEP (Distributed Electric Propulsion) propellers in the mid-section of the wing are turned off and folded. However, for take-off and landing configuration, all the propellers are switched on. For fuel use two options are present. E10 gasoline for maximum range, or E85 for decent range, but a 70% lower eco-impact. 122 kW of power is supplied to the 6 outboard motors during cruise. The take-off distance is 450 m and the landing distance is 462 m. Two different propellers were designed and optimized for DEP and cruise conditions. To verify the noise requirements, a propeller noise analysis of the vehicle was carried out, since that is the largest contributor to overall vehicle noise. From that analysis it was concluded that the propeller noise level of the vehicle is 52.3 dBA at 1000 ft, which is low compared to other general aviation aircraft.

The airfoil of the wing was selected using the design lift coefficient of 0.56. The airfoils chosen for the wing and tail are, respectively, the NACA4418 and NACA0012. The wing was designed to have an aspect ratio of 17, a surface area of 8.414 m² and a span of 11.96 m. Using these values, the induced drag and pitching moment coefficients were determined. To investigate the overall efficiency of the aerodynamics of the wing, the lift over drag ratio (L/D) was calculated for each configuration. For cruise, landing and take-off, the L/D is 12.93, 7.74 and 9.48, respectively.

The packaging of the vehicle resulted in the centre of gravity of the operative empty weight of the full configuration to act at 37.4% of the fuselage length at an empty mass of 1174.7 kg. The longitudinal and lateral stability and control of the vehicle were assessed. Due to the large downwash caused by the DEP propellers of the wing, a T-tail configuration was designed to move the tail away from the downwash and make it more effective. A fully-movable horizontal tail was necessary to counter the large lift coefficient and, consequently, the moment created by distributed electrical propulsion. The horizontal and vertical stabiliser were designed with a surface area of 2.42 m² and 1.1 m² respectively.

After analysing the strengths and manufacturing methods of several materials it was found that the wingbox would be made using aluminium (AL7075-T6) with taper in the sheet thickness. Due to the slender wing, the weight of the wing became relatively high at 200 kg. For the skin, the most suitable material was polyester with glass fibres for its specific strength, price and compatibility with a foam or balsa core. For the linkage system, the location where the linkage is established needed to be considered. After investigating this, it was determined that the best place for the linkage would be the rear of the road hardware and the front of the flight hardware. For the linkage the Scharfenberg train coupling was used together with safety pins. The Scharfenberg connection was scaled down to suit the vehicle as it was originally designed for trains.

After the final design is concluded, it is necessary to plan for future research in order to make this concept a reality. There are still uncertainties in how DEP affects the performance and aerodynamics of the concept. Therefore, it is recommended to conduct more low speed tests to properly establish those effects. Computational Fluid Dynamics (CFD) and wing tunnel testing is also recommended to visualise and analyse the fluid flow of the wing. A structural analysis using the finite element method and full scale tests of the major components are also recommended. As the coupling mechanism has never been used in aerospace application, further research into the adaptability and the integration of this mechanism should be performed. As a single-engine Private Pilot License is preferred, recommendations were also made on tests that need to be performed in order to make a case for the airworthiness authorities.

Contents

Distribution List	iii
Preface	v
Summary	vi
List of Symbols & Abbreviations	ix
1 Introduction	1
2 Market Opportunities	3
2.1 Transportation between Large Cities	3
2.2 The Vehicle Concept	6
3 List of Requirements	7
4 System Functionality	11
4.1 Major Functionalities	11
4.2 Technical Resource Allocation	12
4.3 Electrical System Functionality	14
5 Technical Design	17
5.1 Performance and Propulsion	17
5.2 Aerodynamics.	31
5.3 Stability and Control	40
5.4 Materials and Structures	56
5.5 Linkage Design	66
5.6 The Final Product	73
6 Technical Sensitivity Analysis	79
6.1 Effect of Decreased Aspect Ratio	79
6.2 Effect of Increased/Decreased Taper Ratio	81
6.3 Effect of Increased/Decreased C_{Lmax}	81
6.4 Increase/Decrease in Mass	81
7 Operations and Communications	83
7.1 Linkage Operations	83
7.2 Communication during Operations.	84
8 Production Strategy	87
8.1 Part Manufacturing	87
8.2 Assembly	88
8.3 End of Life Cycle and Recycling	88
9 System Sustainability	91
9.1 Cradle to Cradle, Life Cycle Context.	91
9.2 "Well to Wheel" LCA (Fuel Use)	92
9.3 Sustainable Business Model.	92
9.4 Material Choice	93
10 Business Case	95
10.1 Company Vision and Strategy.	95
10.2 Flight Hardware Rental	97
10.3 Chesta Vehicle Connectivity.	98
10.4 Financial Strategy	99

11 Technical Risk Assessment	105
12 Verification and Certification of the Product	107
13 Further Research and Recommendations	109
13.1 Performance and Propulsion	109
13.2 Aerodynamics.	109
13.3 Stability and Control	109
13.4 Vehicle Structures.	110
13.5 Linkage Design	110
13.6 Project Design & Development Logic	110
14 Conclusion	113
Bibliography	115
A Reference Aircraft Data	119
B EcoDesign Strategy Wheel	121
C Work Division	123

List of Symbols & Abbreviations

Table 1: List of symbols

Symbol	Description	Unit
A	Aspect ratio	[-]
A_p	Propeller area	m^2
b	Wing span	m
b	Height of wing box	m
C_D	Drag coefficient	[-]
$C_{D,0}$	Zero-lift drag coefficient	[-]
C_{fe}	Skin friction coefficient	[-]
C_L	Lift coefficient	[-]
$C_{L\alpha}$	Lift curve slope	1°
C_m	Moment coefficient	[-]
C_r	Root chord	m
C_t	Tip chord	m
\bar{C}	Mean aerodynamic chord	m
D	Drag	N
E	Young's modulus	GPa
F_{DEP}	DEP factor	[-]
F_{wake}	Wake factor	[-]
FF	Form factor	[-]
g	Gravity of Earth	m/s^2
h	Height of wingbox	m
I_{xx}	MOI around the x-axis	$kg \cdot m^2$
I_{yy}	MOI around the y-axis	$kg \cdot m^2$
\dot{m}	Mass flow	kg/s
M	Bending moment	Nm
q	Dynamic pressure	Pa
Q	First moment of area	m^3
S	Wing area	m^2
$S_{section}$	Wing section area	m^2
S_{wet}	Wetted skin area	m^2
S_{ref}	Reference wing area	m^2
T	Thrust	N
$t_{1,2}$	Sheet thickness in wingbox	m
T_p	Thrust per propeller	N
V	Shear force	N
V	Speed	m/s or kts
V_2	Increased speed due to the propeller	m/s or kts
V_s	Stall Speed	m/s or kts
V_∞	Free stream velocity	m/s or kts
v	Deflection	m
W	Weight	kg
x_{ac}	Aerodynamic centre position	m
x_{ref}	Reference position	m
x_{cp}	Centre of pressure position	m

Symbol	Description	Unit
α	Angle of attack	$^\circ$ [deg]
δ	Deflection	m
ϵ	Downwash	rad
θ	Angle of deflection	$^\circ$ [deg]
λ	Taper ratio	[-]
Λ	Sweep angle	$^\circ$ [deg]
ρ	Density	kg/m^3
σ	Compressive/tensile stress	MPa
σ_Y	Yield Strength	MPa
τ	Shear stress	MPa

Table 2: List of Abbreviations

Abbreviation	Meaning
0.25C	Quarter-chord
0.5C	Half-chord
AL	Aluminium
ATC	Air Traffic Control
CER	Cost Estimating Relationships
CFRP	Carbon Fibre Reinforced Plastic
CoW	Clip-on-Wing
c.g.	Centre of Gravity
DEP	Distributed Electric Propulsion
DMU	Digital Mock-Up
EIRD	Equipment Installation Requirements Document
EASA	European Aviation Safety Agency
E10	Gasoline, up to 10% ethanol
E85	Bio-Ethanol 85%
FBS	Functional Breakdown Structure
FFD	Functional Flow Diagram
FH	Flight Hardware
FRP	Fibre Reinforced Plastic
GPWS	Ground Proximity Warning System
ICE	Internal Combustion Engine
IoT	Internet of Things
LE	Leading edge
MDT	Mean Down Time
MMH/FH	predicted Maintenance Man Hours per Flight Hour
MTBF	Mean Time Between Failures
MTBM	Mean Time Between Maintenance
MTBUR	Mean Time Between Unplanned Removals
MTOW	Maximum Take Off Weight
MTTF	Mean Time To Fail
MTTM	Mean Time To Maintain
MTTR	Mean Time To Repair
MOI	Moment of Inertia
OEW	Operating Empty Weight
PIREPS	Pilot Reports
PC	Polycarbonate
PEEK	Polyether ether ketone
PEI	Polyetherimide
PEK	Polyetherketone
PET	Polyethylene terephthalate
PP	Polypropene
PPL	Private Pilot License
PVC	Polyvinyl chloride
RDT&E	Research, Development, Testing and Evaluation
RH	Road Hardware
TOP	Take Off Performance
TCAS	Traffic Alert and Collision Avoidance System
SIRD	System Installation Requirements Document
TE	Trailing Edge
100LL	Leaded aviation gasoline "low lead"



Introduction

The dream of constructing hybrid vehicles capable of both road and air transport is finally being realised. Several concepts and designs developed by companies such as PAL-V¹, AeroMobil² and Terrafugia³ already incorporate the ability to transition between road and flight configuration. These designs were conceived by attaching foldable wings or rotors to specifically-designed vehicles in order to make these suitable for both land and air. However, these vehicles have to carry both the road and flight hardware, making them fairly large and inefficient. This limits the vehicles' road capabilities in busier city traffic and when using parking spaces. The flight configuration undergoes compromise as well with non-optimal wingspan as a primary result. To address this problem, an alternative concept is envisioned where the flight hardware is attached to a road vehicle at an airport. This concept removes the need to carry the flight hardware as it is stored at airports until it is used. This improves the vehicle's road capabilities as well as the flight hardware's optimisation. The design of this concept is the aim of this project.

The purpose of this report is to present the final design of the product. This is done by conducting technical calculations of the design parameters. After conducting these calculations, the design will be verified, validated and tested to see if it meets the requirements through a compliance matrix. After that, the non-technical aspect of the project is established such as the operations and logistics of the product, the production strategy, and the business case. This process is then concluded with the certification of the product and further research of the design and recommendations of the product will be discussed regarding post-DSE activities. For marketing reasons, the vehicle will be launched under the name of CHESTA: Car Hybrid Electric Short Take-off Aircraft.

The structure of the report is as follows. Chapter 2 discusses the market opportunities of the product. In Chapter 3, the list of requirements of the product is presented. Chapter 4 describes the major functionalities of the product and discusses how the technical resource budgets are allocated. In Chapter 5, the technical calculations of the design parameters are presented and, in the same chapter, the verification and validation of each technical department is performed, concluding with a compliance matrix to show if it meets the requirements. Chapter 6 presents the technical sensitivity analysis of the design parameters and the drawn conclusions of the potential risks in further phases. Chapter 7 establishes the operations and logistics of the product. In Chapter 8 explains how the product is assembled and produced. Chapter 9 describes how the product takes sustainability into account and in Chapter 10, the business case is conducted. Chapter 11 identifies and ranks the potential risks of the product itself and in the future. The certification of the product is presented in Chapter 12 and further research and recommendations are discussed in Chapter 13. Finally, Chapter 14 presents a summary of the findings from the various chapters in this report.

¹<https://www.pal-v.com/>, (Retrieved on 15 November, 2017)

²<https://www.aeromobil.com/>, (Retrieved on 15 November, 2017)

³<https://www.terrafugia.com/about-terrafugia/>, (Retrieved on 15 November, 2017)

2

Market Opportunities

This chapter explains why the product could play a role in a successful business case. First, section 2.1 explains the current status of travel opportunities between four major European cities. Once the existing travel methods are known, section 2.2 presents the concept that could potentially compete in the existing market and is elaborated on throughout the report.

2.1. Transportation between Large Cities

In order to get an understanding of existing travel options between several European metropolises, research was performed on travel times and corresponding prices between four big cities in Europe: Amsterdam, Berlin, London and Paris. The travel methods considered most suitable for these journeys are transportation by car, train or plane. The results and investigation methods can be found in section 2.1.1. Then, some alternatives are presented, starting with flying car concepts before systems like a hyperloop or personal transportation services are described in section 2.1.3.

2.1.1. Conventional Travel Methods between Large European Cities

If one needs to travel between large European cities, different transportation methods are available. In this section travel between Amsterdam, Berlin, London and Paris is considered with three different types of transportation: by car, train or aircraft. Only four major European cities have been considered for this analysis due to the limited time available. These are chosen because they are part of the most densely populated area of Europe¹ and no mountain chains lie between them. Further analysis of travel times and costs between European cities would be desirable and can be done during the project's next phase.

In table 2.1, the results of a market analysis for conventional transport are shown. For consistency, the data was produced using several guidelines. First, the moment of travel was Wednesday November 29th, 2017 at 13:00. Then, the quickest schedule was always used, unless a significantly cheaper option with reasonable extra travel time, within an hour of the desired departure time is available.

In order to calculate the costs and travel times for road transport, an average family car was considered with a fuel consumption of 17.6 km/L. The fuel consumption was determined by averaging the true operational fuel consumption of twelve fuel efficient average family cars.² The car runs on petrol and the petrol price per liter equals €1.68.³ Google maps was used to find the quickest route and no traffic jams are considered. In France, the autoroutes require toll payments. The toll prices along the previously calculated routes are determined using the calculator presented by the French association of parties involved in the exploitation of the autoroutes (ASFA).⁴ Finally, google maps found that the quickest route to London was through the eurotunnel. Compared to other routes, travelling to London is the most expensive, this is a result of the Eurotunnel⁵ and French toll prices.

¹<http://spainforum.me/europe-population-density-map.html/european-population-and-europe-density-map>, (Retrieved on November 27, 2017)

²<https://www.anwb.nl/auto/besparen/top-10-zuinige-autos/middelgroot-benzine>, (Retrieved on November 27, 2017)

³<http://www.brandstofprijzen.info/>, (Retrieved on November 27, 2017)

⁴<http://www.autoroutes.fr/en/routes.htm>, (Retrieved on November 27, 2017)

⁵[https://www.eurotunnel.com/book/FareFinder/\(0\)](https://www.eurotunnel.com/book/FareFinder/(0)), (Retrieved on November 27, 2017)

Train prices were calculated using the same criteria as mentioned at the start of this section. The results were found by filling in the aforementioned travel information into an online tickets website.⁶ Most trajectories offer departures within an hour from one o'clock. Only from Berlin to London an earlier - 6:25 AM - departure time was chosen, since departure around one o'clock would result in a nineteen hour journey at a higher price of €365.

To calculate the costs and travel times of travelling via aircraft, the ticket website of Skyscanner was used.⁷ Considering the ruling established above, flights were found within an hour of 13:00 on Wednesday the 29th of November, 2017. It was quickly determined that departing at 13:00 is not ideal for most flight trajectories in terms of price, with cheapest tickets typically being offered in the early hours of the morning or late in the afternoon. As one can see, travel time for all distances are under 2 hours. Typically, London is the cheapest destination to fly to, whilst Berlin is the cheapest destination to fly from. The most expensive route to fly around 13:00 is *Paris-Amsterdam*. From the list of times and especially prices, it can be concluded that air transportation between the cities can be relatively cheap, but prices can be impacted significantly by the desired departure time. A flight from Paris to Amsterdam will cost €551 when departing at 12:40, but could only cost €59 when departing at 20:50. Therefore, it is clear that a consideration has to be made with regards to departure time and ticket pricing for certain trajectories, impacting overall freedom and availability of affordable commutes.

Table 2.1: Time and price per conventional transportation method determined 2 days prior to the travel date. The time and prices related to the quickest option, within a reasonable time frame from the desired destination time (13:00).

Destination	Road		Train		Air	
	Time (h:m)	Price (€)	Time (h:m)	Price (€)	Time (h:m)	Price (€)
Amsterdam - Berlin	6:58	63	6:06	132	1:15	522
Amsterdam - London	6:52	182	3:48	261	1:10	60
Amsterdam - Paris	5:49	65	3:18	135	1:15	356
Berlin - Amsterdam	6:58	63	6:30	90	1:30	75
Berlin - London	12:05	213	10:40	170	1:55	69
Berlin - Paris	10:40	114	8:42	240	1:45	154
London - Amsterdam	6:52	182	4:44	217	1:10	53
London - Berlin	12:05	213	9:33	270	1:40	155
London - Paris	5:38	175	2:23	174	1:15	131
Paris - Amsterdam	5:49	65	3:17	135	1:20	551
Paris - Berlin	10:40	114	8:10	180	1:40	173
Paris - London	5:38	175	2:26	185	1:25	129

In table 2.1, one can find that travel times between several big European cities can be less than two hours and cost less than €100. However, if this is the case, why are alternative transportation concepts still being considered? Actually, the road and train transport examples consider travel between city centres. Air transport, on the other hand, considers flight times between the cities' main airports. As a result, real door to door travel times for air transport are significantly higher than shown, since alternative transportation methods have to be used to and from the airport and at least one hour spent at the airport has to be added. These inconveniences were not yet considered in the table, since different transportation methods are preferable for different cities, resulting in varying travel times and prices. So, fast travel between large European cities still requires a journey with multiple transportation methods, resulting in time losses while waiting and changing vehicles. Also, the traveller is still dependent on externally determined departure times, negatively influencing its freedom in choosing departure times.

2.1.2. Existing Flying Car Concepts

So far, only the most common conventional transportation methods have been discussed. From section 2.1.1 it already follows that quick transport between city centres requires a combination of air transport and local methods to and from the airport. Also, no quick personal travel method, which also provides the freedom of determining the departure time is available. Private planes could be an option, but existing tariffs are in a whole other price range and there still is a need for transport to and from airports. From the latter it becomes clear that a single vehicle capable of transporting people privately over longer distances, within a short time, is not yet on the market. To make this possible, several companies are trying to launch such a product. This results in several flying car concepts. Nevertheless, the roads are

⁶<https://www.goeuro.nl/>, (Retrieved on November 27, 2017)

⁷<https://www.skyscanner.nl/>, (Retrieved on November 27, 2017)

yet to be flooded with vehicles that combine the advantages of road transport and flight characteristics. Even though many companies have tried to create a hybrid land and air vehicle, none of them successfully launched a product to this date. However, several companies are trying to induce a radical change. Companies such as PAL-V, Aeromobil, and Terrafugia are paving the way. Despite none of their products being currently available to the public, it is necessary to analyse the competitor's design concepts in order to get familiar with their business cases and the opportunities they envision for the flying car market.

PAL-V

PAL-V is a Dutch start-up with the purpose of constructing a vehicle capable of both flying and driving. By means of a gyroplane principle, the company promotes their PAL-V Liberty to create lift by its wind-powered rotor. By combining this gyroplane principle with a three-wheel automotive design, the PAL-V Liberty sets itself apart significantly. Through the retracting rotor blades, the transition vehicle also does not exceed the typical dimensions of a regular car. Two versions of the PAL-V Liberty, the Sport edition and the Pioneer edition, are available for pre-order with a predicted delivery in 2019. The Sport edition is predicted to be turning heads at a price tag of €299,000, while the Pioneer Edition (of which only 90 will be produced) will be delivered for €499,000.⁸ Where the Pal-V strikes out, however, is in aspects such as fuel efficiency and aesthetics. With a fuel efficiency of 7.6 l/100km and 18.6 l/100km for car and flight configuration respectively, the vehicle's fuel efficiency will not meet the project requirements stated in chapter 3. Furthermore, the new driving technology developed for the car configuration is working and complies with regulations.

Aeromobil

Another European company which is seeking market entry is Aeromobil. Their product, Aeromobil 4.0, is a hybrid vehicle with a sleek appearance and retractable wings to ensure flight capabilities. However, due to its retractable wings the automotive dimensions are not ideal with a length of 5.9m. This length of 5.9m constitutes to difficult handling in tighter road situations, such as driving through a busy city. The previous version's prototype was successful in all testing stages, resulting in the desire to commercialise the Aeromobil 4.0. Production will be up to 500 units, which are projected to be delivered to the public by 2020. Similarly to the PAL-V Liberty, the hybrid vehicle can already be pre-ordered. Furthermore, selling the Aeromobil 4.0 at a predicted price of €1.2 to €1.5 million creates the desired prestigious appearance⁹. This price is, however, far beyond what is conceived to be a competitive price. With already up to 5 times as expensive as the Pal-V, it is the question whether the more aesthetically appealing and fuel efficient Aeromobil 4.0 will actually have a market impact.

Terrafugia

Terrafugia originated from an MIT student initiative and is currently in the process of producing two practical flying cars. The first is "The Transition", which is a car with the appearance of a plane. The wings are folded and compacted to the side of the 'fuselage'. With a length of approximately 6 meters, the Transition does not acquire the sleek and prestigious stigma surrounding its competitors. Although pre-ordering is optional with a refundable payment of \$10,000, Terrafugia has yet to decide on a product price. The second proposed flying car, the TF-X, has barely left the drawing board. The design is much more appealing than its predecessor, with its premium feature being, not having to depend on airport infrastructure. Not needing a take-off/landing strip would be an incredible innovation for the automotive/aeronautical hybrid industry, yet realisation of the design will remain something for the future.

2.1.3. Alternative Concepts

After having discussed conventional transportation methods and analysed certain competitors and their transitional car/aircraft vehicles, it is interesting to evaluate the possible future of personalised air transportation. Certain companies are conceptualising amazingly innovative ideas, hoping to realise them as soon as technology allows. The characteristic shared by these futuristic concepts is the desire to create a taxi service similar to the service Uber supplies. Using mobile applications, companies such as Airbus Pop.Up, Airbus CityAirbus, Lilium, and Uber's Elevate, are trying to incorporate taxi services with both car and flight transportation. Using one's phone, one can request a vehicle at any point and time. Through vertical take-off/landing (VTOL) capabilities and often proposed automation, the vehicle helps to decide the fastest route and increases possibilities regarding employability in city centers. The public will not require personally owned vehicles anymore, because these new transportation services provide personal and safe transportation as efficiently as desired.

⁸<https://www.pal-v.com/en/reserve-your-pal-v>, (Retrieved on November 21, 2017)

⁹<https://www.aeromobil.com/>, (Retrieved on November 21, 2017)

This, however, is still a concept which is far from being realised. Taking Uber's Elevate for example, the concept of depending on VTOL capabilities to provide transport within city infrastructures is still hindered by numerous market feasibility barriers. The most critical challenges, according to Holden and Goel (2016), lie in some of the following points:

- **The Certification Process.** Certification of conceptually new aircraft concepts, such as VTOL aircraft, is historically slow. To become compliant with the US Federal Aviation Administration (FAA) and European Aviation Safety Agency (EASA) regulations will, therefore, be a tedious process.
- **Battery Technology.** Even though electric propulsion is likely to be the most preferred source of propulsion, certain problems still exist with the energy source. The specific energy of a battery system is still, to this day, insufficient for longer commutes. Furthermore, current charge rates will not be able to support the desired frequency of commuting.
- **Infrastructure in Cities.** This operational barrier is quite present, with current cities lacking sufficient locations to support VTOL fleets. Before such fleets can become realised, the infrastructure has to be constructed. Heliports have to be introduced in the right locations, with space available for charging stations and be easily accessible from the street.
- **Vehicle Efficiency.** With current market technologies, helicopters are the closest form of technology to realise the VTOL discussed by Uber. They are, however, not energy efficient, becoming economically unfeasible when constructing a larger fleet. Introducing Distributed Electric Propulsion (DEP) technology, is listed as a viable option by Uber, but still not commercially available and applicable.

The Airbus Pop.Up concept will also be hindered by these barriers, with additional barriers introduced due to its automated, self-sufficient vehicle concept design. Complying with regulations for a vehicle both driving and flying self-sufficiently will almost definitely not be fulfilled in the upcoming decade. The alternate vehicle concept which is currently furthest along within its design stage is the Lilium.¹⁰ This vehicle will be confronted with multiple market barriers listed above as well, but has managed to introduce Distributed Electric Propulsion in its flight stage. Testing of the vehicle has already been successful, with the designers purely focusing on the vehicle's flight capabilities for the time being. The Lilium strives to design an air taxi which can take-off from a proximate landing pad, is all-electric with a range of approximately 300 km, and will fly with a speed of 300 km/h with minimum noise. The time-line presented by the Lilium engineers aims to launch the first commercial flight in 2025. However, although the concept is promising and innovative, it is yet the question to see if the time-line will be followed and achieved. Furthermore, a limiting aspect to the Lilium lies in its inability to supply a customer with road transportation. If the Lilium's flight abilities can be incorporated into a vehicle capable of road transportation as well, that would be ideal.

2.2. The Vehicle Concept

The revolutionary concepts discussed, however, are far from optimised or will most likely not be realised for another decade or so. Nevertheless, section 2.1.1 mentioned that the concept of a personalised hybrid road and flight vehicle has the potential play a role in existing market. Its advantages, such as door to door travel, personal travel and limited dependency on travel companies make it a product worth investigating. If air and road transport with personally owned vehicles is to be achieved, the practical disadvantages of the existing concepts have to be solved. That is why, for this project, detachable flight/road hardware is considered.

From section 2.1, it becomes clear that currently no systems with detachable road/flight hardware are being prepared for market entry. Existing flying car concepts tend to limit themselves to what the name suggests, one vehicle with all flight and drive hardware integrated during all phases of operation. During this project, however, such systems are not considered feasible for daily commuting operations due to inefficiencies of carrying hardware for both configurations. Flight hardware will be offered by a rental company at the airport and an hourly tariff has to be paid. The vehicle has to be sustainable and in order to compete with the earlier mentioned transportation methods, its range should be large enough to travel between large European cities. More details about the design and its requirements will be presented in chapter 5 and chapter 3, respectively.

¹⁰<https://lilium.com/>, (Retrieved on November 27, 2017)

3

List of Requirements

This chapter discusses the stakeholders and the requirements that flowed from them. The stakeholders that were deemed important for the vehicle at hand are listed below:

- **Client, TU Delft tutors:** provide the initial requirements.
- **Users, customers and occupants**
- **Governmental bodies**, such as the European Aviation Safety Agency (EASA) and European Council (EC): set requirements in the form of regulations and safety standards.
- **Market competitors**, such as PAL-V, AeroMobil, train network, regular airlines etc.: help with making sure the vehicle can be economical and compete in the market.
- **Flight hardware leasing firm:** provide more market related requirements.
- **Airports and Air Traffic Control (ATC):** they have a say on vehicle functionality and operations on or near airports.
- **Pedestrians, general public and the community:** set high safety, noise and emissions requirements, mostly enforced and represented by governmental regulations.
- **The environment:** forces the vehicle to be sustainable.

The requirements that flowed from these stakeholders have been put together into one organised list. The requirements are ranked into key requirements and driving requirements, shown in table 3.1.

Table 3.1: All Key- and Driving-Requirements

Key-Requirements	Driving-Requirements
CoW-Sys-Tech-1.1	CoW-Sys-Tech-1.3
CoW-Sys-Tech-1.2	CoW-Sys-Tech-3.1
CoW-Sys-Tech-1.4	CoW-Sys-Tech-3.2
CoW-Sys-Tech-2.1	CoW-Sys-Car-3.1
CoW-Sys-Tech-2.2	CoW-Sys-Air-4.1
CoW-Sys-Tech-3.4.0	CoW-Mis-Sus-1.Air
CoW-Sys-Car-1.1	CoW-Mis-Sus-3.Car
CoW-Sys-Car-2.1	CoW-Mis-Sus-3.Air
CoW-Sys-Car-2.2	CoW-Mis-Sus-5.1
CoW-Sys-Car-3.2	CoW-Mis-Sus-5.2.Car
CoW-Sys-Car-3.3	CoW-Mis-Sus-5.2.Air
CoW-Sys-Air-1.1	CoW-Mis-Mar-1.1
CoW-Sys-Air-2 (all)	CoW-Mis-Mar-2.1
CoW-Sys-Air-3 (all)	
CoW-Mis-Sus-1.Car	
CoW-Mis-Sus-2.Car	
CoW-Sys-Mar-2.2	
CoW-Sys-Mar-2.3	
CoW-Sys-Mar-3.1	

The list has been organised in the following way: First starting with the project name, Clip-on-Wings (CoW). After this point it is split up in to two sections. The systems (Sys) section, which includes all technical requirements, and the mission (Mis) section, which include all non-technical and sustainability requirements. The full list of requirements are shown below:

- CoW-Sys-Tech-1.1:** The vehicle shall have a road configuration and flight configuration.
- CoW-Sys-Tech-1.2:** The flight hardware shall be separable from the vehicle.
- CoW-Sys-Tech-1.3:** The flight hardware shall be attached/detached in 5 minutes or less.
- CoW-Sys-Tech-1.4:** Conversion shall not require manual labour.
- CoW-Sys-Tech-2.1:** Redundant and/or fail-safe links shall be employed for the linking of flight and road hardware.
- CoW-Sys-Tech-2.2:** The vehicle, in both configurations, shall have emergency facilities.
- CoW-Sys-Tech-3.1:** The minimum payload capacity shall be 360 kg.
- CoW-Sys-Tech-3.2:** The vehicle shall have a minimum capacity for at least 3 occupants, including the user.
- CoW-Sys-Tech-3.3:** The occupants shall have a minimum seat spacing¹ of 50.8 cm.
- CoW-Sys-Tech-3.4.0:** The vehicle shall have a minimum luggage capacity² of 3 pieces of 0.55-0.4-0.23 m³ each; 0.152 m³ for all occupants combined.
- CoW-Sys-Tech-3.4.1:** The vehicle shall have the ability to secure the luggage during operation.
- CoW-Sys-Tech-3.5.0:** The vehicle shall have an enclosed cabin.
- CoW-Sys-Tech-3.5.1:** The vehicle shall have locks.
- CoW-Sys-Tech-3.5.2:** The vehicle shall have secure windows.
- CoW-Sys-Car-1.1:** The vehicle, in road configuration, shall meet road safety requirements in compliance with Directive 2007/46/EC amendment M29.
- CoW-Sys-Car-2.1:** The vehicle, in road configuration, shall have a driving range of at least 200 km.
- CoW-Sys-Car-2.2:** The vehicle, in road configuration, shall have a maximum road speed of at least 140 km/h.
- CoW-Sys-Car-3.1:** The vehicle, in road configuration, shall be no longer than 4.5 m.
- CoW-Sys-Car-3.2:** The vehicle, in road configuration, shall be no wider than 2.55 m (in compliance with Regulation (EU) No 1230/2012).
- CoW-Sys-Car-3.3:** The vehicle, in road configuration, shall be no taller than 4.00 m (in compliance with Regulation (EU) No 1230/2012).
- CoW-Sys-Car-4.1:** The vehicle, in road configuration, shall be operable under a standard EU driver's license.
- CoW-Sys-Air-1.1:** The vehicle, in flight configuration, shall be safe to fly, in compliance with airworthiness requirements CS-23 amendment 5.
- CoW-Sys-Air-2.1:** The vehicle, in flight configuration, shall have a flight range of 300 NM (excluding reserves).
- CoW-Sys-Air-2.2:** The vehicle, in flight configuration, shall have a cruise speed of 160 kts at maximum payload weight.
- CoW-Sys-Air-2.3:** The vehicle, in flight configuration, shall have a maximum service ceiling of 10000 ft.
- CoW-Sys-Air-2.4:** The vehicle, in flight configuration, shall take off and land with a runway length of 450 m at sea level, no wind, at maximum takeoff weight.
- CoW-Sys-Air-3.1:** The vehicle, in flight configuration, shall include control augmentation or autopilot functionality.
- CoW-Sys-Air-3.2:** The vehicle, in flight configuration, shall include Traffic Collision Avoidance System (TCAS).
- CoW-Sys-Air-3.3:** The vehicle, in flight configuration, shall include ground proximity warning functionality (GPWS).
- CoW-Sys-Air-4.1:** The vehicle, in flight configuration, shall be operable under a standard Private Pilot's License (single-engine piston fixed wing aircraft) / Light Aircraft Pilot's Licence (PPL/LAPL).
- CoW-Mis-Sus-1.Car:** The vehicle, in road configuration, shall use no more than 141.0 MJ worth of fuel per 100 km or 98.7 MJ per 100 km if using electrical propulsion.
- CoW-Mis-Sus-1.Air:** The vehicle, in flight configuration, shall use no more than 246.8 MJ worth of fuel or electrical energy per 100 km.
- CoW-Mis-Sus-2.Car.0:** The vehicle shall adhere to road emission standards.

¹<https://www.seatmaestro.com/airlines-with-the-most-seat-space-in-economy-class/>, (Retrieved on 22 November 2017)

²<https://www.skyscanner.net/news/cabin-luggage-guide-hand-baggage-sizes-and-weight-restrictions>, (Retrieved on 22 November 2017)

- CoW-Mis-Sus-2.Car.1:** The vehicle, in road configuration, shall emit no more than 95.0 g/km CO₂ in compliance with European 2021 targets.
- CoW-Mis-Sus-2.Car.2:** The vehicle, in road configuration, shall emit no more than 1.0 g/km CO in compliance with Euro 6 emissions regulation (EU) No 715/2007.
- CoW-Mis-Sus-2.Car.3:** The vehicle, in road configuration, shall emit no more than 0.08 g/km NOX, in compliance with Euro 6 emissions regulation (EU) No 715/2007.
- CoW-Mis-Sus-2.Car.4:** The vehicle, in road configuration, shall emit no more than 0.005 g/km of fine atmospheric particle matter, in compliance with Euro 6 emissions regulation (EU) No 715/2007.
- CoW-Mis-Sus-3.Car:** The vehicle, in road configuration, shall have a maximum vehicle noise ($L_{A,max}$) of 75 dBA, in compliance with regulation (EU) No 540/2014.
- CoW-Mis-Sus-3.Air:** The vehicle, in flight configuration, shall have a maximum vehicle noise ($L_{A,max}$) of 72 dBA, in compliance with 14 CFR Part 36.
- CoW-Mis-Sus-4.1.0:** A cradle-to-cradle concept shall be used.
- CoW-Mis-Sus-4.1.1:** 5% of the vehicle shall be reusable by mass for use in other aerospace applications.
- CoW-Mis-Sus-4.1.2:** 75% of the vehicle shall be recyclable by mass for use in lower than aerospace grade applications.
- CoW-Mis-Sus-4.1.3:** 80% of the remaining material shall be incinerated for heat recovery (Thermal recycling).
- CoW-Mis-Sus-4.1.4:** The vehicle or operational facility shall use some form of sustainable energy.
- CoW-Mis-Sus-4.1.5:** The product shall comply with the Reduction of Hazardous Substances (RoHS) regulations.
- CoW-Mis-Sus-4.2:** The vehicle shall be designed with decommissioning in mind.
- CoW-Mis-Sus-4.3.0:** The vehicle materials, in road configuration, shall be re-used.
- CoW-Mis-Sus-4.3.Car:** The vehicle, in road configuration, shall be recycled in compliance with Directive 2005/64/EC Article 7.
- CoW-Mis-Sus-5.1:** The vehicle shall have an eco-cost no higher than 5,000 € during production.
- CoW-Mis-Sus-5.2.Car:** The vehicle, in road configuration, shall have an eco-cost no higher than € 3.98 per 100 km.
- CoW-Mis-Sus-5.2.Air:** The vehicle, in flight configuration, shall have an eco-cost no higher than € 6.96 per 100 km.
- CoW-Mis-Mar-1.1:** The purchase cost of the road vehicle shall not exceed €80,000.
- CoW-Mis-Mar-1.2:** The car shall last 20 years whilst driving 10,000 km a year, amounting to an average of 27.4 km a day.
- CoW-Mis-Mar-2.1:** The lease cost of the flight hardware shall not exceed €120 per flight hour.
- CoW-Mis-Mar-2.2:** The vehicle infrastructure model shall be supported by an analysis of the logistics for the lease or ownership of the flight hardware.
- CoW-Mis-Mar-2.3.0:** The flight hardware shall have a minimum availability rate of 80% during peak times (Mon-Fri: 7am-9am, 5pm-7pm as well as peak days during summer holidays such as Black Saturday).

The following requirements still have TBD design values as this needs to be determined in the next stage of the development of the product.

- CoW-Mis-Mar-2.3.1:** The vehicle, in flight configuration, shall have a minimum dispatch reliability of <TBD> %.
- CoW-Mis-Mar-2.3.2:** The vehicle, in flight configuration, shall have a Mean Time Between Unplanned Removals (MTBUR) of <TBD> hours.
- CoW-Mis-Mar-2.3.3:** The user or leasing firm shall perform a minimum of <TBD> Pilot Reports (PIREPS) for every flight.
- CoW-Mis-Mar-2.3.4:** The vehicle, in flight configuration, shall have a minimum delay/ cancellation ratio of <TBD>.
- CoW-Mis-Mar-2.3.5:** the vehicle, in flight configuration, shall have a maximum of <TBD> in-flight shut-downs.
- CoW-Mis-Mar-2.3.6:** The vehicle, in flight configuration, shall have a minimum communication link availability of <TBD>.
- CoW-Mis-Mar-2.3.7:** The vehicle, in flight configuration, shall have a Maximum Time To Failures (MTBF) of <TBD> hours.
- CoW-Mis-Mar-2.3.8:** The vehicle, in flight configuration, shall have a Maximum Time To Repair (MTTR) of

<TBD> hours.

CoW-Mis-Mar-2.3.9: The vehicle, in flight configuration, shall have a maximum fail rate of <TBD> failures/hour.

CoW-Mis-Mar-2.3.10: The vehicle, in flight configuration shall have a maximum Mean Down Time of <TBD> hours.

CoW-Mis-Mar-2.4: The flight hardware shall have a lifespan of 29,200 flights in 20 years, amounting to an average of 4 flights a day.

CoW-Mis-Mar-3.1: The vehicle shall look cool and be attractive for customers, assessed in accordance with a survey conducted amongst 'potential customers'.

4

System Functionality

Following the exploration of the opportunities and setting-up of important requirements comes the listing of what the system should be able to do and how it will be done. This chapter will first recap major functionalities the system should have. These will be presented in a Function Flow Diagram (FFD) in section 4.1. Furthermore, section 4.2 will present the technical resource allocation, which will show the mass breakdown of the system. Finally, the electrical system of the product is presented in section 4.3.

4.1. Major Functionalities

The system must be able to perform multiple tasks. To identify these tasks, a FFD was set-up. The chronological level 1 and 2 functions can be seen in fig. 4.1. The four major functionalities that the system must be able to perform are:

- 1.0 **Provide road transport**
- 2.0 **Provide transformation to flight configuration**
- 3.0 **Perform flight operations**
- 4.0 **Provide transformation to road configuration**

Each major functionality also has multiple sub-functions which must be designed for. Blocks 1.0 and 3.0 contain all operations associated with driving and flying. Blocks 2.0 and 4.0 are two specific functions that will set this system apart from any other systems. In general these two functions will be very similar, with the exception of 2.2 and 2.3 being reversed at 4.1 and 4.2. These are the linkage functions of the system. Block 2.0 starts with a receive information function and starts the linkages step. This information tells the user when and where he/she can find an available FH to link with. The next step is the linkage itself. More on this specific step can be found in chapter 7. After the linkage the system verifies if the link was successful, hence the GO and NO-GO. If a go is given, there is an option to fuel/charge the vehicle, if not from that point on it is considered an aircraft and can go on to block 3.0. If a no-go is given, maintenance will come in to fix the issue and redo step 2.3. Block 4.0 starts with this same verification block with a GO or NO-GO step. After flight, the vehicle is checked for damage and whether the FH can be removed safely. If not, maintenance is called in to help. Step 4.2 will be very similar to 2.2 (see chapter 7 for further details). All points between 2.2 and 4.2 is also where the FH is part of the vehicle. After the detachment, an option to fuel/charge is given again. From this point the vehicle can flow to either point 1.0 or 1.2 and is considered a car.

There are also some other top level functions which occur the whole time. These are named level 0 functions and there are also four of those. They are:

- 0.1 **Vehicle health monitoring:** This should identify issues, display the vehicle health to crew and appropriate stakeholders and transmit the vehicles health status to the maintenance department.
- 0.2 **Provide communications:** This includes all vehicle communications, both internal (intercom) and external, such as with the Air Traffic Control (ATC) and other vehicles.
- 0.3 **Navigate:** Provide both GPS on the road as well as in flight. However, this function also includes all primary road and flight meters and give the crew a situational awareness.
- 0.4 **Provide safety:** All modern car and aircraft safety features should be present.

Note that these functions are only active while there is at least one person on-board of the vehicle in either configuration. Function 0.1 is also of high importance at both system verification steps (2.3 and 4.1), indicated with the M in fig. 4.1. Here maintenance is needed if linkage fails and the vehicle cannot continue to operate as normal.

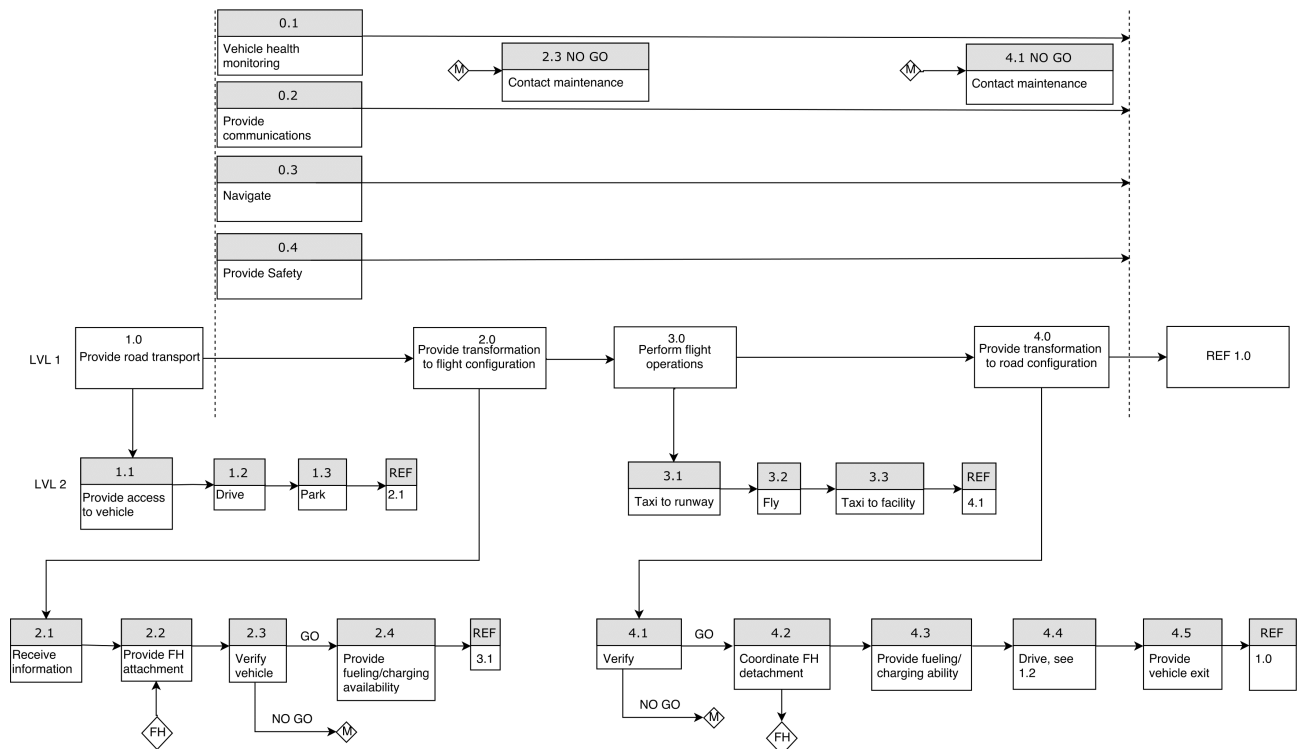


Figure 4.1: Functional Flow Diagram of the 2 uppermost levels

4.2. Technical Resource Allocation

In this section, the technical resources are allocated, tracked and managed. The budgets are evaluated at two points in the design process. The major budget is mass, power is also discussed.

4.2.1. General Mass Estimation Procedures

During this project, mass is estimated with varying methods, with increasing amount of accuracy. Before the midterm, a so-called Class I estimate was made. In the second half of the project, most estimates are replaced by Class II, or Class III methods. An overview is made of the different classes, as taught in LaRocca (2017c):

Table 4.1: Explanation of Class I, II, III methods

Stage	Methods	Returns
Class I: Early conceptual	Statistics and range equation.	MTOW, OEW, M_{fuel}
Class II: Conceptual stage	Statistics based on simple airplane geometry.	Weight of (sub) systems
Class III: Preliminary design	Aerodynamic analysis and structural sizing.	Increased accuracy

Using the Brequet range equations Vos et al. (2017), with a statistical regression from Roskam (1997a), and a penalty for the road hardware of 200 kg, it was estimated that the aircraft would receive a MTOW of around 1500 kg. All components were designed to withstand flight loads at 1500 kg initially, but as it became apparent that the aircraft would weight approximately 1650 kg, this value was raised to an absolute maximum of 1600 kg, to drive the design to be more efficient. This 50 kg difference has to be overcome by using innovations with regard to materials and electronics.

4.2.2. Contingency Management

When assigning the departments with mass budgets for their (sub)systems, a contingency of 20% was initially put into place. As the design matured, this contingency allowance was decreased to 10%. However, the contingency was not sufficient, since some departments went past their contingency allowance, and the total mass passed the 1600 kg maximum. As can be seen in table 4.2. The power budget increased from 100 kW to 130 kW, mainly due to increased zero-lift drag from the first order estimate.

4.2.3. Airframe

Table 4.2: Mass breakdown at low and higher order accuracy

	Initial mass [kg]	Class	Final estimate [kg]	Class
Powerplant/drivetrain	230	II	261	III
Car without propulsion	520	I	453	II/III
Extra for DEP	90	III	96	III
Wing	160	II	200	III
Empenage	44	I	31	II
Fuselage behind car	60	-	72	III
Linkage/reinforcement	20	-	18	III
DEP naceles	17	II	17	II
Control + Avionics	30	I	30	I
E85 fuel (after taxi)	135	I	128	I/II
Payload	360		360	
Total MTOW* [kg]	1666		1666	

*The fact that MTOW is the same for both estimates is a coincidence.

The powerplant was sized using a power requirement of 100 kW continuous initially, and 130 kW updated, together with the extra mass for DEP, this is further elaborated upon in section 4.2.5 The car was initially estimated to have a 750 kg empty mass, which is approximately 25% lighter than a compact car, for details, see section 4.2.4. The wing was estimated using a Class II formula from Raymer (1999), using MTOW, wing area (S), aspect ratio (A), and thickness to cord ratio (t/c). This, however, turned out to produce too low an estimate, the actual wing design, with larger t/c, turned to be 25% heavier (for the design, see section 5.4.2). This was expected, since this wing would otherwise be remarkably light for its aspect ratio. Raymer probably did not have aircraft with aspect ratios far above 10 in his dataset. The empenage and control/avionics were estimated using averages from Kundu (2010). Fuel was estimated using the Brequet range equations, with a correction for Ethanol use.

4.2.4. Car Mass Budgets

Standard mass breakdowns for cars were initially taken from Lutsey (2010) and compared to the aircraft nomenclature and relative weights from Kundu (2010).

Table 4.3: Car mass breakdown at low and higher order accuracy.

	Initial [kg]	Final [kg]	Includes:
Chassis group	210	207	Chassis, wheels, brakes, suspension, steering, battery enclosure.
Other	23	23	Lights/signalling, sensors, seatbelts.
Body	195	161	Structures, attachment to FH, doors, glass.
Interior	60	60	Seats, instruments and airconditioning.
Contingency	30	0	
Drivetrain	233	263	See section 4.2.5
Total [kg]	750	714	

Table 4.4: Body and chassis mass

Body	mass [kg]	Chassis	mass [kg]
middle truss	27	Structure	97
aft truss	30	Wheels	66
glass front	20	Suspension	in structure
"closures"	60	Brakes	44
extra skin	24	Steering	in structure
		Battery box	20
Total [kg]	161		207

The "structure" is the front and lower part of the chassis. The trusses with the skin form the car body. No mass is added for the bumper. The middle and aft truss have been designed as in section 5.4.4. The glass and skin mass were estimated from the uncovered area. The closures are the doors, including glass and the hood. This was 80 kg for the

light SUV Lotus Cars (2010), with 2 doors less this is estimated to be 60 kg. The structure and brakes are also adapted from Lotus Cars (2010). For a 15" wheel, the tire and rim weigh both in the order of 8 to 8.5 kg each, adding up to 66 kg for the four wheels. Finally, the battery box is estimated to weigh 20 kg.

4.2.5. Power and Propulsion Components

Table 4.5: Drivetrain and DEP component mass

Drivetrain component	Mass [kg]	DEP component	Mass [kg]
Engine, 130 kW continuous	110.5	Mass of 6 outboard engines. 24 kW each.	18
10 kWh battery cells at 333 Wh/kg	30	Mass of 12 remaining engines. 8 kW each.	12
Generator	25.7	Mass of engine controllers	12
Electromotors, 2x, RWD	25	Propellers 1 kg and 2 kg.	24
Inverters generator	6.5	Wiring+overall DEP control (20+10)	30
Driving controller	5		
Tank, 200 L	25		
Fuel lines system	3		
Engine control (incl. cooling)	30		
Total [kg]	261	Total [kg]	96

The engine, generator and battery mass have been sized in section 5.1.14. The mass of the drivetrain and DEP components are presented in table 4.5. The inverter is scaled at 20 kW/kg. (Petermaier, 2015) The engine control is from a Class I estimate from Kundu (2010). The fuel lines are from a Class II estimate, the tank is a 200 L mobile diesel tank. The DEP engines are rated approximately 5 hp/lb (8 kW/kg) and the controllers 15 hp/lb (25 kW/kg.) (Moore, 2012) The propellers are estimated to add up to 24 kg. For reference, the Cirrus SR22 has a 27 kg constant-speed propeller without de-ice. The wiring and overall DEP controller (fly-by-wire system) are the hardest to estimate. If normal high current wires (the common red 400V AC socket with multiple phases) are used, the mass would be almost 40 kg, it is expected that lightweight DC design can almost cut this in half.

4.3. Electrical System Functionality

In this section, the electrical system of the product is presented. This is done by illustrating in detail its electrical equipment and their interactions in section 4.3.1 and describing the data handling block diagram in section 4.3.2.

4.3.1. Electrical System

In fig. 4.2, the electrical block diagram of the product is presented. In this figure, it can be seen that the electrical system is split into 3 sections, namely the flight hardware, road hardware and the linkage. This shows that the linkage defines the connection between the two hardware configurations which makes sense as the flight hardware is detachable and not fixed. In this section, the flight and road hardware will be discussed. The linkage will be discussed in detail in section 4.3.3.

The flight hardware consists of the 18 propellers, each containing of a motor and a controller. All of the propellers on each side are then connected to a primary and secondary motor control box. This is done to have full control of each propeller for the ease of use of changing it's settings to comply with the right flight configuration as explained in chapter 5. The secondary box is also added for redundancy. All of this is connected to the linkage.

For the road hardware, the battery and the internal combustion engine (ICE) are present. They are connected to the battery controller and the AC-DC rectifier respectively. For redundancy, the battery is also connected to a DC-DC converter. The power system is connected to the engine controller for power, which in turn is then connected to the wheel motors for movement. The road hardware also consists of the avionics and navigation controller. The power system is also connected to the vehicle system, which consists of lighting, entertainment, TCAS, GPWS, autopilot, driving equipment etc. Unlike the flight hardware, the road hardware is functionable by itself as it has the power source. However, when connected to the linkage, and therefore the flight hardware, the power can flow through and make the flight hardware function as well.

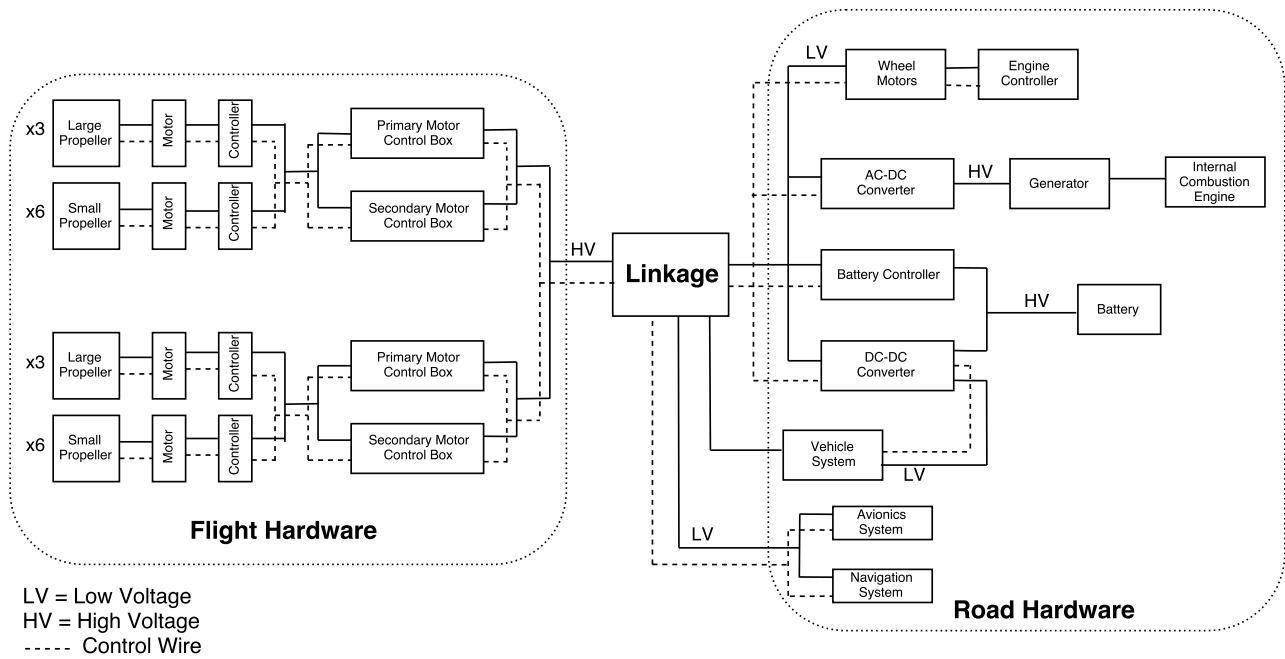


Figure 4.2: Electrical Block Diagram

4.3.2. Data Handling System

The data handling block diagram shown in fig. 4.3 was used to schematically show the relations between different parts of the vehicle. The diagram is divided in a flight hardware part and a road hardware part.

The input of a pilot on the cockpit controls should be registered by the flight computer which then translates that signal to the flight controls, in this case the aileron, stabiliser, rudder and flaps. The same logic applies to the motors, as a change in thrust needs to be transmitted through the flight hardware to the engine controller and the engine and to the motor controller and motors. Furthermore, health data from the motors and flight controls should be processed back to the pilot. Moreover, sensors such as angle of attack vanes and pitot tubes, send data to the flight computer which needs to be communicated to the pilot. Finally, the autopilot system should be turned on when it receives a signal from the flight computer. In the diagram also warning systems, navigation systems and radio are linked to the flight computer. Warning systems are the TCAS and GPWS. Moreover, sensors send data about the fuel level and engine temperature to the flight computer.

The same logic applies to the car. The carputer registers input from the driver and sends this data to the battery controller, engine controller and wheel motors. The carputer receives health data from these parts as well. Important information such as the charge of the battery and the speed of the vehicle needs to be communicated to the driver. Furthermore, sensors that register the fuel level should be connected to the carputer.

The sensors for linkage is the only link between the flight hardware data handling system and the road hardware data handling system, this is to reduce the chance that a stray signal from the road hardware could interfere with the datastreams of the flight hardware and produce misleading data. The linkage sensors send data to the carputer and consequently the driver during the linkage process. Once the linkage is completed they will send a signal to the flight hardware, completing the linkage.

4.3.3. Electrical Linkages

In conventional cases, there is only one electrical system for the aircraft. This case is different as there are two systems, the road and flight hardware. This brings the linkage between the two. As later stated in section 5.5, a Scharfenberg train coupling mechanism is used for the front part of the linkage lug. Within train travel and technology there is a lot of know-how of how to make self connecting links. Having used this possible coupling system for mechanical purposes why not also look into the electric/electronic potentials. Although it advantages in preventing movement in the free axis, forwards and backwards, and it use in power transfer between the two vehicle parts, it is unsure if these couplings can be scaled-down to the right size for this vehicle.

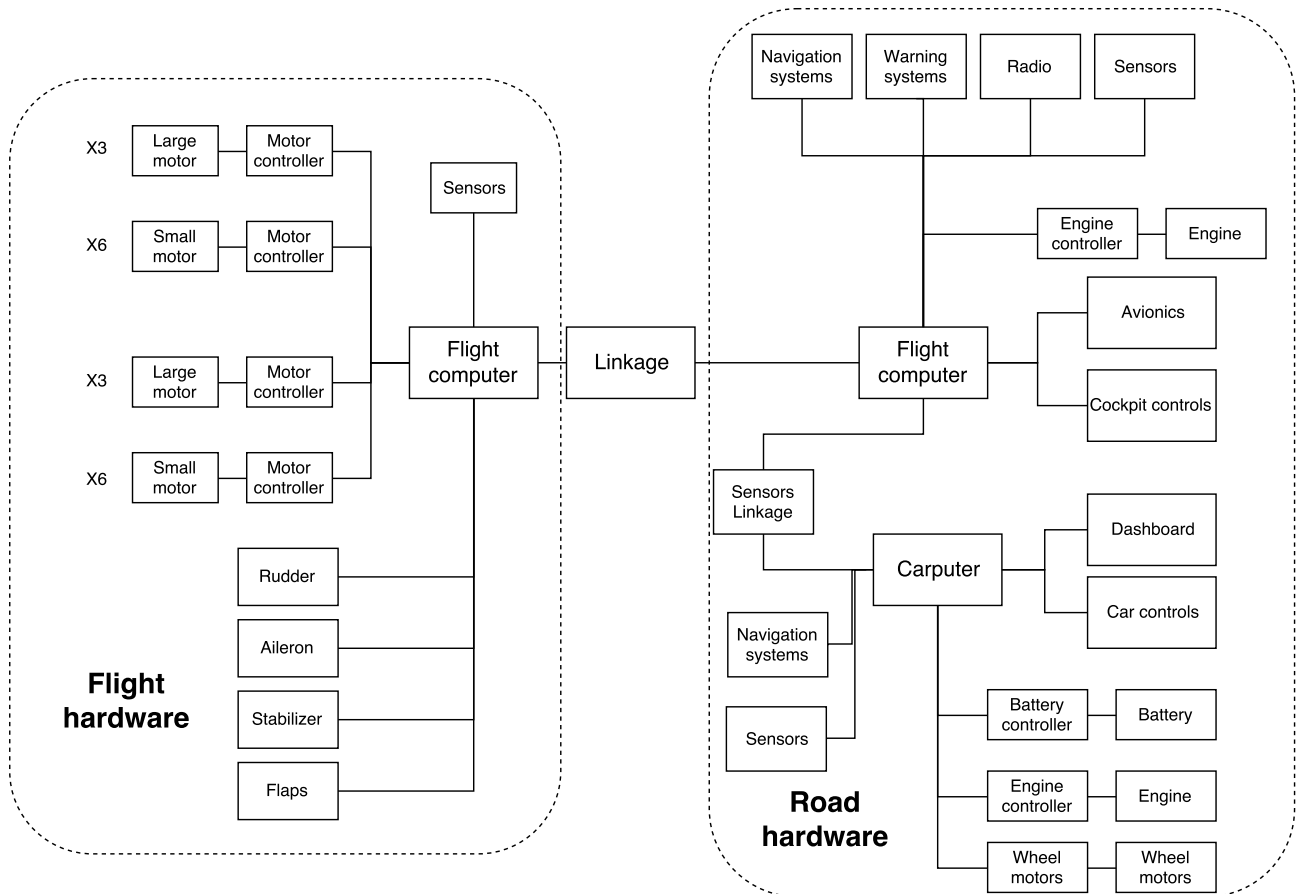


Figure 4.3: The data handling block diagram

5

Technical Design

In this chapter, the technical parameters of the design are calculated and presented. This is split up into five different departments which are: Performance and propulsion (section 5.1), aerodynamics (section 5.2), stability and control (section 5.3), vehicle structures (section 5.4), and finally linkage design (section 5.5). After the design parameters are calculated, the final design is presented in section 5.6 along with a compliance matrix to check if the product meets the requirements.

5.1. Performance and Propulsion

In this section the flight performance is analysed and compared to requirements from the customer and EASA. Novelty of the design requires the modification of standard assumptions and formulas, and special attention is paid to the failure of critical components to ensure the design remains safe. In the first part of this section, the flight stages are elaborated upon. Afterwards, an intermediate summary is given with reference speeds as calculated in the first subsections.

5.1.1. The design space: W/S and W/P diagrams

In order to obtain initial values for major design parameters such as wing area, aspect ratio, and power, the W/S and W/P diagram is constructed, as shown in figure 5.1. W/S is the wing loading in N/m^2 and W/P is the power loading in N/W , where the W is the MTOW of the aircraft. When plotting the W/S and W/P diagrams, the wing loading was mainly limited by the landing condition, this produced a desired landing stall speed, from which the wing area can be sized with $C_{L_{max}}$. The value of $C_{L_{max}}=4$ was assumed to be an attainable value, since $C_{L_{max}}$ values of 5 were expected from Distributed Electric Propulsion (DEP). (Stoll et al., 2014) This leads to a wing area of just $8.42 m^2$, which reduces the zero-lift drag during cruise. The lift induced drag is still just a quarter of the total drag because of the high aspect ratio. The high aspect ratio is also needed to accommodate the propellers. The only uncertainty is the Takeoff lines, since different books use different definitions and units of Take Off Performance (TOP), which are complex to convert. Due to the hybrid battery boost, and possibility to drive the wheels, it is foreseen that takeoff is not the driving requirement.

5.1.2. Wing Layout

There are 18 engines in total, of which 12 are DEP engines. The DEP engines are located along the section of the span where the flaps are present, which is 3 m long. The flap was selected to have a span of 3 m at 16.7 to 66.7 % of the semi span, leaving 1m of space for the fuselage and 1.98m the ailerons. For redundancy, the number of cruise propellers is set to 6. They are sized to have similar power loading as a Cirrus SR22 (50 to 60 kW/m^2), so they are not undersized. The number of DEP propellers are varied, but the number of 12 propellers was chosen as a trade-off between DEP effectiveness (which favours more propellers) and complexity (which favours less). Their size is comparable to the propellers in Stoll et al. (2014). The design of the propellers is shown in section 5.1.15.

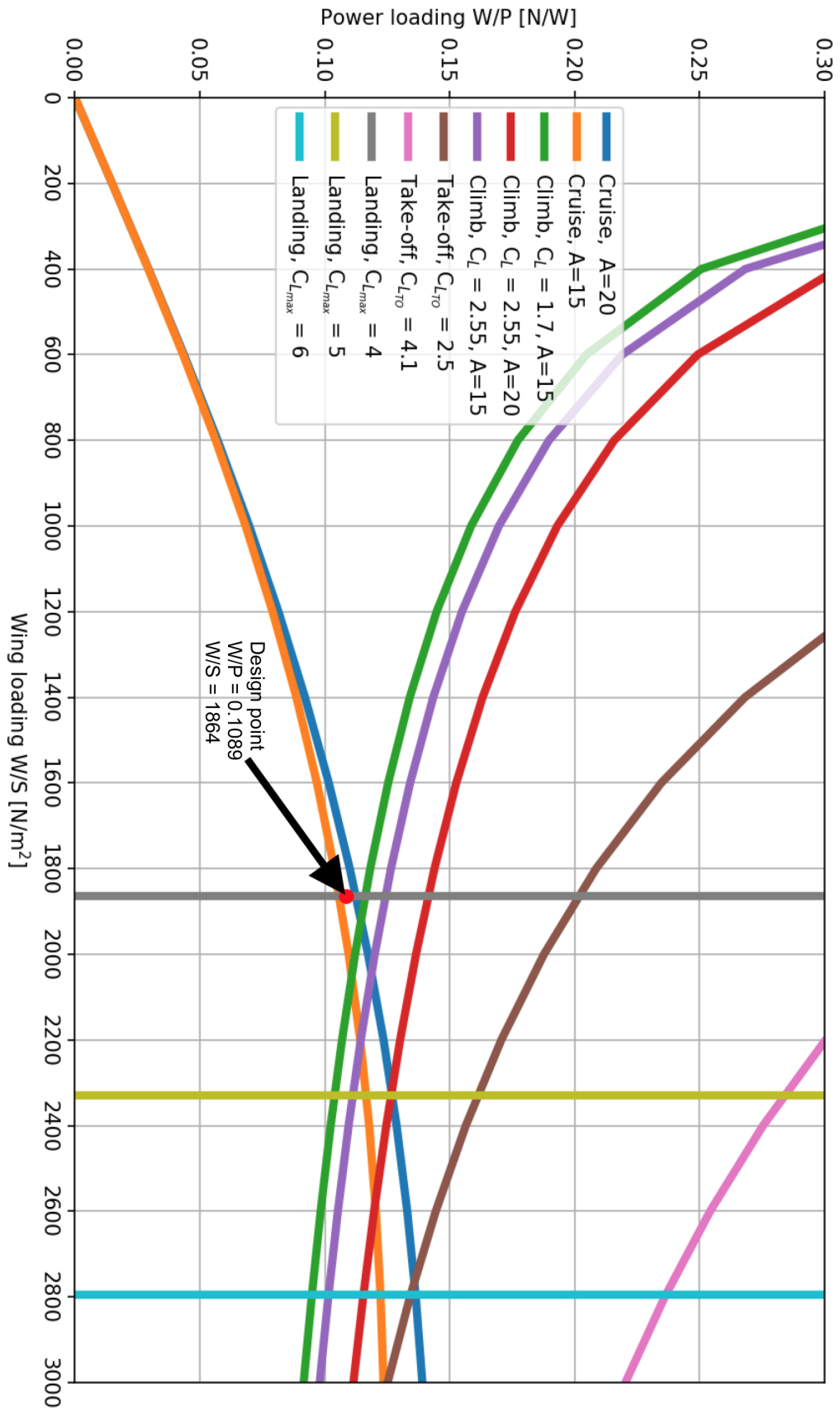


Figure 5.1: The $W/S, W/P$ diagram, otherwise known as "design space"

5.1.3. Take off

During take off, the flaps are set to 10 degrees, this is a standard flap setting for takeoff on many aircraft, producing extra lift with a small drag penalty.

To improve efficiency, the car tires are used. The car tires transform all their shaft power into useful work, whilst the efficiency and thus the thrust of the propellers suffer at these low speeds. For both takeoff and landing, formulas from Voskuil (2016) are used.

During the ground run, the maximum power of 203 kW is set, as determined for under the approach condition with speed brakes deployed.

The propellers have 144 kW of power, as determined for the climb phase. The remaining power goes to the DEP propellers, at 8 kW each, and the outboard propellers run at 1/3rd power which is 8 kW. The wheels are supplied with 59 kW of electric power. At lower speeds, the "thrust" is limited by torque of the engine.

At V_{ave} , as evaluated in the next paragraph, the "thrust" provided by the wheels is 2266 N and that of the propellers is 3630 N, the wheels provide 38% of the total thrust. The risk of tipping over about the rear wheels has been evaluated in section 5.3. The result was that the maximum torque of the car produced a thrust at standstill of 4700 N, which would make the car tip over. For safety the power on the wheels is limited to produce a force of no more than 3000 N at low speeds, to ensure the front wheels do not lift off. After 19 m/s (37 kts), the thrust is limited by the car's power, and power is applied up unto rotation. Rotation and liftoff are assumed to occur at the same moment in time, the tires provide grip for the entire ground run and have enough grip to provide 3624 N up to the moment of rotation, where just 35% of the aircraft weight is pressing down on the wheels.

The thrust and drag on the ground run are evaluated at V_{ave} , which is $V_{lof}/\sqrt{2}$, equal to 52 kts. The rotation speed, and thus V_{lof} , at 73 kts, have been determined at an angle of attack of 6 degrees for the aircraft. The only limit is that V_{lof} has to be at least $1.05 \cdot V_{mc}$, where V_{mc} is the minimum speed for maintaining "adequate aeroplane control for take-off" (Ruijgrok, 2009), in the case of an engine failure. V_{mc} lies at 69 kts, which is the highest possible with the current V_{lof} , it lies 4 kts above the stall speed V_{ms} . The tail will be sized for the event of an engine failure at this speed, as explained in section 5.3. At the moment of rotation, the car propulsion is switched off. The resulting ground run is 228 m.

The airborne phase of the manoeuvre the aircraft has to clear a fence of 50 ft (15.2 m), whilst flying at a minimum speed of $1.2 \cdot V_{ms}$, in case of engine failure. Unlike CS25, CS23 has no different value for the case of 4 engines or more. Taking a higher speed would result in degraded climb angle, and thus a longer airborne phase, therefore $V_{scr}=1.2 \cdot V_{ms}=78$ kts is chosen. The outboard engines ramp up from 8 to 16.5 kW of power at the moment of rotation, which is 99 kW combined, this was the required cruise power in an earlier calculation. At the fence, a steady climb gradient of 12.7% is achieved. The DEP propellers still run at full power, providing 96 kW combined, leading to a total of 195 kW of power. After reaching a safe altitude the aircraft will accelerate further and raise the flaps. The resulting airborne phase is just 130m.

The combined takeoff distance, at maximum takeoff weight, at sea level altitude, is just 367m.

5.1.4. Climb and Acceleration

Climb was modelled in clean condition from an altitude of 0 up to 8000 feet. The brake power available is 144 kW, of which 24 kW is supplied by the battery. Rather than optimising for rate of climb, a climb profile with higher speed, and lower battery use is chosen. At a C_L value of 1, an indicated airspeed of 107.3 kts is maintained, resulting in an unsteady rate of climb of 728 fpm, which is 2% below the steady speed of climb, since the speed is increased slowly to account for the lowering density. It takes 11 minutes to reach cruise altitude, during this manoeuvre, the horizontal distance covered is 39 km. During the climbing manoeuvre, 4.7 kWh of the battery is consumed. After climbing, the aircraft has to be accelerated to from 107.3 to 160 kts, this takes just approximately 75 seconds, and 5.5 km in distance, consuming another 0.5 kWh from the battery. For E10 gasoline, this resulted in a fuel consumption 40% lower than the class I estimate. The exact consumption during takeoff and early climb-out has not been computed, but at 80 kW, it may take 3.6 minutes to consume the 4.8 kWh budget left for takeoff.

5.1.5. Cruise

The cruise phase was calculated using the Breguet range equations (Vos et al., 2017), and the L/D determined at the average cruise weight of 1540 kg. The range used as input was 555.6 km (300 NM), plus half an hour reserve at

cruise speed, minus 39 km from the climb phase. The resulting cruise range is 665 km. During cruise, the fuel use for Ethanol E85 is 101 kg and for Gasoline E10 it is 76 kg. The fuel properties are further elaborated upon in the system sustainability, section 9.2 and section 5.1.8. This 39 km is not removed from the required range for the normal operations, which means that the fuel consumption in section 5.1.8, may become slightly lower. Cruise is performed at 8,000ft, and 160 kts TAS. At 10,000 ft, the cruise speed would be 137 kts EAS, which is still well above the clean stall speed of 110 kts EAS. The case of cruising at low altitude (1500ft) due to VFR restrictions is also considered: When cruising at 160 kts TAS, the increased density at lower altitude leads to an increase in parasitic drag, and a decrease in induced drag, because of the higher dynamic pressures. The power requirement is therefore increased from 122 kW shaft power to 137 kW. Therefore, the aircraft will need to keep flying at 137 kts EAS at these altitude to limit the power needed.

5.1.6. Descent

Descent was calculated for the case of charging the 10 kWh battery, to ensure a safe landing and possibility of a go-around. The thrust and distance during descent have not been evaluated. If the drag of the free-milling outboard engines is ignored, a glide ratio of 17 can be achieved.

5.1.7. Landing

For landing, the standard fraction was used for gasoline, resulting in around the same consumption as the climb phase. When the spoilers are extended too early, a lot of power is needed to remain airborne: 203 kW. A large share of power will come from the battery approach: around 80 kW. This will be further elaborated upon in section 5.1.14.

The approach speed is $1.3V_{stall}$, this has to be maintained up until the fence. At approach speed, with an angle of 3 degrees (no flare), the vertical speed is 2.0 m/s. Since DEP produces thrust, the flare manoeuvre will significantly increase. The thrust of DEP increases from 60% on approach to 70% on touchdown, which occurs at $1.15V_{stall}$. To counteract this thrust, speed brakes are extended. Since "A constant configuration must be maintained throughout the manoeuvre" (EASA, 2010), they are deployed during the approach. However, their size is limited due to the fact that the aircraft has to remain airborne, and not descend below its steady approach angle of 3 degrees. The speed brakes are sized for the "excess" thrust of the outboard propellers, which is 2.3 kN. This leads to the high power demand of 203 kW during final approach. During the manoeuvre, the cruise propellers are switched off, whilst DEP increases. At touchdown, with flaps, DEP producing thrust and speed brakes producing drag, the L/D ratio is still fairly high at 7.8. Ground effect is taken into account, which decreases the lift induced drag by 50%, at touchdown.¹ Any increase in lift is neglected. The resulting airborne phase of the manoeuvre is 338 m.

During the ground run, the automotive tires and brakes help take the aircraft to a quick stop. It is assumed 95% braking capacity is reached through modern ABS, with a friction coefficient of 0.7, and at an estimated average 25% L/W value. This results in a ground run of 123 m. The total landing distance is 462 m. The required field length is actually 10/6 times the shortest demonstrated distance; this would be 770 m if the tests were conducted as simulated, with no wind, at MTOW. Touching down sooner, at a higher speed, will reduce the airborne phase, but braking at high speed is limited, especially without the use of spoilers. This is certainly material for further research.

5.1.8. Summary of Fuel Consumption

Table 5.1: Fuel use at maximum range, and MTOW

Flight Stage	E85	E10	100LL
1.start	8.1	6.4	6.4
2. taxi	4.8	3.2	3.2
3.TO	3.2	3.2	3.2
4. climb	9.7	7.8	7.8
5. cruise	101	84	82
6. descent	3.7	3.0	3.0
7. land	10.3	7.5	7.5
total [kg]	141	115	113
volume [L]	181	157	157

¹<https://www.skybrary.aero/index.php/File:Induced-drag.jpg>, (Retrieved on 21 January 2018)

As can be seen from Table 5.1, Ethanol E85 has less energy content, however, this will remain the fuel of choice because of sustainability reasons (see Section 9.2 also). Avgas 100LL has a slightly higher energy content than gasoline but is also slightly less dense.

According to CADDET Centre for Renewable Energy (1997), the increase in fuel consumption when flying on ethanol is around 15%. Another source states 15% to 27% worse economy.² 15% increase in fuel consumption is used for further calculations, since this value was based on an aero-engine that previously ran on Avgas.

5.1.9. Payload Range Diagram

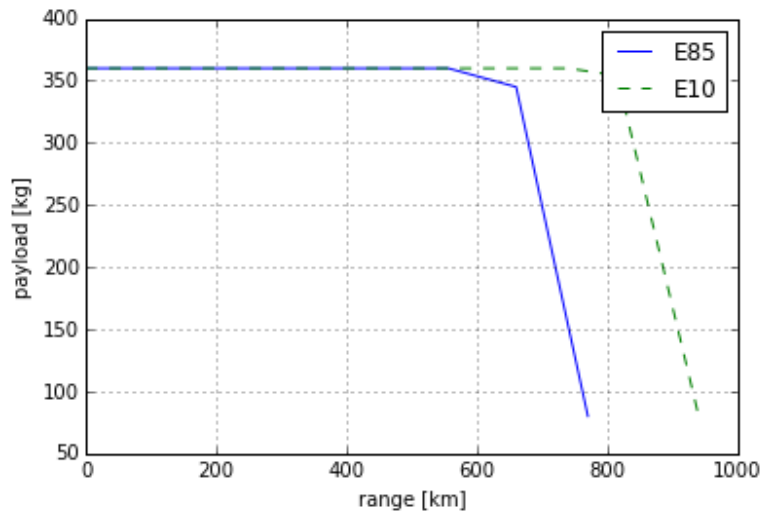


Figure 5.2: Payload range diagram for 2 types of fuel

The 1600 kg MTOW allows for 360 kg payload and 141 kg of fuel (before starting). The fuel tanks have a combined capacity of 200 L. This may contain 156 kg of E85 Ethanol or 147 kg of E10 gasoline. It can be seen that a full tank of E10 gasoline will provide 20% more range than E85 ethanol. The minimum payload is 80 kg, since a pilot has to be included. Avgas has not been included, but lies very close to E10, because they are 90% identical.

5.1.10. Summary of Flight Configurations

An overview of the aircraft configuration during various flight stages is provided in Table 5.2. The drive train is a series hybrid system, as mentioned in Section 4.3.1, and detailed in Section 5.1.14.

Table 5.2: Summary of typical flight stages

Stage	Speed [kts]	Power set (DEP)*	α (Wing)	α (Aircraft)	P_{brake} (kW)
Liftoff	73	96	8	6	195
Climb	107	0	7	5	160
Cruise	160**	0	2	0	130
Approach	73	60	7	5	70
Touchdown	64	70	10	8	70

*out of 99 kW

**TAS, other speeds are in EAS since they are evaluated at ground level or throughout a climb manoeuvre.

The efficiency of the electric motors is 96%, the efficiency of the controllers is 98%.

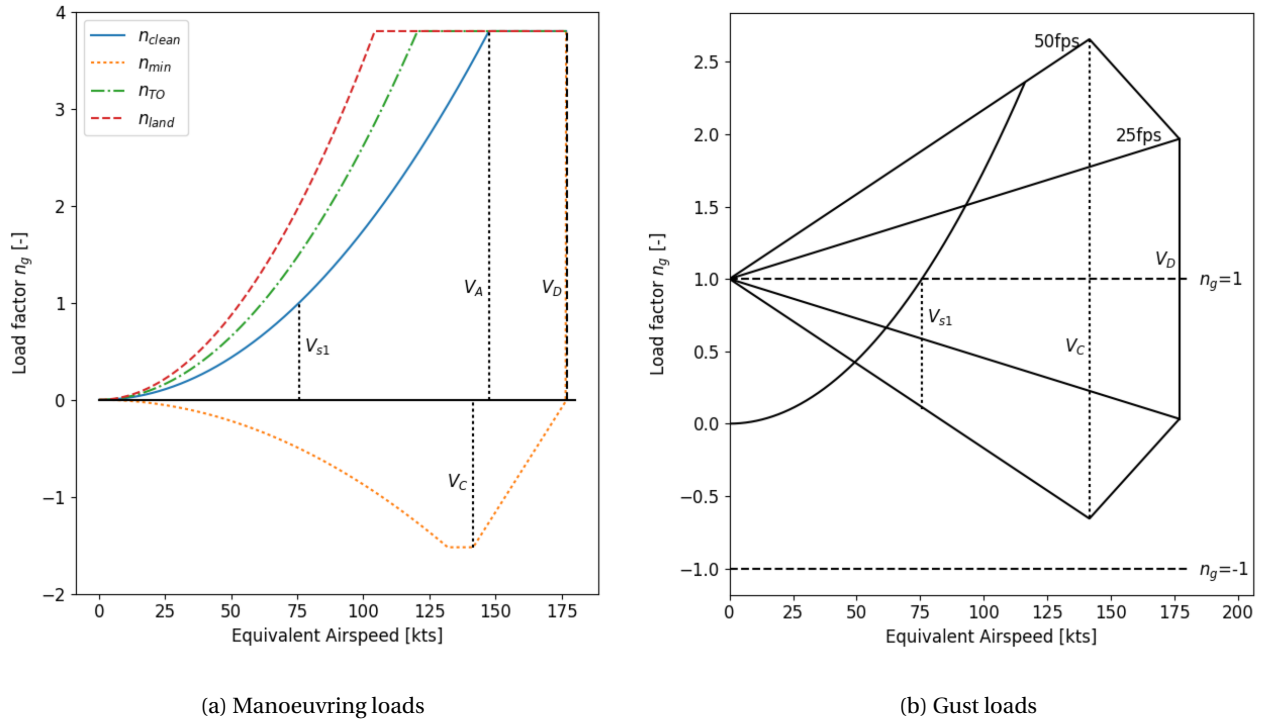
The stall speeds are given for common configurations in tabletable 5.3.

²<https://www.fueleconomy.gov/feg/ethanol.shtml>, (Retrieved on 21 January 2018)

Table 5.3: Stall speeds

	speed [kts]	power set (DEP)*	α (Wing)	α (Aircraft)	P_{brake} (kW)
V_s T/O	65	96	12.6	10.6	194
V_s land	56	96	12.6	10.6	96
V_s clean	110	0	12.6	10.6	130

5.1.1.1. Flight Envelope (Manoeuvring and Gust Loading Diagram)

Figure 5.3: (V_{EAS},n) diagrams

The (V_{EAS},n) diagrams shown in Figure 5.3 were set up in accordance with CS23.335-341³, with the vehicle classified as a normal category airplane.

The parameters on both diagrams are as follows:

- V_{s1}
Stall speed of the clean aircraft configuration at a load factor of $n = 1$. $V_{s1} = 75.7$ KEAS
- V_C
Cruise speed of the aircraft. The requirement specified this as 160kts TAS, which means $V_C = 141.6$ KEAS.
- V_A
Design manoeuvring speed of the aircraft, defined in CS-23 as being $V_A = V_s \sqrt{n_{max}}$ with n_{max} being the limit manoeuvring load factor.
- n_{max}
Positive limit manoeuvring load factor used in design, defined as $2.1 + \frac{24000}{W+10000}$ where W is in lbs. For this vehicle, $n_{max} = 3.8$
- n_{min}
Negative limit manoeuvring load factor, defined as $n_{min} = -0.4 \cdot n_{max}$.
- V_D
Design dive speed, defined as $V_D = 1.4 \cdot V_C = 177$ KEAS
- 25 fps and 50 fps gust lines
The diagram includes both positive and negative 25 feet/second and 50 feet/second gusts; their respective load

³<https://www.easa.europa.eu/certification-specifications/cs-23-normal-utility-aerobatic-and-commuter-aeroplanes>, (Retrieved on January 10 2018)

factors can be found at V_C and V_D . The procedure that was used to compute the associated load factors were computed can be found in CS23.441.

Table 5.4 presents the load factors that can be seen in both diagrams.

Table 5.4: Manoeuvring and gust load factors

Manoeuvring		Gusts			
n_{max}	n_{min}	$n_{max,50fps}$	$n_{max,25fps}$	$n_{min,50fps}$	$n_{min,25fps}$
3.82	1.52	2.66	1.97	-0.66	0.03

5.1.12. Non-standard Operations/Emergencies

There are several concerns regarding the safe operation of the aircraft, especially with regards to the failure of multiple engines.

Concerns were raised about a total failure of DEP, which could have several causes, such as fuel starvation. With the relatively small wing area, this would increase the landing speed. This would increase the stall speed in landing configuration from 56 kts to approximately 80 kts. Using the statistical formula $S_L = 0.56 * V_{stall}^2$, the landing distance is estimated to be 949 m. This means that, in the case of an emergency, the aircraft will be restricted to business and regional airports or larger. The first order estimate for the standard configuration is 465 m.

Since the failure of a single cruise engine in flight will result in large control forces in flight, the possibility of shutting down the opposing engine is considered. This reduces the available shaft power to 96 kW. This reduces to the cruise speed to approximately 140 kts TAS, or 124 kts IAS, which is still above the stall speed of 110 kts IAS. In case of another failure, the aircraft will have to descend, and use the DEP engines.

5.1.13. Car Propulsion

The automotive electric motor has approximately 60 kW of continuous power. This should be more than sufficient to reach a top speed of 130 km/h, the exact top speed depends on aerodynamic design and rolling drag. For reference, a Suzuki swift with 69 kW reaches a top speed of 165 km/h.

5.1.14. Propulsion Components

In this chapter, the selection and function of the main propulsive components are elaborated upon. Propellers are addressed in the Section 5.1.15, and the mass of remaining components, such as cables and controllers, are mentioned in Table 4.5.

The hybrid system was chosen for increased efficiency; it can supplement the internal combustion engine (ICE) when needed, leading to a lighter ICE. It also allows for the use of regeneration when driving on the road. The selected type of hybrid electric system is called a series hybrid. This means that there is no direct link between the engine and the driven wheels and propellers, but that the wheels and propellers are driven only by electric motors. This limits the amount of moving parts, and enables the use of DEP, whilst allowing for the use of an electric linkage with no mechanical clutches or fuel lines. Ground tests on a series hybrid system of the same output (200kW) have been conducted by Pipistrel and Siemens for the Hypstair project.⁴

Disadvantages of the the hybrid system are energy losses in electric components, and their mass. Fitting all electronics is a challenge, room has been reserved in the wing box to accommodate cables and engine controllers. The major components are listed in Table 5.5.

⁴<http://www.hypstair.eu/>, (Retrieved on 30 January 2018)

Table 5.5: Propulsion subsystem components

Component	Specification	#
Turbocharged piston engine	130 kW continuous; 6% boost	1
Generator	130 kW continuous	1
Battery	10 kWh	1
DEP engine	8 kW continuous	12
Cruise engine	24 kW continuous	6
Car electric motor	30 kW continuous; 15 kW boost possible	2

The engine initially selected was the Rotax 915 series, which was certified last year. The required power rose throughout the design process, therefore the design was extrapolated 30% in terms of mass and power, see Section 4.2. It is expected that Rotax will release larger engines in the future, or that automotive engines, which have similar specific power, (around 100hp/L,) can be modified. An alternative would be the Lycoming IO-360, or the Continental IO-360, preferably turbocharged to perform at altitude, but it is feared that these blocks are not fuel efficient enough due to their age, the earliest variants were certified in the 50's and 60's.

The Rotax 915 engine has several advantages:⁵

- No loss of power with altitude; take-off power (105 kW) available up to 15,000 ft
- Continuous power close to takeoff power (99 kW). Advantageous for the hybrid system
- Compatible with regular gasoline (95 RON)
- High RPM compatible with selected generator (5500 RPM continuous)
- Turbocharged engines tend to be quieter since the turbine muffles part of the engine sound

Another source reveals additional information:⁶ The fuel consumption is around 280-310 g/kWh BSFC (Brake Specific Fuel Consumption) at 5500 RPM. E10 gasoline is also mentioned.

The required generator is scaled from a design from Siemens(Petermaier, 2015), which is rated at 170 kW. A 135 kW meant for a diesel engine (AE300) is currently under development, with a capacity of 7 kW/kg. When scaling down, identical ratios between maximum torque, power and RPM are assumed.

The battery is scaled using an initial estimate of 40 kW boost, for a maximum of 15 minutes time. This turned out to be sufficient for flight, if charged during a descent. For automotive use, the battery will last for approximately 100 km of driving (see section 9.2, before the generator needs to kick in. There is 10 kWh worth of cells. The bare cells are estimated to be rated at 333 wh/kg, therefore 30 kg will be needed. The enclosure is estimated to be 20 kg. The combined density is then 200 wh/kg. For reference, the Pipistrel Alpha Electro currently has 135 Wh/kg⁷.

One challenge is the energy density of the batteries, with current technology the battery package is only able to provide about half of the power needed. The Pipistrel Alpha Electro has an 85kW motor, meaning the battery will probably be able to provide 0.67 kW/kg. With the 50 kg battery system, this gravimetric energy density is insufficient for take-off and landing conditions. This will need to be addressed by using different electronics and improvements in battery technology that are being awaited.

The electric engines are scalable, at 5 kW/kg, two of such engines have been developed at 65 kW and 1/4 MW. (Petermaier, 2015) A cooling solution is needed, either liquid or direct, fortunately the heat produced by an electric motor is much smaller than the heat produced by an ICE because of its high efficiency.

5.1.15. Propeller Design

Choosing a highly unconventional propulsion system brings with it several advantages and disadvantages. One advantage is that the use of 18 different propellers allows for optimisation for cruise and take-off configurations. Propellers that are highly efficient and provide a lot of thrust at take-off will not necessarily perform the same at cruising altitude, even if that cruising altitude is only 8000 feet. A disadvantage of using so many propellers is that their respective diameters have to be much smaller to be able to place them along the leading edge of the wing within the maximum wingspan. This means no standard single-engine aircraft propellers can be chosen, since those are usually of much larger diameter. Additionally, due to the unconventionally small size of the propellers, questions were raised about the noise created by propeller blades with greater tip speeds due to the smaller tip radius. From prior research, it was established that blade geometry and the number of blades used can greatly affect the noise produced by the

⁵<https://www.flyrotax.com/produkte/detail/rotax-915-is-isc.html>, (Retrieved on 21 January 2018)

⁶<https://www.rotax-owner.com/en/rotax-blog/item/43-915is>, (Retrieved on 21 January 2018)

⁷<https://www.pipistrel.ad/training/alpha-electro>, (Retrieved on 21 January 2018)

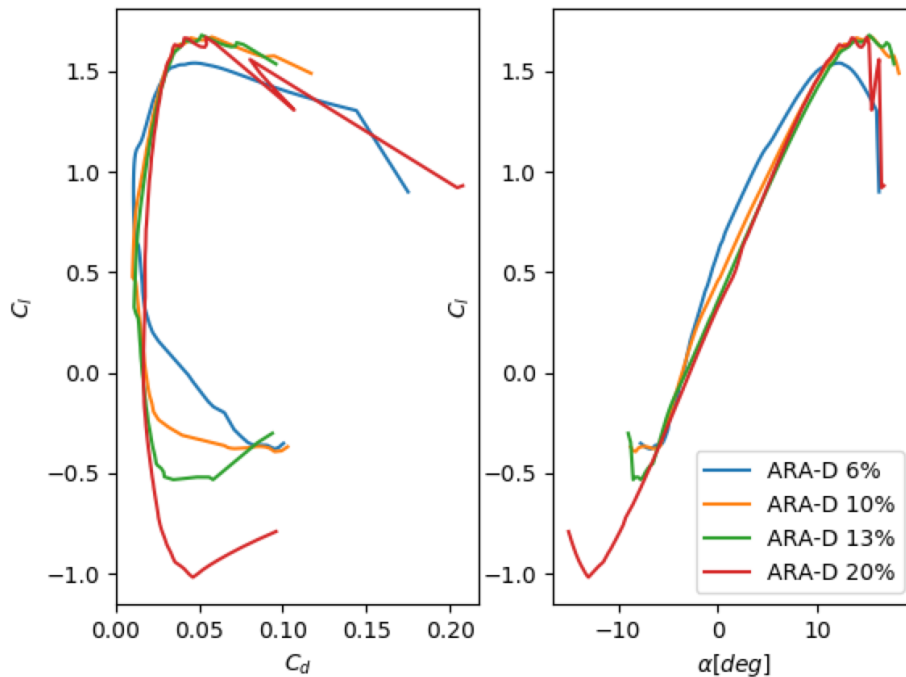


Figure 5.4: C_l - C_d and C_l - α for ARA-D family

propeller and therefore will have to be analysed. For these reasons, a decision was made to design custom propeller blades, optimise them for take-off and cruise configurations, and analyse how many blades each propeller will have.

The propeller blades were designed and analysed using XROTOR⁸; an open-source computational fluid dynamics suite tailored to propeller design for aircraft propellers and windmills. Propeller blade lofting and airfoil modelling were done using CROTOR, an open-source extension to XROTOR.

First, the ARA-D family of airfoils was selected for use in both propeller blades in order to simplify analysis and comparison for both. They are also known to have excellent performance at higher tip Mach numbers, which is to be expected with the smaller propellers in the DEP system. Developed in the 70s by the British Aeronautical Research Association specifically for use in propellers, airfoils in the ARA-D family vary only by a single parameter, the thickness over chord ratio t/c . Figure 5.4 presents the airfoil characteristics, obtained using XFOIL at $Re = 200,000$.

The propeller blades were then designed according to their specific operating conditions as follows:

DEP Propellers

The propellers that will provide extra lift on take-off, henceforth referred to as DEP propellers, were required to perform optimally at landing conditions: an altitude of 0 feet AGL and a speed of 40.8m/s. The radius of the DEP propellers was determined by finding the lowest amount of propellers that could be used in order to still achieve a significantly increased lift coefficient on take-off. The propulsion system configuration was inspired by the NASA LEAPTech project (Stoll et al., 2014) by setting those results as a performance goal for the design of this vehicle, then modifying the number of engines/propellers and distance between them until these results could theoretically be replicated. In the end, it was decided to use six DEP propellers (12 total) with a radius of 0.241m. These six propellers are intended to cover the flapped area of the wing which is exactly 3m long, leaving a couple of centimetres of tolerance between the props for safety reasons.

⁸<http://web.mit.edu/drela/Public/web/xrotor/>, (Retrieved on January 9 2018)

Cruise Propellers

The cruise propellers were required to perform optimally at the cruise altitude of 8000 ft AGL (2.44km) and cruise speed of 160 kts TAS (82.31 m/s). The radius of the cruise propellers was primarily dictated by the spanwise positioning of the flaps and the need for three cruise propellers on each side for redundancy and fulfilling the PPL requirement. The resulting propeller radius is presented in Table 5.6.

The propeller blades themselves were optimised using XROTOR with the following two main considerations in mind:

- Highest achievable propeller efficiency at the specified speed and altitude (mainly optimized by varying tip twist angle of the blade)
- Lowest overall propeller noise level (mainly driven by the number of blades on the propeller)

The design parameters and results from the propeller optimisation process are presented in table 5.6.

Table 5.6: Design parameters and results for cruise and DEP propellers/blades

Propeller	r_t [m]	r_{hub}	β_{tip} [deg]	V [m/s]	h [km]	η_{prop}	N_{blades}	$L_{A_{max}}$ [dB(A)]
DEP	0.241	0.05	25.226	40.8	0	0.7211	5	49
Cruise	0.376	0.07	43.2	82.31	2.44	0.8232	4	51

In which:

- r_t is the tip radius in meters, from the propeller centre line to the tip of the blade
- r_{hub} is the radius of the propeller hub, primarily driven by the radius of the electric motor powering the propeller
- β_{tip} is the angle of twist of the airfoil profile at the tip of the blade, with respect to the airfoil profile at the root of the blade where it is attached to the propeller hub
- V and h are the parameters of the design points the propellers are optimised for
- η_{prop} is the resulting propeller efficiency
- N_{blades} is the number of blades on the propeller
- $L_{A_{max}}$ is the maximum A-weighted noise level produced by 1 propeller at 1000 ft. AGL when running at full power, optimised using the number of blades on the propeller

The resulting blade geometry can be seen in Figure 5.5.

Figure 5.5 also shows where the 4 ARA-D airfoils are located along the propeller, at locations that experience the local helical tip Mach number for which the particular airfoil is designed.

Figure 5.6 shows the aforementioned propeller parameters, as well as additional parameters such as the thrust delivered by the propellers at the design point. The graphs show the radial distributions of efficiency (η_{local}), local Mach number (dotted line) and circulation Γ expressed in the Betz-Prandtl canonical form. The latter is not especially relevant to the optimisation performed here and is more concerned with wake effects, which will not be analysed at this stage.

5.1.16. Noise Performance: Aircraft

Since the noise performance of the vehicle is determined by a large number of parameters, priority had to be given to the most influential of these parameters in order to optimise the design. Since the ICE that is used is mostly internal to the vehicle and will therefore be shielded sufficiently, the propeller noise was determined to be the most crucial aspect of the vehicle's noise performance. This is especially true considering the large amount of propellers (18 in total) and the fact that two different types of propellers are used. Table 5.6 in Section 5.1.15 shows the noise performance of just one propeller for each type at the design point. In order to compute the total propeller noise however, these measurements have to be fine-tuned and calculated for the total array of 12 DEP propellers and 6 cruise propellers.

First, the measurement conditions were set in accordance with 14 CFR Appendix G to Part 36⁹ and the after-take-off/climb design point:

- Power setting of 100%
- Velocity of 40.8 m/s
- Aircraft altitude of 1000 ft AGL (resulting in the corresponding atmospheric conditions)
- Microphone height of 1.2 m (4 ft) above the runway

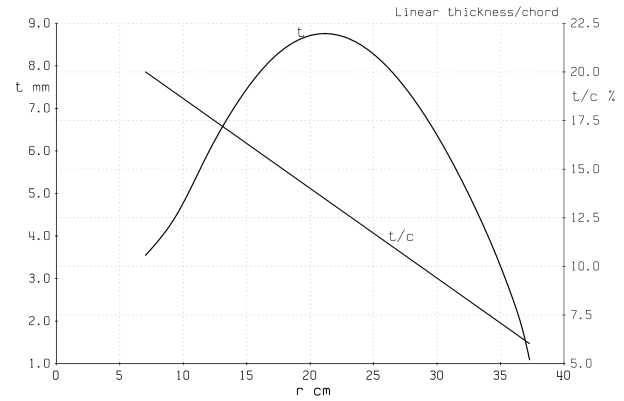
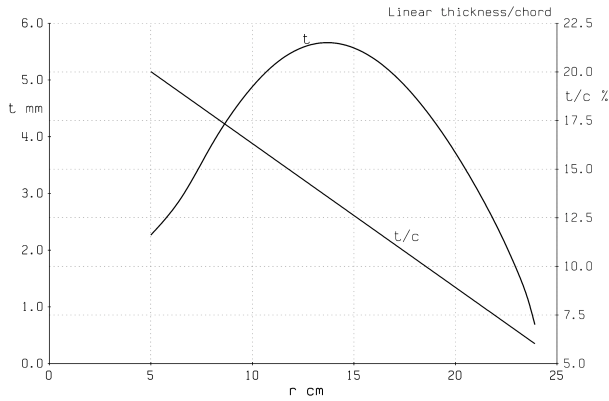
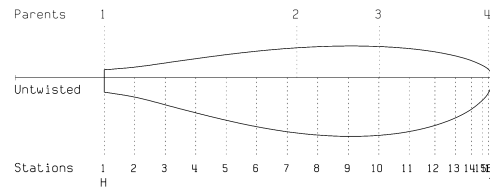
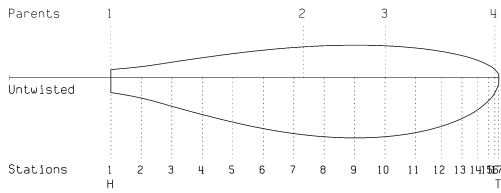
This resulted in an accurate noise estimation at these conditions per type of propeller. The total propeller noise was then calculated using eq. (5.1)

⁹https://www.law.cornell.edu/cfr/text/14/appendix-G_to_part_36, (Retrieved on 12 January 2018)

Lofted Blade: smallprop

Lofted Blade: largeprop

CROTOR v755-ES1.3



(a) DEP propeller, 5 bladed

(b) Cruise propeller, 4 bladed

Figure 5.5: Geometry and airfoil station locations of the two propellers

$$\text{total } L_{A_{max}} = 10 \cdot \log_{10} \left(N_{DEP} \cdot 10^{\frac{L_{ADEP}}{10}} + N_{Cruise} \cdot 10^{\frac{L_{ACruise}}{10}} \right) \quad (5.1)$$

in which:

- N_{DEP} is the number of DEP propellers
- N_{Cruise} is the number of cruise propellers
- L_{ADEP} is the maximum A-weighted noise level at the aforementioned conditions for one DEP propeller.
- $L_{ACruise}$ is the maximum A-weighted noise level at the aforementioned conditions for one cruise propeller.

The results from the propeller noise calculations are presented in table 5.7.

L_{ADEP}	$L_{ACruise}$	total $L_{A_{max}}$
39.5 dB(A)	47 dB(A)	52.3 dB(A)

Table 5.7: Propeller noise level results (V=40.8 m/s, 100% power, h = 1000 ft AGL)

The difference between the noise levels generated by the DEP propeller versus the cruise propellers is caused by three parameters, as presented in Table 5.8

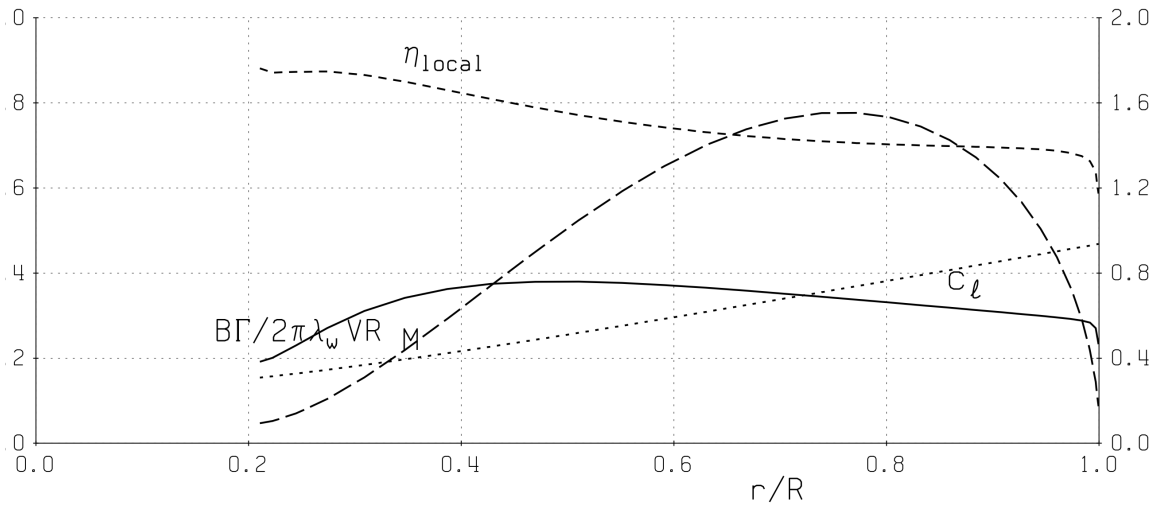
Table 5.8: Propeller data at noise measurement design point (V=40.8 m/s, 100% power, h = 1000 ft AGL)

Propeller	RPM	M_{tip}	N_{blades}
DEP	6165	0.475	5
Cruise	3418.6	0.415	4

Comparing the two propellers, the DEP propellers are running at almost twice the RPM of the cruise propellers. The increase in noise caused by this high RPM and resulting higher tip Mach number is mitigated by the increased blade count and lower radius, resulting in a significantly lower L_{ADEP} as opposed to $L_{ACruise}$.

smallprop

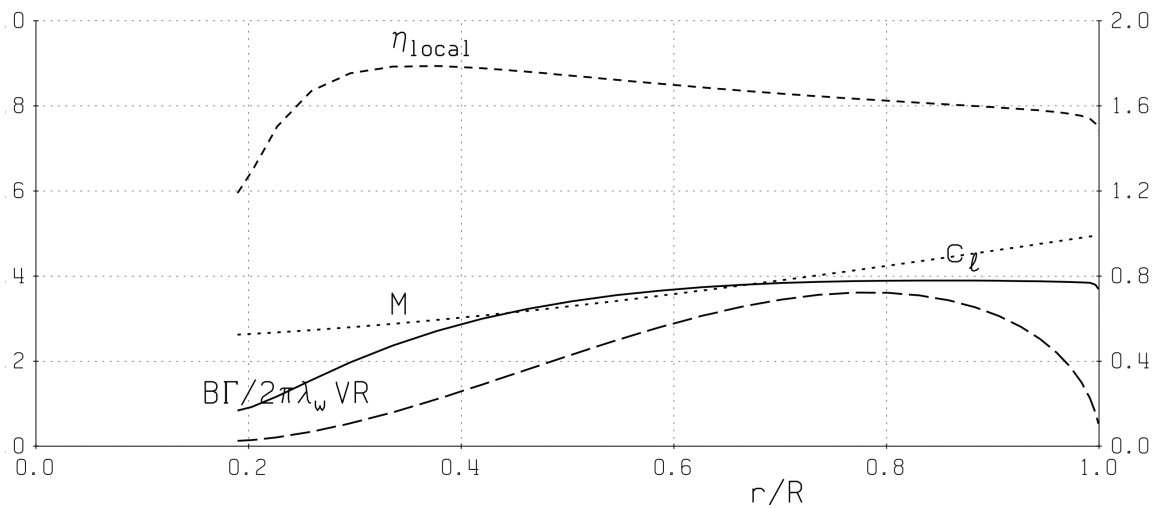
#bld= 5	R m = 0.241	$\sigma_{3/4}$ = 0.2984	β_{twist} = 28.651	
Vm/s= 40.800	V/QR= 0.2642	P_C = 1.053	C_P = 0.2365	η_{ideal} = 0.8597
h km= 0.000	J = 0.8300	T_C = 0.759	C_T = 0.2054	η = 0.7211
T kN= 0.1414	P kW= 8.0000	RPM = 6119.0	β_{tip} = 25.226	



(a) DEP propeller

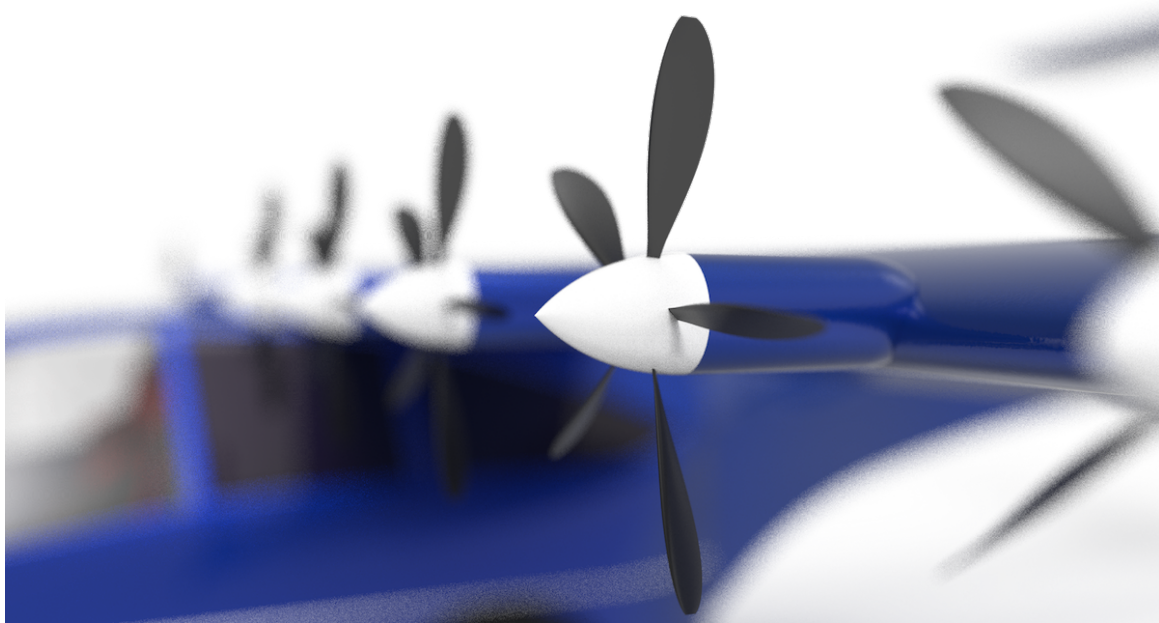
largeprop

#bld= 4	R m = 0.376	$\sigma_{3/4}$ = 0.2384	β_{twist} = 28.651	
Vm/s= 82.311	V/QR= 0.5782	P_C = 0.201	C_P = 0.4731	η_{ideal} = 0.9617
h km= 2.440	J = 1.8163	T_C = 0.166	C_T = 0.2144	η = 0.8232
T kN= 0.2400	P kW= 24.0000	RPM = 3615.7	β_{tip} = 43.226	

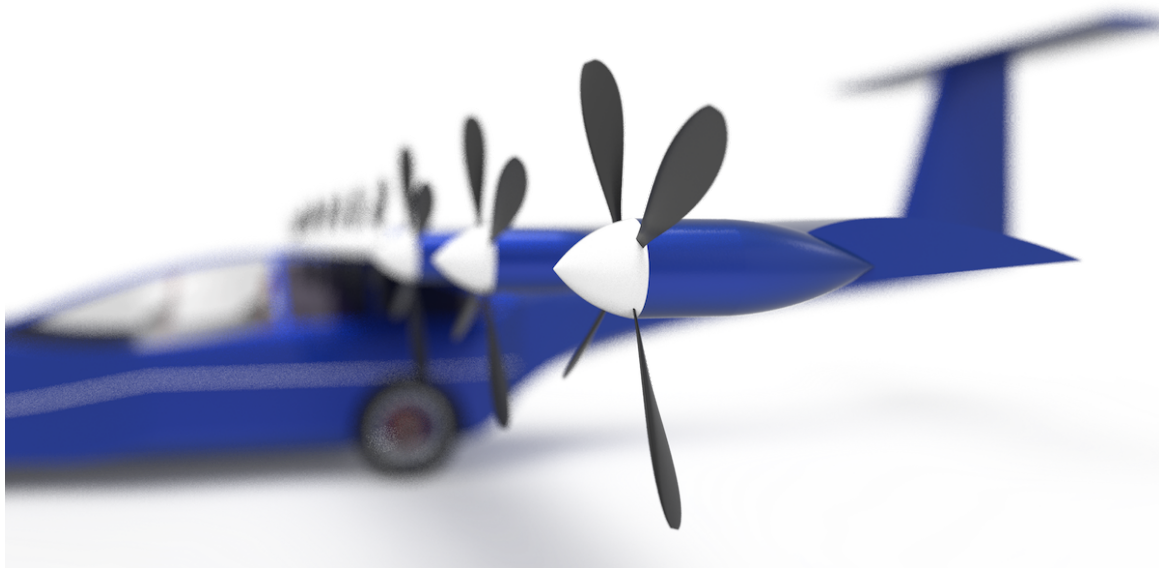


(b) Cruise propeller

Figure 5.6: Radial distributions of propeller characteristics: efficiency and Mach number



(a) DEP propeller



(b) Cruise propeller

Figure 5.7: Rendering of two propellers on the wing

Other noise sources

Even though the noise from the vehicle's 18 propellers was analysed extensively because it is the biggest contributor to overall noise levels, there are several other factors that cause abnormal noise behaviour relative to conventional general aviation aircraft.

- **Cabin noise**

While noise levels on the ground caused by the vehicle are decreased drastically due to the use of electric propulsion and propellers with a low tip Mach number, the fact that the vehicle uses 18 different propellers will have severe effects on cabin noise. The pilot and passengers are sitting in between the two 9-propeller arrays, with two types of propellers that are not only always spinning at different speeds but whose rotational speed is also

varied depending on power setting (since the propellers are constant-pitch). Significant increases in noise levels due to flow impingement effects of the propellers on the wing and on each other are to be expected, most of which is concentrated around the cabin. (Block and Gentry Jr., 1986)

- **Airframe noise**

With the advent of electric propulsion comes a change in how aircraft noise is analysed. Engine and propeller noise are no longer the only significant contributors to vehicle noise; the noise generated by the airframe itself has also become a factor. Airframe noise is notoriously difficult to analyse since it is often caused by a large variety of different noise sources interacting with each other. Noise generated by landing gear is a good example of airframe noise, since for large aircraft landing gear noise is often one of the most significant noise sources while landing, with the engines throttled back. While the vehicle under consideration is by no means a large aircraft, it does have clunky, non-retractable road-optimised landing gear which will surely generate a lot of noise in any flight phase. (Yong et al., 2013)

- **Trailing edge noise.**

Technically a part of airframe noise, trailing edge noise is generated when turbulent flow across an airfoil section reaches a sharp trailing edge and experiences a sudden pressure jump. It is especially relevant for this vehicle since the wingspan is very high and there are small airframe 'gaps' where the flight hardware meets the road hardware. (Howe, 1978)

All the noise sources mentioned above were not analysed quantitatively, since this is not feasible at this stage of the design process and requires very advanced flow modelling techniques.

5.1.17. Noise Performance: Car

While propeller noise and other noise sources associated with the flight hardware will be the driving factors in determining the overall noise performance, a situation where the flight hardware is detached must also be considered. Since the vehicle is powered by electric motors for most of the road phase, noise produced by the internal combustion engine is not a major factor in determining the noise performance of the car. Even when the battery eventually runs out (after about 100km) and the engine has to be switched on to charge it, it will be significantly quieter than a normal car with an internal combustion engine. This is because the engine does not have any mechanical connection to the wheels, lacks a gearbox and runs at a constant RPM whilst powering the generator.

The noise produced by the engine is insignificant compared to the two other major noise sources:

- **Tyre noise**

This source of noise is primarily caused by the roughness of the tyre tread which is required to provide grip (tread noise), as well as the pressurised cavity between the metal wheel and rubber inner tyre (tyre cavity noise). The latter is particularly annoying, causing a relatively low-frequency noise between 200-250Hz which is low enough for it to cause structural vibrations in the vehicle as well as being audible for passengers and outside observers. (O'Boy and Walsh, 2016)

- **Aerodynamic noise**

This source of noise arises from a variety of geometric aspects of the vehicle. Any abrupt transition in geometry can cause pressure drops and spikes which emit noise at various frequencies. Open sunroofs and side windows are particularly serious offenders, as well as the wheel wells which form serious geometric discontinuities in the aerodynamic shape of the car. (SAE International, 2016)

Without complex wind tunnel testing, it is not possible to make an accurate estimation of the aerodynamic noise generated by the vehicle under consideration. However, the vehicle is expected to meet road noise standards since the primary noise contributor in gas-powered cars, the internal combustion engine, will not actually be used most of the time. Only when driving over 100km on a full charge will the internal combustion engine kick in, producing much less noise than a conventional car because of engine placement and optimisation for a specific engine/generator RPM.

5.2. Aerodynamics

In this section, the aerodynamic characteristics of the vehicle are determined, in particular the wing and the fuselage as the sizing of the tail is specified in section 5.3. The wing parameters are determined and the lift, drag and moment coefficients are calculated and presented in the form of curves for cruise, landing and take-off configurations.

5.2.1. Wing Planform

For the wing design, some parameters have to be decided before calculating the rest. These parameters are the aspect ratio (A) and the taper ratio (λ). For the Aspect ratio, a value of 17 is assumed which was influenced by Stoll et al. (2014). For the taper ratio, it is assumed to be 0.8 due to structural failure calculations from section 5.4. Furthermore, it is decided that the trailing edge has no sweep ($\Lambda_{TE} = 0$).

From the wing loading diagram in section 5.1, a value of 8.414 m^2 was obtained for the wing area (S). Using this value and the aspect ratio, the root chord, tip chord, mean aerodynamic chord and sweep of the wing can be calculated (Steenhuizen and Elham, 2015b):

$$b = 2 \cdot S \frac{(1 + \lambda)}{c_r} = 11.96, \quad (5.2)$$

$$C_r = \left(\frac{A \cdot (1 + \lambda)}{2b} \right)^{-1} = 0.782 \text{ m} \quad (5.3)$$

$$\bar{C} = \frac{2C_r}{3} \cdot \left(\frac{1 + \lambda + \lambda^2}{1 + \lambda} \right) = 0.706 \text{ m} \quad (5.4)$$

$$\Lambda_{LE} = \tan^{-1} \left(\frac{C_r - C_t}{b/2} \right) = 1.50^\circ \quad (5.5)$$

$$\Lambda_{0.25C} = \tan^{-1} \left(\tan(\Lambda_{LE}) - \left(\frac{C_r}{2b} \right) \cdot (1 - \lambda) \right) = 1.12^\circ \quad (5.6)$$

$$\Lambda_{0.5C} = \tan^{-1} \left(\tan(\Lambda_{LE}) - \left(\frac{C_r}{b} \right) \cdot (1 - \lambda) \right) = 0.749^\circ \quad (5.7)$$

A render of the wing can be seen in fig. 5.8 with the calculated wing parameters.

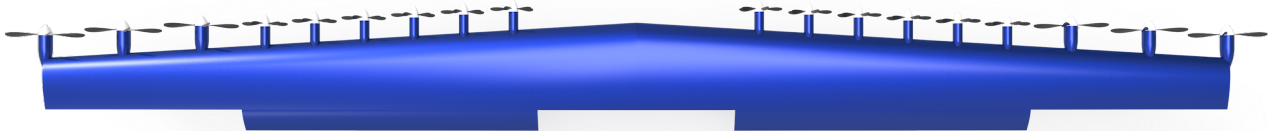


Figure 5.8: Representation of the Wing Design

5.2.2. Airfoil Selection

The selection of an adequate airfoil impacts numerous phases of flight and will affect the eventual aircraft parameters significantly. The airfoil will impact the aerodynamic efficiency during all phases of flight, whilst simultaneously contributing to changes in cruise speed and take-off/landing distances amongst other things. This section will discuss the airfoil selection, both of the wing and tail, and discuss the consideration that went into the process.

When considering the airfoil geometry, the most important parameters to consider are the airfoil's camber and thickness to chord length ratio (t/c). The camber of an airfoil refers to its geometric curvature and is expressed as the maximum distance between the chord line and the mean camber line as a percentage of the chord length. The introduction of camber prevents the separation of the airflow, hence reducing drag and increasing lift. Furthermore, due to camber, the circulation of the airflow is increased, which in turn increases the lift compared to non-cambered airfoils. The t/c ratio refers to the maximum thickness of the airfoil divided by the chord length.

Typically, airfoil design is an inversely iterative process, using computational analysis to determine airfoil geometry based on desired pressure distributions along the airfoil. However, within the current detailed design stage, existing airfoils were considered for application. The National Advisory Committee of Aeronautics (NACA) created widely used airfoil families. The "four-digit" series represents one branch of these airfoils, with the first two digits referring to the percent camber and the location of maximum camber, respectively. The last two digits represent the maximum thickness as a percentage of chord length. Furthermore, the "five-series" and "six-series" NACA airfoils were introduced in order to consider shifts in maximum camber positions and laminar flow increase, respectively. The airfoil chosen will be from either the NACA four or five series, as the six-series are more typically used for high-speed-wing design (Raymer, 1999).

The most important consideration for the airfoil selection was considered to be the airfoil's lift to drag ratio. With a relatively low wing surface area, the lift characteristics of the foil have to allow for enough lift to be generated during the specific flight stages. Furthermore, stall characteristics and structural evaluation were considered when determining an appropriate t/c .

Consulting an online database tool¹⁰ for common four-and-five-series NACA airfoils, a variety of different airfoils could be evaluated. By choosing an array of different foils, and comparing their aerodynamic characteristics against one another, the optimal airfoil can be determined. This airfoil will then be analysed once again for different t/c ratios, concluding the detailed design airfoil selection. Figure fig. 5.9 depicts the five common airfoils which were evaluated for their lift and drag characteristics. From these airfoils, the NACA 4418 performed best with respect to lift and drag capabilities. Therefore, the 4418 foil will be analysed and evaluated at different t/c in fig. 5.10.

For the evaluation of the aerodynamic characteristics of the NACA airfoils, two programs were used, which are Xfoil¹¹ and XFLR5¹². Moreover, the airfoil database, Airfoil Tools, supplied individual foil analysis for low Reynolds numbers. Although XFLR5 and Airfoil Tools use Xfoil style analysis for airfoils, the outcomes of different analyses were still compared to one another to verify the results. Furthermore, the resultant airfoil characteristics from Xfoil and XFLR5 analysis were validated using windtunnel test results presented in both Raymer (1999) and Abbott and Doenhoff (1959). The results from actual testing varied slightly from the conducted analyses, with the Xfoil and XFLR5 typically being more "optimistic" in terms of maximum lift coefficients. However, this was applicable to all airfoils analysed with Xfoil, thus the correlations established between profiles was upheld by the physical windtunnel test results. Throughout the aerodynamic analysis, the aerodynamic characteristics of the windtunnel testing will be used in order to ensure analysis at the more extreme set of available data. Furthermore, the physical representation of the airfoil is more appropriate to choose when designing and sizing the vehicle.

From fig. 5.10, it is clear that the 4412 airfoil displays the best lift over drag characteristics. However, considering the slenderness of the wing geometry, structural analysis and evaluation deemed this airfoil impractical. Either extremely large deflections were predicted under the most critical load cases, or the wingbox structure would be unreasonably heavy. This is explained further in section 5.4. By increasing the thickness of the airfoil, however, the flow tends to separate from the trailing edge. This typically results in a more gradual lift decrease due to flow separation from increasing the angle of attack. This gradual increase in boundary layer separation results in less severe stall characteristics.

For the wing, morphing airfoils was also considered throughout the design stage. This was primarily considered practical due to the implementation of Distributed Electrical Propulsion. With different propellers inducing accelerated airflows over different section of the wing, the airfoils could be optimised more specifically for each stage. Within the current design stage, however, analysis deemed that usage of the NACA 4418 over the entire wing was sufficient. This reduced complexity of the calculations and computational programs. For future analysis, however, implementing different airfoils along the wing could optimise the aircraft's performance capabilities.

The airfoil that will be implemented and considered throughout the remainder of the Aerodynamic analysis will therefore be the NACA 4418.

5.2.3. Lift

For this model, it is assumed that all of the lift is generated by the wing instead of a part coming from the fuselage. Therefore, the focus will be on the wing for lift modelling. To model this lift, the DATCOM method is used (Steenhuizen and Elham, 2015a). From section 5.1, the Mach number at the 3 configurations is 0.25, 0.0915 and 0.11 for

¹⁰airfoiltools.com, Retrieved on 20 January, 2018

¹¹<http://web.mit.edu/drela/Public/web/xfoil/>, (Retrieved on 20 January 2018)

¹²www.xflr5.com, (Retrieved on 20 January, 2018)

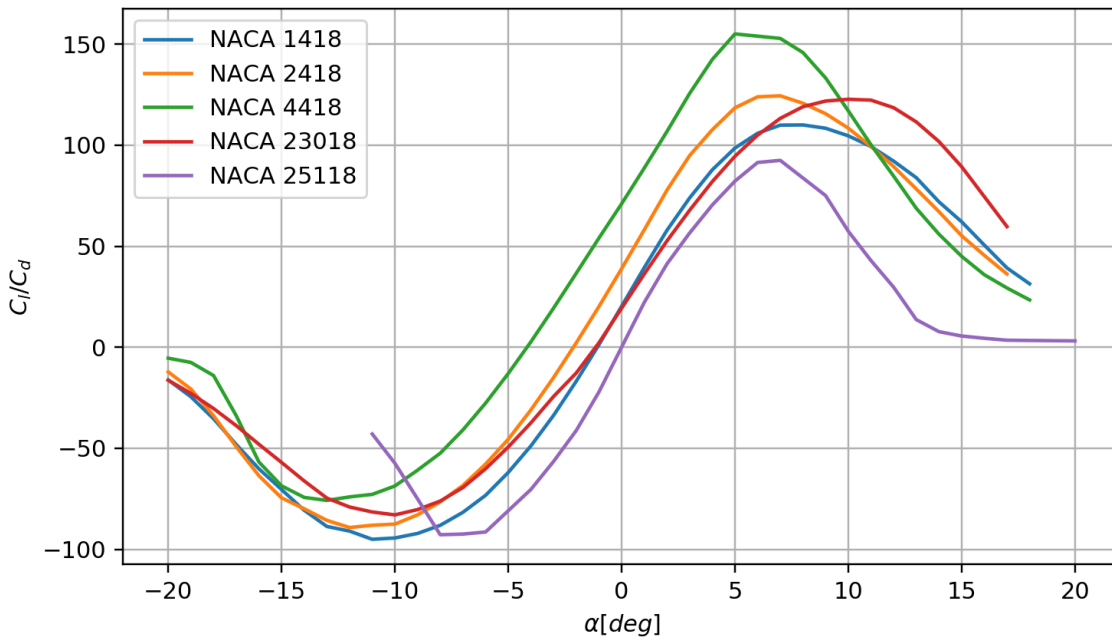


Figure 5.9: $\frac{C_L}{C_D}$ plotted against Angle of Attack for several NACA four and five digit series

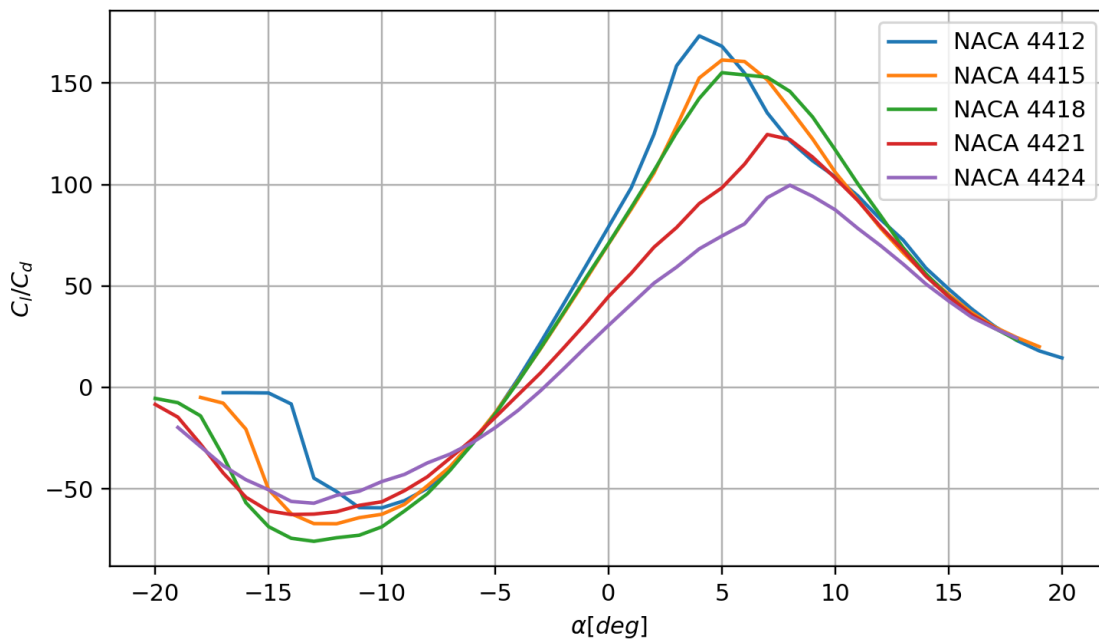


Figure 5.10: $\frac{C_L}{C_D}$ plotted against Angle of Attack for the NACA 4412-4424 airfoils

cruise, landing and take-off configuration, respectively.

For cruise configuration, only the tip propellers are on. As they give a small DEP effect, this can be neglected and therefore a clean wing is modelled at cruise configuration. the gradient of the cruise configuration lift curve is:

$$C_{L\alpha} = \frac{2\pi \cdot A}{2 + \sqrt{4 + \left(\frac{A\beta}{0.95}\right)^2 \cdot \left(1 + \frac{\tan^2(\Lambda_{0.5c})}{\beta^2}\right)}} = 0.0935/\circ \quad (5.8)$$

Throughout the computation of the clean wing lift characteristics, the software XFLR5 was used for verification purposes. Besides analysing airfoils, XFLR5 can be used to model the wing. Numerically, the program can then calculate the lift and the induced drag. Although the software is more efficiently used on thin airfoil (as the viscous effects fail to translate with 3D wing modelling), the tool is used throughout the analysis to guarantee accuracy of the calculations on the clean wing. Verifying results with DEP effects go beyond the limits of this program, with extensive future Computational Fluid Dynamic analysis being strongly advised. Furthermore, all calculations have been thoroughly calculated manually, to ensure mistakes were filtered from the process. The value for $C_{L\alpha}$ computed through XFLR5 was 0.0939, verifying eq. (5.8).

Using the airfoil data and the graphs from the DATCOM method which takes into account Mach number and sweep, the maximum lift coefficient of the clean wing ($C_{L_{max, clean}}$) is 1.296. Using this value and the gradient, the stall angle (α_s) can be determined:

$$\alpha_s = \frac{C_{L_{max, clean}}}{C_{L\alpha}} + \alpha_0 + \Delta\alpha_{C_{L_{max}}} = 11.96^\circ \quad (5.9)$$

As $\Delta\alpha_{C_{L_{max}}}$ takes into account the non-linear effects of the lift curve (Steenhuizen and Elham, 2015a), this will be neglected during modelling as the actual C_L values can only be obtained through experimentation. Therefore, in this case, the lift curve will be modelled to stall (α_s) at an angle of 9.86° .

For the flapped configuration, it is decided that a single fowler flap is used. For the landing configuration, the flaps will deploy at an angle of 40° and for the take-off configuration at 10° . The flaps cover 40% of the chord. From this, the increased chord length (c') and the reference wing flapped surface ratio (Swf/S) can be determined. For landing and take-off configuration, the increased chord length are, respectively, 1.244 m and 1.18 m. For both configurations, the reference wing flapped surface ratio is 0.511. Using these values, the gradient of the flapped wing curve for landing and take-off configuration are:

$$C_{L\alpha, flapped, landing} = C_{L\alpha} \cdot \left(\frac{S'}{S}\right)_{landing} = C_{L\alpha} \cdot \left(1 + \left(\frac{Swf}{S}\right) \cdot \left(\frac{c'}{c} - 1\right)\right)_{landing} = 0.105 \quad (5.10)$$

$$C_{L\alpha, flapped, take-off} = C_{L\alpha} \cdot \left(\frac{S'}{S}\right)_{take-off} = C_{L\alpha} \cdot \left(1 + \left(\frac{Swf}{S}\right) \cdot \left(\frac{c'}{c} - 1\right)\right)_{take-off} = 0.102 \quad (5.11)$$

The new maximum lift coefficient for landing ($C_{L_{max, flapped, landing}}$) and take-off ($C_{L_{max, flapped, take-off}}$) are determined by the increase in lift from the flaps. For landing and take-off, the increase in lift are:

$$\Delta C_{L_{max, landing}} = 0.9 C_{l_{max, landing}} \cdot \frac{Swf}{S} \cdot \cos\Lambda_{hinge_line} = 0.743 \quad (5.12)$$

$$\Delta C_{L_{max, take-off}} = 0.9 C_{l_{max, take-off}} \cdot \frac{Swf}{S} \cdot \cos\Lambda_{hinge_line} = 0.705 \quad (5.13)$$

Where $C_{l_{max}}$ is the local lift of the flaps when deployed and Λ_{hinge_line} is assumed to be parallel to the trailing edge and is therefore 0° .

Knowing the new maximum lift coefficients and the gradients, the stall angle of the landing and take-off configurations can be found:

$$\alpha_{s, landing} = \frac{C_{L_{max, flapped, landing}}}{C_{L\alpha_{flapped, landing}}} + \alpha_{0_{landing}} + \Delta\alpha_{C_{L_{max}}} = 9.83^\circ \quad (5.14)$$

$$\alpha_{s, take-off} = \frac{C_{L_{max, flapped, take-off}}}{C_{L\alpha_{flapped, take-off}}} + \alpha_{0_{take-off}} + \Delta\alpha_{C_{L_{max}}} = 12.59^\circ \quad (5.15)$$

For the same reasons as the stall angle at cruise, the non-linear effects are neglected and the modelled stall angle for landing and take-off configuration will be, respectively, 7.73° and 10.49° . The reason that the stall angles differ quite largely in landing and take-off configuration is because of the difference between α_0 at landing and take-off. This angle of attack is calculated with:

$$\alpha_{0_{flapped}} = \alpha_0 + \Delta\alpha_0 = \alpha_0 + \Delta\alpha_{0_{airfoil}} \cdot \frac{Swf}{S} \cdot \cos\Lambda_{hinge_line} \quad (5.16)$$

Where $\Delta\alpha_{0_{airfoil}}$ is -15° at landing and -10° at take-off. From this, the zero lift angle of attack (α_0) at landing and take-off are, respectively, -11.66° and -9.11° .

To model DEP, it is decided that it would act as a leading edge high lift device that raises the landing and take-off curves by a increased lift due to DEP ($\Delta C_{L_{DEP}}$). The following assumptions are made when modelling DEP:

- The gradient of the curves are constant
- The stall angles of attack are constant
- The zero lift angles of attack are constant
- The C_L values increase by $\Delta C_{L_{DEP}}$

To calculate how much lift DEP gives, a velocity triangle approach is taken. The DEP engines are at a slightly different angle to the wing and therefore give an increase in speed at a different angle to the free stream velocity (V_∞). Therefore, the new velocity (V_2) after passing the propeller is:

$$V_2 = V_\infty + \frac{T_p}{\dot{m}} = V_\infty + \frac{T_p}{\rho \cdot A_p \cdot V_p} = V_\infty + \frac{T_p}{\rho \cdot A_p \cdot \left(\frac{V_\infty + V_2}{2}\right)} \rightarrow V_2 = \sqrt{V_\infty^2 + \frac{2T_p}{\rho \cdot A_p}} \quad (5.17)$$

To simplify this approach, the wing is split into 3 sections, the tip where the 3 large propellers are, the middle where the 6 small propellers are and the root where there are no propellers. For this reason, the thrust setting and propeller area change and therefore, V_2 changes as well. The value for V_2 at the tip and middle for landing and take-off configuration are:

Table 5.9: V_2 at the middle and tip section of the wing

Configuration	V_2 (tip)	V_2 (middle)
Landing	-	46.78 m/s
Take-off	48.90 m/s	51.52 m/s

As the speed increases, the wake area decreases. To take this effect into account, this factor (F_{wake}) is multiplied by the pressure effect (V_2/V_∞)² and is called the DEP factor (F_{DEP}). This factor is calculated using eq. (5.18):

$$F_{DEP} = F_{wake} \cdot \left(\frac{V_2}{V_\infty}\right)^2 = \sqrt{\frac{V_\infty}{V_2}} \cdot \left(\frac{V_2}{V_\infty}\right)^2 \quad (5.18)$$

The value for the DEP factor in landing and take-off configurations are:

Table 5.10: F_{DEP} at the middle and tip section of the wing

Configuration	F_{DEP} (tip)	F_{DEP} (middle)
Landing	-	1.68
Take-off	1.48	1.60

This DEP factor is then multiplied by their respective lift coefficient and wing section areas which differs as the tip and root experience the lift from the clean wing whereas the middle section is fully flapped. Therefore, when calculating the lift for the middle section, Swf/S is assumed to be 1. Also, for the sections influenced by DEP, the area around the engines that has been excluded due to the wake effects are still affected by the free stream velocity. To take this into account, a free stream factor product of the decrease in wake diameter, the respective lift coefficient and wing section area is added to the initial product:

$$C_{L_{S_{DEP}}} = C_L \cdot S_{section} \cdot F_{DEP} \quad (5.19)$$

$$C_{L_{S_{free}}} = C_L \cdot (1 - F_{wake}) \cdot S_{section} \quad (5.20)$$

$$C_{L_{S_{local}}} = C_{L_{S_{DEP}}} + C_{L_{S_{free}}} \quad (5.21)$$

The values for the product for each configuration are:

Table 5.11: $C_{L_{S_{local}}}$ at the root, middle and tip section of the wing

Configuration	$C_{L_{S_{local}}}$ (tip)	$C_{L_{S_{local}}}$ (middle)	$C_{L_{S_{local}}}$ (root)
Landing	2.82	24.41	2.07
Take-off	3.88	16.61	1.725

Now that the product of the respective lift coefficients and their wing sections are found, the total lift coefficient of the entire wing can be calculated by summing up the products and dividing it by the total wing area. However, the effect of DEP might give an optimistic value of the total lift coefficient (Stoll et al., 2015) so a safety factor of 0.9 is taken into account.

$$C_{L_{total}} = 0.9 \frac{\sum(C_{L_{S_{local}}})}{S} \quad (5.22)$$

Finally, to calculate $\Delta C_{L_{DEP}}$, The flapped C_L values for both configurations at their respective angles of attack are deducted from the $C_{L_{total}}$ values calculated in eq. (5.22):

$$\Delta C_{L_{DEP}} = C_{L_{total}} - C_{L_{flapped}} \quad (5.23)$$

The values of $\Delta C_{L_{DEP}}$ for landing and take-off configuration are, respectively, 1.305 and 0.638. Now that all the necessary lift parameters are found, the lift curves can be modelled. Using the DATCOM method, the lift curves for all three configurations are:

$$C_{L_{cruise}} = C_{L_{\alpha}} \cdot (\alpha - \alpha_0) \quad (5.24)$$

$$C_{L_{landing}} = C_{L_{\alpha, flapped, landing}} \cdot (\alpha - \alpha_{0_{landing}}) + \Delta C_{L_{DEP, landing}} \quad (5.25)$$

$$C_{L_{take-off}} = C_{L_{\alpha, flapped, take-off}} \cdot (\alpha - \alpha_{0_{take-off}}) + \Delta C_{L_{DEP, take-off}} \quad (5.26)$$

5.2.4. Drag

It is essential to approximate the drag characteristics of the vehicle under different flight phases. To estimate this, the zero-lift drag coefficient must be determined, after which the lift induced drag contribution can be incorporated. In order to predict the vehicle's drag, the following two methods can be followed:

1. Calculate the zero-lift drag coefficient based on equivalent skin-friction drag.
2. Calculate the zero-lift drag coefficient by analysing individual drag components.

The first method considers the equivalent skin-friction coefficient C_{f_e} of the vehicle, which consists of separation pressure drag and skin-friction. Typically, a well designed aircraft will experience these two forms of drag throughout subsonic cruise. Therefore, by multiplying the skin-friction coefficient to the ratio of the vehicle's wetted surface area (S_{wet}) to the reference wing area (S_{ref}), as shown in eq. (5.27), the parasitic drag can be approximated.

$$C_{D_0} = C_{f_e} \frac{S_{wet}}{S_{ref}} \quad (5.27)$$

Using a C_{f_e} value of 0.005 obtained from Raymer (1999), the first prediction of C_{D_0} is calculated to equal 0.03163.

The method of analysing the drag build-up due to individual drag components is more accurate and precise than relying on the equivalent skin-friction drag approximation. Furthermore, it is a commonly applied drag estimation method, used in Raymer (1999) Roskam (2000b) and Williams et al. (1978). The parasitic drag is calculated using the flat plate friction coefficient (C_f) relevant for the specific drag component. These friction coefficients vary according to the relative Reynolds number and can be determined from Fig. 4.3 from Roskam (2000b). Furthermore, a Form Factor (FF) approximates the streamlined shape of the component and accounts for pressure drag due to flow separation. For every component, interference drag is also considered in terms of an Interference Factor (Q). As shown in eq. (5.28), multiplying C_f , FF , and Q with the component's wetted area, S_{wet} , the summation of all drag components will provide the vehicle's zero-lift drag coefficient.

$$C_{D_0} = \sum C_{D_{0, component}} = \frac{\sum C_f \cdot FF \cdot Q S_{wet}}{S_{ref}} \quad (5.28)$$

The components that will be evaluated individually, will be the wing, fuselage group, horizontal and vertical stabilisers, and the nacelles. In order to determine the form factors of the wing and fuselage, the following expressions are

considered, respectively:

$$FF_w = (1.0 + L' \frac{t}{c} + 100 \frac{t^4}{c}) \quad (5.29)$$

$$FF_{fus} = (1 + \frac{60}{l_f^3} + 0.0025 \frac{l_f}{d_f}) \quad (5.30)$$

With L' representing the airfoil thickness location parameter, $\frac{t}{c}$ being the thickness ratio of the airfoil at the mean geometric chord, and l_f and d_f representing the fuselage length and maximum fuselage equivalent diameter, respectively. For the horizontal and vertical stabilizers, it is assumed that the Form Factor can be approximated as a wing, while the nacelles are modelled as tiny fuselages.

Through approximation of the interference factors and calculating the component surface areas based on its geometry and validating it through the SolidWorks model, the following C_{D_0} values were determined:

Table 5.12: The individual drag components and the overall resultant C_{D_0} of the vehicle

Component	Wing	Fuselage	Horizontal Stabiliser	Vertical Stabiliser	Nacelles	Total
C_{D_0}	0.0114	0.0165	0.00332	0.00165	0.000931	0.0338

The final value of 0.0338 for the vehicle's zero-lift drag coefficient is within an acceptable range of the value obtained from the first approximation method. This verifies that the estimation techniques are comparable and that the drag component estimation method is within a reasonable value range. Moreover, in order to effectively perform further calculations, the drag values estimated have been conservatively estimated. Using overestimated values for factors such as the skin-friction drag and surface area exposed to the airflow, component drag factors are considered slightly higher than in reality.

Furthermore, due to the extension of the flaps at landing and take-off, extra drag is generated. A drag increment due to the profile, lift-induced, and interference drag are instigated through the deployment of the flaps at different stages. In take-off configuration, the vehicle will extend its flaps by 10%, while at landing the flaps are extended at 40%. Furthermore, the flaps are considered to be the size of 40% of the wing chord, with a resultant ratio of wetted surface area to wing area of 0.511. Therefore, using drag increment approximations from Raymer (1999), the increase in drag due to flap extension in take-off and landing will be 0.0408 and 0.0867.

In order to approximate the induced drag due to lift, the Oswald Efficiency factor must be determined. The Oswald Efficiency factor, e , takes the vehicle's deviation from an ideal elliptical lift distribution into account. Using different approaches and equations provided in Nita and Scholz (2012), and taking the average factor as a final value, the Oswald factor was determined to be 0.59.

Using the values obtained in the lift and drag calculations, the relationships between them can be represented. This can be seen in fig. 5.11:

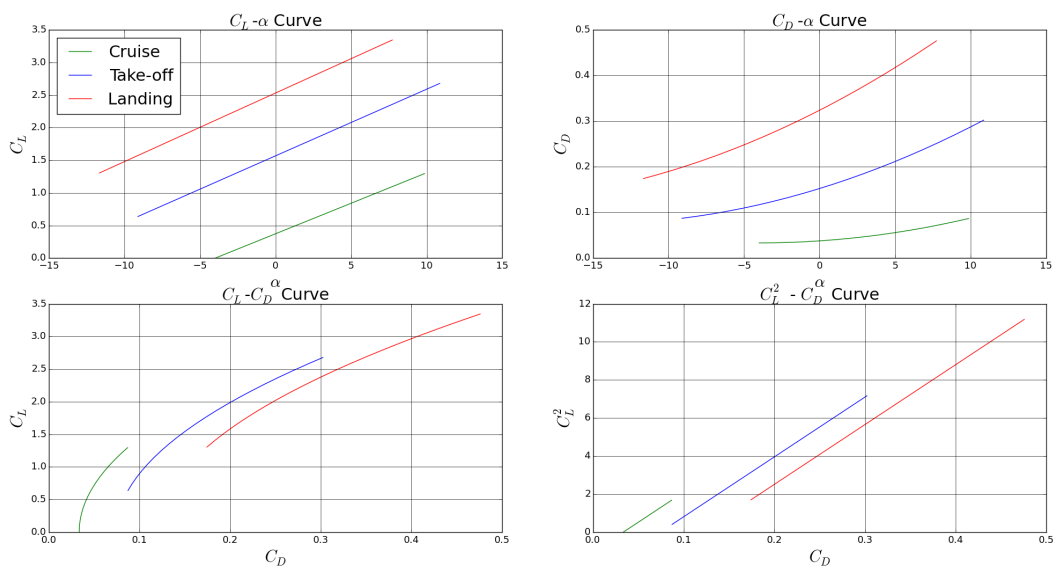


Figure 5.11: Lift and Drag Curves

The most important parameters from these curves can be found in:

Table 5.13: Lift and Drag Parameters

Configuration	C_L	C_D	α	L/D
Cruise	0.561	0.0434	2.0	12.93
Landing	3.09	0.399	9.0	7.74
Take-off	2.37	0.250	8.0	9.48

Now that the parameters are found, it is necessary to make sure that they are correct. To do this, the parameters must be validated. To validate this, several reference aircraft¹³ (Filipone, 2000) are investigated (the data can be found in appendix A) and their values for lift and drag are compared to the product's. The comparison can be seen in table 5.14. The first flight data consists of general aviation aircraft. As this flight data is only available for cruise, a second flight data is used as well which consists of larger aircrafts but has data for all configurations.

Table 5.14: Lift and drag validation

Configuration	Numerical Data	Flight Data 1	% Error 1	Flight Data 2	% Error 2
C_L (Take-off)	2.37	-	-	1.04	128.9
C_L (Cruise)	0.561	0.405	38.52	0.510	9.94
C_L (Landing)	3.09	-	-	1.20	158.5
C_D (Take-off)	0.25	-	-	-	-
C_D (Cruise)	0.0434	0.0356	21.91	0.0424	2.29
C_D (Landing)	0.399	-	-	0.0616	548.0
L/D (Take-off)	9.48	-	-	-	-
L/D (Cruise)	12.93	12.53	3.19	12.03	7.48
L/D (Landing)	7.74	-	-	19.5	60.3

As evident in the % errors, the values differ greatly for take-off and landing configuration. This was expected as the product has DEP during those configurations and therefore a higher C_L and C_D than the reference aircraft used. If the aircraft in Stoll et al. (2014) was used, for example, their $C_{L_{max}}$ in landing configuration is 5.2 due to DEP. Comparing the numerical data with this reference aircraft, the % error for C_L in landing configuration is 40.6%. This is a much larger improvement than when it was compared to the standard reference aircraft. Another reason for the great differences is the fuselage. The product is shaped as a road vehicle so it is not completely optimised for flight like the

¹³http://www.dept.aoe.vt.edu/~mason/Mason_f/CessnaCitationIIBravo.pdf

reference aircraft. This explains the large drag coefficients in landing and take-off configuration. Finally, the reference aircrafts have different thrust and speed settings at each configuration when compared to the product, thereby having different values.

5.2.5. Moment

Before the moment curves can be modelled, the zero lift pitching moment coefficient of the clean wing ($C_{m_{0,w}}$) needs to be known. In order to calculate this, the airfoil C_{m_0} of -0.105 from the airfoil data and eq. (5.31) are used (Roskam, 2000b):

$$C_{m_{0,w}} = C_{m_0} \cdot \left(\frac{A \cos^2(\Lambda_{0,25C})}{A + 2 \cos(\Lambda_{0,25C})} \right) = -0.0939 \quad (5.31)$$

Using this value, the position of the aerodynamic centre from section 5.3 and Roskam's method (Roskam, 2000b), the pitching moment coefficient for the clean wing in cruise configuration is modelled as:

$$C_{m_{cruise}} = C_{m_{0,w}} + C_{L_{cruise}} \cdot \left(\frac{x_{ref} - x_{ac}}{\bar{C}} \right) \quad (5.32)$$

From eq. (5.32), the aerodynamic centre moment coefficient ($C_{m_{ac}}$) can be found by equating x_{ref} and x_{ac} which results in $C_{m_{0,w}}$. Therefore, ($C_{m_{ac}}$) and $C_{m_{0,w}}$ are equal.

For the landing and take off configurations, the increase in moment coefficient ($\Delta C_{m_{landing}}$ and $\Delta C_{m_{take-off}}$) are also calculated using Roskam's method (Roskam, 2000b):

$$\Delta C_{m_{landing}} = C_{l_{max,landing}} \cdot \left(\frac{x_{ref}}{\bar{C}} - \frac{x_{cp}}{\bar{C}} \left(\frac{c'}{c} \right) \right) = -0.711 \quad (5.33)$$

$$\Delta C_{m_{take-off}} = C_{l_{max,take-off}} \cdot \left(\frac{x_{ref}}{\bar{C}} - \frac{x_{cp}}{\bar{C}} \left(\frac{c'}{c} \right) \right) = -0.675 \quad (5.34)$$

Therefore, the pitching moment coefficient for landing and take-off configuration are:

$$C_{m_{landing}} = C_{m_{0,w}} + C_{L_{flapped,landing}} \cdot \left(\frac{x_{ref} - x_{ac}}{\bar{C}} \right) + \Delta C_{m_{landing}} \quad (5.35)$$

$$C_{m_{take-off}} = C_{m_{0,w}} + C_{L_{flapped,take-off}} \cdot \left(\frac{x_{ref} - x_{ac}}{\bar{C}} \right) + \Delta C_{m_{take-off}} \quad (5.36)$$

From these two equations, the aerodynamic centre pitching moment coefficient for landing and take-off configuration are, respectively, -0.805 and -0.769. Using these values, the relationship between the pitching moment and the lift coefficient, the angle of attack and the speeds can be represented. These relationships can be seen in fig. 5.12. The most important parameters from these curves can be found in table 5.15:

Table 5.15: Moment Parameters

Configuration	$C_{m_{ac}}$	C_m	V [m/s]
Cruise	-0.0939	-0.252	82.3
Landing	-0.805	-1.25	37.6
Take-off	-0.769	-1.22	33.1

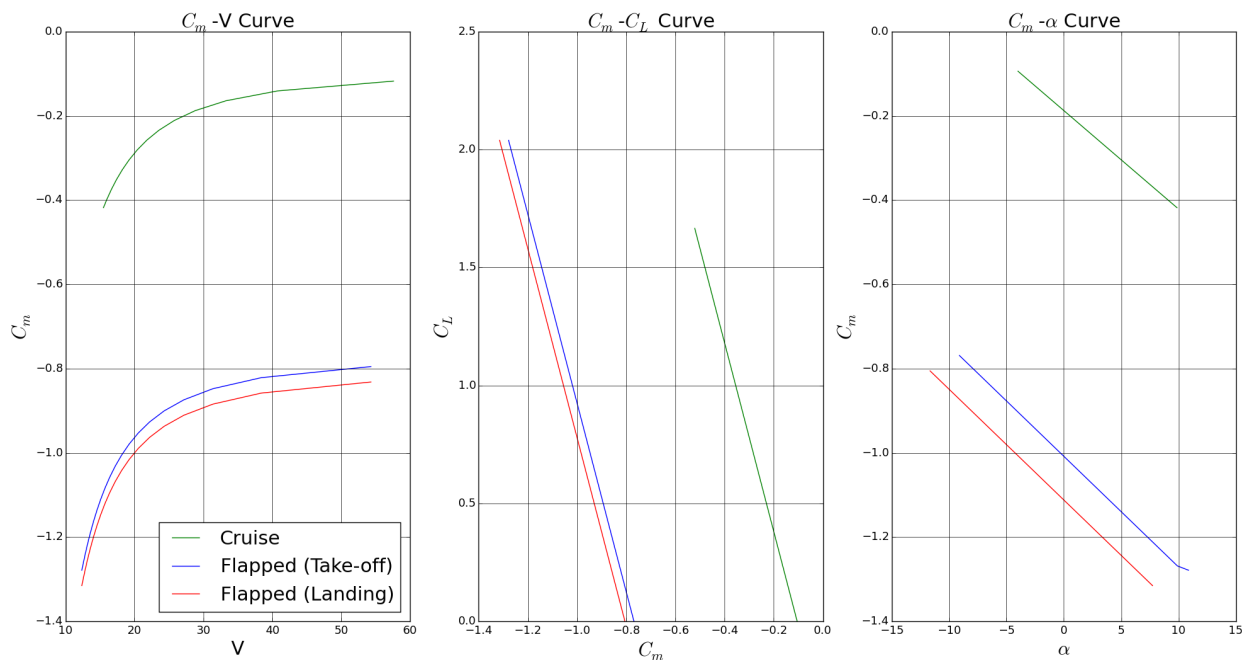


Figure 5.12: Moment Curves

5.3. Stability and Control

The aircraft needs to be balanced around all its axis and should be statically, and dynamically stable for the full range of centre of gravity locations. Furthermore, it must be possible to trim the aircraft during critical control situations. During the design option phase it was concluded that a T-tail configuration has to be used. For linkage purposes a high wing design was selected. On this high wing design a large amount of propellers are located due to DEP, which increases the downwash gradient. The larger this downwash gradient, the less effective the tail. In order to move the tail as far as possible outside this region of influence a T-tail was chosen. Using input from section 5.1 and section 5.2, the planform of the horizontal, and vertical stabiliser can be determined using Class I and Class II calculations. For the sizing of the controls a Class I estimation will be used. The objective of the empennage design is to meet the requirements on stability and control set by EASA with the least amount of weight.

This section will start in section 5.3.1 by discussing the packaging of the car and the assumptions used in the c.g. analysis. Section 5.3.2 will discuss the c.g. of the operative empty weight of the car, the c.g. range during operation of the vehicle and the tip-over stability. Section 5.3.3 will discuss these aspects for the flight configuration. Section 5.3.4 discusses the analysis performed to arrive at a surface area for the horizontal stabilizer. Subsequently, the planform of the vertical stabiliser will be selected. This will be continued by an estimation of the stability derivatives. Finally, the required rudder and aileron size will be determined.

5.3.1. Centre of Gravity Location

Once the weight of each component was known, the centre of gravity could be determined. This subsection discusses the assumptions made that were used in further analysis. Firstly, the assumptions used are stated. Secondly, the internal layout of the car is presented. The assumptions made when calculating the centre of gravity are listed below:

- For each of the components the c.g. was assumed to be in the middle of that components
- The centre of gravity of the chassis acts in the middle of the vehicle
- The reference point for defining x-locations is the nose, unless stated otherwise
- The reference point for defining z-locations is the ground, unless stated otherwise.

The centre of gravity of a vehicle can be calculated with eq. (5.37). The centre of gravity was calculated in (x,z) coordinates, as the vehicle is symmetric around the y-axis. All the components except the engine and generator are symmetric, however, the engine and the generator are placed in such a way that the resulting centre of gravity acts in

the symmetry axis.

$$x_{cg} = \sum \frac{W_i \cdot x_i}{W_i} \quad z_{cg} = \sum \frac{W_i \cdot z_i}{W_i} \quad (5.37)$$

Packaging of the car

Figures 5.13 and 5.14 show the internal lay-out of the car. This drawing is to scale, where 1 cm is equal to 0.25 m. The distances defined in the drawing are used in further analysis, section 5.4. The initial dimensions of the car were based on the Nissan Bladeglider¹⁴. A 1-2 seating configuration was selected. This would allow room for a luggage compartment in between the passengers. Furthermore, this would allow the shape of the vehicle to be more streamlined. The final dimensions of the car are a length of 4.5 m, a maximum width of 1.85 m and a height of 1.47 m with respect to the ground. The internal cabin height or the fuselage height is 1.3 m. This is within the dimensions stated in the requirements (chapter 3).

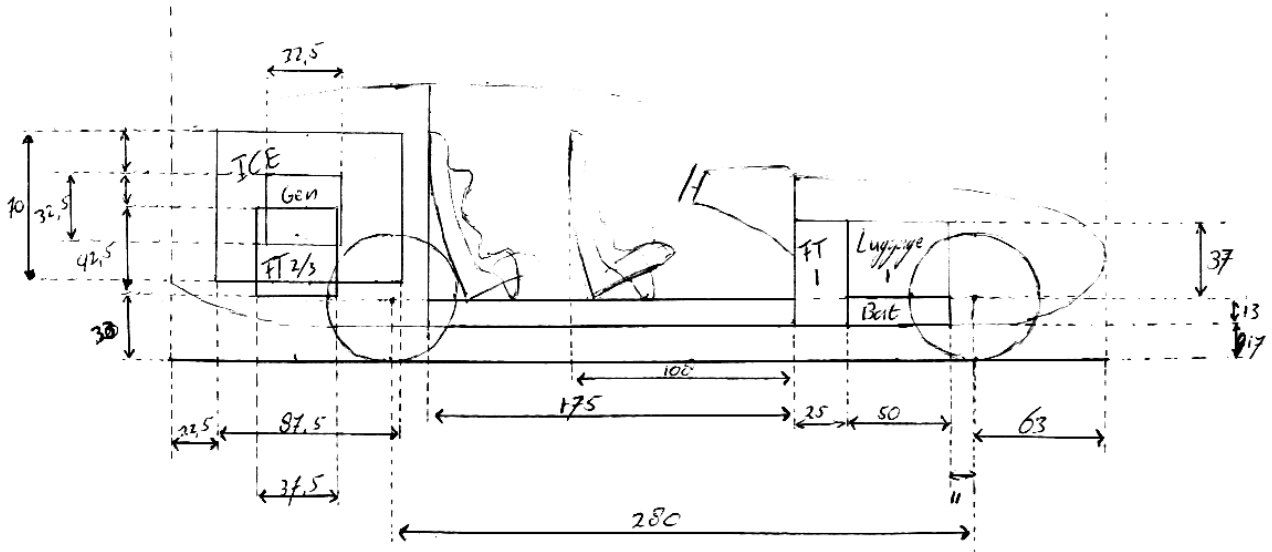


Figure 5.13: The side view of the car

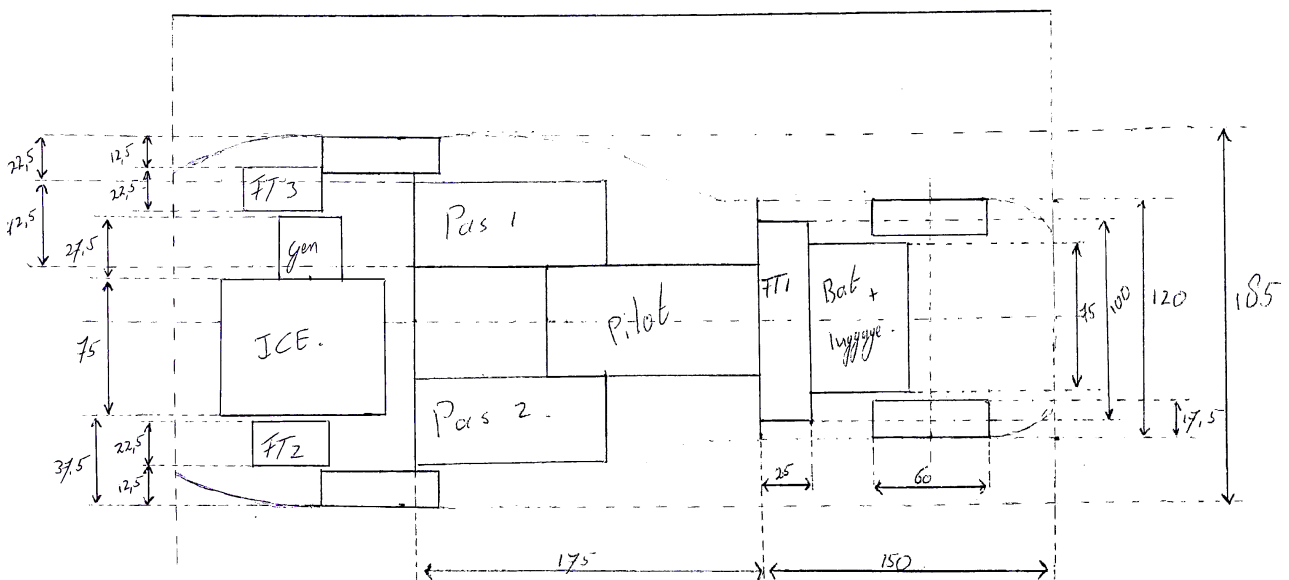


Figure 5.14: The topview of the car

¹⁴<https://www.topspeed.com/cars/nissan/2017-nissan-bladeglider-prototype-ar174021.html>, (Retrieved on 12 December 2017)

5.3.2. Road configuration

This subsection discusses the operative empty weight centre of gravity of the road configuration. After that, the centre of gravity range during operation will be explained. This subsection concludes with a tip-over analysis to make sure the vehicle in road configuration does not tip over when applying wheel thrust.

Operative empty weight centre of gravity

Once the packaging of the vehicle was decided upon, the operative empty weight c.g. location ($x_{cg,oew}$) for the road vehicle could be determined. In order to decrease the linkage complexity, the majority of components needed to fly will be present in the car. Furthermore, due to the concept of clip-on wings the wings are restricted to some extent in their movement forward. In order to achieve an acceptable tail size the centre of gravity of the car should be as far back as possible. This is the reason the engines and generator are placed in the back and there is not one big fuel tank in the front, but three fuel tanks in total of which two are located in the back. The fuel tanks have a capacity of 125, 36 and 36 L, combining to a total of 197 L. The fuel tanks have one shared fill cap. It was hence assumed that through a system of pumps and valves the fuel will always be evenly distributed throughout the tanks, such that there is a resulting c.g. of the fuel. This resulting value is shown in table 5.17. Furthermore, as the vehicle uses the wheels during take-off, rear wheel drive was employed. Therefore, the electromotors are at the rear wheels. Table 5.16 shows the masses and distances of each of the components used to calculate the $x_{cg,oew}$. The mass of avionics was added to the engine, as it was assumed that one part of the avionics will be in the car and the other part of the avionics will be in the tail, the resulting c.g. would act at the c.g. of the engine.

Table 5.16: Showing the mass and distance of each component, which was used for determining the centre of gravity of the car

Component	Mass [kg]	x_d [m]	z_d [m]
Engine	170.5	3.84	0.74
Generator	32.2	3.84	0.74
Driver seat	9.0	2.05	0.37
Passenger seats	2 · 9	2.825	0.37
Dashboard	38.0	1.5	0.74
Chassis	190	2.25	0.37
Fuel tank ₁	15	1.375	0.49
Fuel tank ₂	5	3.91	0.56
Fuel tank ₃	5	3.91	0.56
Electromotors	25	3.425	0.37
Batterypack	50	1.0	0.30

The mass of the skin and truss structure and other evenly distributed masses, such as cables, are not included in table 5.16, as it was assumed that they act at the centre of gravity and hence do not influence the position of the operative empty weight centre of gravity. All of this resulted in the $x_{cg,oew}$ of the car to be at 2.74 m, which is at 61% of the total car length. This is fairly aft, however the c.g. during flight configuration was deemed more important. The $z_{cg,oew}$ was found to be at 0.53 m. The total empty mass of the car is equal to 742 kg.

Centre of gravity range during operation

Table 5.17 shows the different masses of the payload/fuel used in the analysis and their corresponding distances with respect to the nose of the vehicle. Moreover, the front seat can be adjusted in such a way that it can accommodate 95% of all drivers, this was calculated by taking into account ergonomics and the required distance from the pedal to the c.g. of the driver.¹⁵ This is the reason that in further analysis a distinction is made between having the pilot in the most forward position or most aft position, as can be seen in table 5.17. When analysing the c.g. range the different position of the driver is taken into account for the different scenarios.

The most aft c.g. occurs when the driver is in the most aft position and brings along two passengers and their luggage, which is placed in the aft luggage compartment. This would result in a x_{cg} of 2.743 m, 61% of the car length, which is almost the same as the $x_{cg,oew}$ of the car. The most forward c.g. occurs when the driver is in the most forward position, luggage in the forward compartment and the tanks are filled with fuel. This would result in a x_{cg} of 2.6 m, 58% of the car length. Both cases show that the x_{cg} of the car does not vary a lot compared to the $x_{cg,oew}$. The x_{cg} in both cases is fairly aft, in order to enhance the driving experience, extra (dead) weight can be put in the front to artificially move

¹⁵<https://www.slideshare.net/sudhavel/basic-ergonomics-in-automotive-design>, (Retrieved on 19 December 2017)

Table 5.17: Showing the masses and their distances in both x-direction and z-direction

Loading	Mass [kg]	x_d [m]	z_d [m]
Driver/Pilot	100/77.4	-	-
-Most forward position		2.26	0.37
-Most aft position		2.44	0.37
Passenger	100	2.82	2.63
Luggage (a piece)	20	-	-
-Forward compartment		1.0	0.55
-Aft compartment		2.98	0.44
Fuel	121	2.30	0.51

the x_{cg} forward and put more load on the nose wheels.

The vertical (z-direction) c.g. range during operation is determined in similar fashion. The highest z_{cg} occurs when the driver is in the car and placed luggage in the front compartment. This result in a $z_{cg} = 0.51$ m. Deducting the ground clearance of 17 cm, the z_{cg} acts at 26% of the car (fuselage) height. The lowest z_{cg} occurs when the driver brings along two passengers and their luggage is placed in the aft luggage compartment. This results in a $z_{cg} = 0.48$ m. Deducting the ground clearance of 17 cm, the z_{cg} acts at 24% of the car (fuselage) height.

Tip-over stability

The most critical case occurs when the z_{cg} is at its highest point, $z_{cg} = 0.51$ m and $x_{cg} = 2.67$ m. In this case the arm with respect to the rear wheels is the largest. The analysis was performed at the moment the vehicle would accelerate from a stationary position. The main landing gear (rear wheels), x_{mg} , is at 3.425 m, the front gear (front wheels), x_{fg} is at 0.625 m. The friction coefficient, μ , is set to 0.02 as it is assumed that the car is driving on asphalt (Roskam, 1997c). The weight of the vehicle is 818 kg. The free body diagram is shown in fig. 5.15.

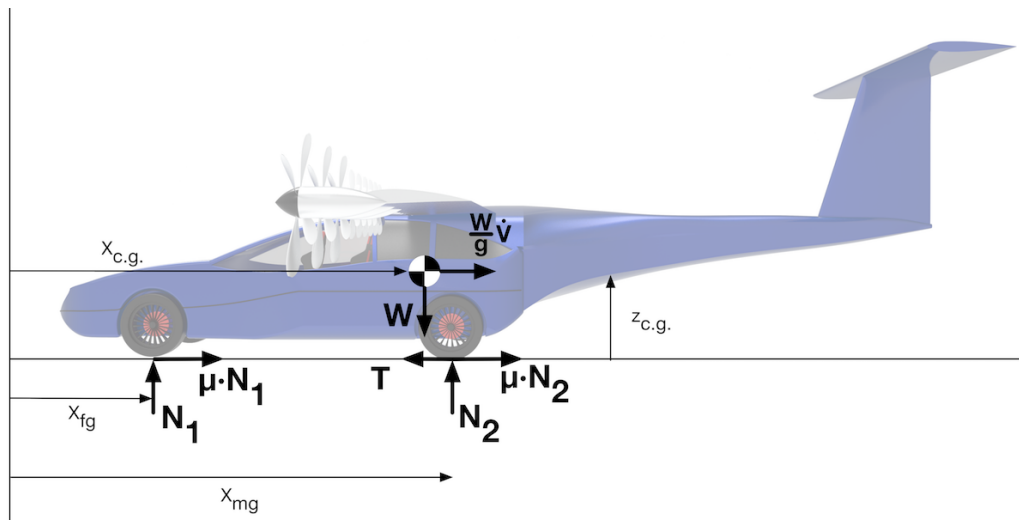


Figure 5.15: Free body diagram used in the tip-over stability analysis.

Based on this the maximum thrust the wheels can apply before tipping over is 5316 N, taken into account a positive margin for N_1 , defined in fig. 5.15. This is the thrust at which the wheels will start to slip. Therefore, in road configuration no limit has to be placed on the thrust the wheels are allowed to generate.

5.3.3. Flight configuration

This subsection discusses the operative empty weight centre of gravity ($x_{cg,oew}$) of the flight configuration, after which the c.g. range during operation will be explained. This subsection concludes with a tip-over analysis to make sure the vehicle in flight configuration does not tip over when applying wheel thrust. Before discussing the analysis for $x_{cg,oew}$ first two parameters necessary in this analysis, namely the length of the fuselage and the distance from the nose to the leading edge of the mean aerodynamic chord (XLEMAC) are explained.

In order to come up with an estimate for a total fuselage length, a statistical approach shown in Roskam (1997b) was used, which uses the fraction of fuselage length, divided by fuselage height, l_f/h_f . This fraction was between 5 and 8 for both twin-engine as well as single engine aircraft. Taking the value in the middle of this range, $l_f/h_f = 6.5$ and the pre-established height of the fuselage of 1.3 m, resulted in a fuselage length of 8.45 m. Comparing this with the length of reference aircraft such as the Cirrus SR22, 7.93 m, and the Tecnam P2006T, 8.7 m, which have a comparable fuselage height of about 1.27 m and 1.26 m respectively^{16, 17}, this fuselage length was deemed reasonable.

An initial estimate for the distance from the nose to the leading edge of the mean aerodynamic chord of the wing (XLEMAC) was set at XLEMAC = 3.1 m, this was based on the initial location of the linkage and the XLEMAC of the Cirrus SR22. This was deemed reasonable for linkage purposes and the most optimal wing location would come to light when plotting the c.g. range for varying wing locations as will be discussed later.

Operative empty weight centre of gravity

Normally the aircraft consists of a fuselage group and a wing group, however in this case the full configuration consists of the road hardware and the flight hardware. The flight hardware consists of the wing group and the tail group. In order to model it as a normal aircraft and to be able to vary the wing location with respect to the nose of the fuselage in further analysis, the wing and tail were taken separately. Firstly, the centre of gravity of the 'fuselage' was determined. This was done by taking the centre of gravity of the road configuration mentioned in the previous section and the centre of gravity of the tail group. The tail group consists of the linkage part, the tail boom and the tail itself. Table 5.19 shows the masses of the components and their distances with respect to the reference point. The distances for the linkage and tail boom centre of gravity were provided by the linkage department. For the empennage the following assumption was made:

- It is assumed that the x-location of the tail's centre of gravity acts 30% of the horizontal tailchord and the z-location acts at 75% of the height of the vertical tail. (Roskam, 1997b)

The x_{cg} of the tail part in x-z coordinates (5.76;1.67) measured with respect to the reference point. The resulting centre of gravity location for the fuselage in x-z coordinates (3.16;0.69) measured with respect to their reference point.

The wing group consists of the wing, the nacelles and the DEP propellers and engines. Table 5.18 shows the masses of the components and their distances with respect to the reference point. The assumptions made in determining the x and z distances are listed below:

- It is assumed that the x-location of the wing's centre of gravity acts at 42% of the MAC and the z-location acts at 50% of the thickness. (Roskam, 1997b)
- It is assumed that the x-location of the DEP propellers and nacelles centre of gravity acts at the leading edge of the wing and the z-location acts at 50% of the thickness of the wing.

The main landing gear (rear wheels) is not part of the wing group, as is normally the case and thus does not change with changing wing position. The main landing gear, rear wheels, position was fixed due to the packaging of the car. When the wing position will be moved, the location of the rear wheels is compared with the most aft c.g. location for that scenario, in order to make sure the aircraft wouldn't tip over.

Table 5.18: Wing group: The masses and distances used in the analysis

Component	Mass [kg]	x_d [m]	z_d [m]
<i>Wing</i>	200	3.40	1.54
<i>DEP props</i>	96	3.1	1.54
<i>Nacelles</i>	17	3.1	1.54

Table 5.19: Tail group: The masses and distances used in the analysis

Component	Mass [kg]	x_d [m]	z_d [m]
<i>Linkage</i>	18	3.85	1.295
<i>Empennage</i>	31	7.97	2.63
<i>Tail boom</i>	72	5.28	1.35

The $x_{cg, oew}$ of the full configuration in x-z coordinates (3.20;0.92) measured with respect to the reference point. The x-location is at 38% of the fuselage length and at 14% of the MAC. The total empty mass was equal to 1174.7 kg.

¹⁶<https://www.globalair.com/aircraft-for-sale/Specifications?specid=468>, (Retrieved on 20 December 2017)

¹⁷<https://www.tecnam.com/aircraft/p2006t-smp/>, (Retrieved on 20 December 2017)

Centre of gravity range during operation

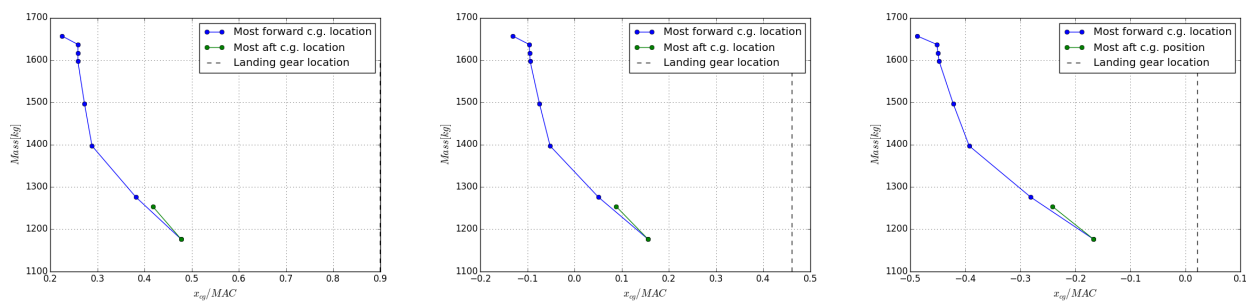
In order to identify the most forward and most aft c.g. range during operation, the most critical cases had to be identified. In order to minimise this c.g. range and hence arrive at a smaller tail size, certain operational limitations were put into place. These are listed below:

- If the pilot flies alone, luggage should be placed in the 'aft' located luggage compartment or on the seats.
- If the pilot flies with one passenger, luggage should be placed in the 'aft' located luggage compartment or on the remaining seat.

The most critical forward c.g. location occurs when the pilot is flying with a full fuel tank and with 2 passengers, who all bring luggage. Then one piece of luggage has to be placed in the forward compartment. For this critical case it was also assumed that pilot and passengers would weigh 100 kg, which is heavier than the standard mean value of an adult of 77.4 kg Berdowski et al. (2009), as this would move the c.g. more forward.

The most critical aft c.g. location occurs when the pilot is flying alone without fuel, as all the other parameters such as luggage and passengers would move the c.g. of the aircraft forward. For this critical case it was assumed that the pilot weighs the standard mean value of an adult of 77.4 kg Berdowski et al. (2009), as a heavier pilot would move the c.g. more forward.

These critical cases are plotted for three different wing locations, the initial estimate of XLEMAC = 3.1 m \pm 10%. This changed the $x_{cg,OEW}$, which in turn influenced the most forward and most aft c.g. location during operation. This is shown in figs. 5.16a to 5.16c



(a) The c.g. range for XLEMAC = 2.79 m

(b) The c.g. range for XLEMAC = 3.1 m

(c) The c.g. range for XLEMAC = 3.41 m

The c.g. range at the initial wing location is equal to 15.5 cm, which is 22% of the mean aerodynamic chord. In Roskam (1997b) it is stated that for twin engine aircraft the c.g. range is between 12 and 22% of the chord. Therefore, the obtained c.g. range was deemed reasonable.

From figs. 5.16a to 5.16c, The most forward and most aft c.g. location for each wing location was taken and a safety margin of 5% was added. This results in fig. 5.17, where the wing location is plotted with respect to the centre of gravity location as percent of mean aerodynamic chord (MAC). This plot is used in determining the minimum required horizontal tail size.

In order to determine the vertical (z -direction) c.g. range, the most critical cases were identified. The highest z_{cg} occurs when just the pilot is present in the vehicle as passengers, luggage and fuel would move the c.g. downward. This gives a z_{cg} of 0.86 m with respect to the ground. Deducting the ground clearance of 17 cm, the z_{cg} acts at 53% of the fuselage height. The lowest z_{cg} occurs when the aircraft is fully loaded. This gives a z_{cg} of 0.76 m with respect to the ground. Deducting the ground clearance of 17 cm, the z_{cg} acts at 45% of the fuselage height.

Tip-over stability

The most critical case occurs when just the pilot is in the vehicle, since other passengers, fuel and luggage would move the z_{cg} downwards, which would positively decrease the arm with respect to the rear wheels. This is at $z_{cg} = 0.76$ and $x_{cg} = 3.16$ m. The analysis was performed at the moment the vehicle would accelerate from a stationary position, hence the effect of lift, drag of the vehicle and thrust of the engines was neglected. The same free body diagram as for the road configuration was used, fig. 5.15. The main landing gear (rear wheels), x_{mg} , is at 3.425 m, the front gear (front wheels), x_{fg} is at 0.625 m. The friction coefficient, μ , is set to 0.02 as it is assumed that the vehicle is driving on asphalt

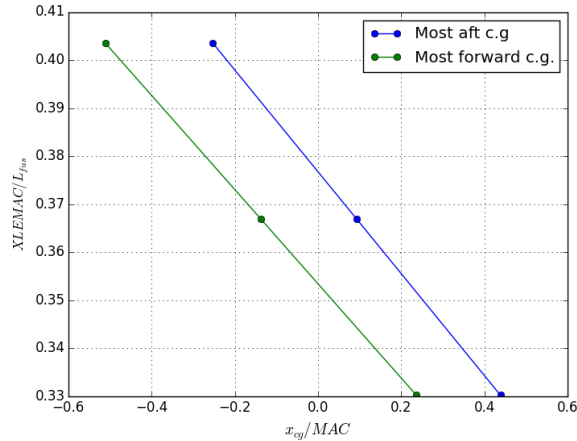


Figure 5.17: The wing location (XLEMAC) as a function of the length of the fuselage (L_{fus}) plotted with respect to the x_{cg}/MAC for three different wing locations, XLEMAC = 2.79 m, 3.1 m and 3.41m

(Roskam, 1997c). The weight of the vehicle in this case is 1251 kg.

Based on this analysis the maximum thrust the wheels can generate is 3000N. Which means that in flight configuration a limit on the thrust generated by the wheels should be put in place. This can be incorporated in the system's specifications which would automatically apply this when it recognises that the flight hardware is attached.

5.3.4. Longitudinal Stability and Control

This section will discuss the longitudinal stability and control analysis performed to arrive at the required horizontal tail size. First the equations of motion used will be presented, after which the different cases which were taken into account are explained.

Equations of motion

The equations of motion were derived using fig. 5.18.

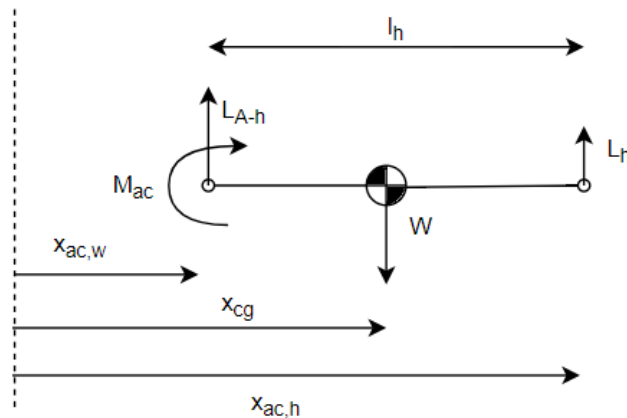


Figure 5.18: The free body diagram used in the longitudinal stability and control analysis

The assumptions made are listed below:

- In this analysis the effect of thrust and drag was not taken into account and only the weight and lift forces are analysed. Thus the equilibrium was calculated along the horizontal, no vertical displacement was taken into account. Even though the thrust location is known, it is decided not to take this into account as the exact location where the drag acts is not known. If only the thrust was taken into account a more inaccurate result would occur since the drag would counter the moment created by the thrust to some extent
- The moment was taken around the centre of gravity

- It was assumed that the distance from the centre of gravity to the aerodynamic centre of the tail is more or less equal to the tail arm.

Stability

Equation (5.41) was used to determine the horizontal tail size as a function of the centre of gravity. The stability of the aircraft was assessed at cruise speed. The location of the aerodynamic centre is influenced by the wing, fuselage and nacelles. The aerodynamic centre of the wing was taken to be at 25% of the mean aerodynamic chord which is a valid assumption for a high aspect ratio wing at subsonic speeds (Raymer, 1999). The contributions of the fuselage and nacelles was calculated using the equations presented in appendix E of Torenbeek (1982). The aerodynamic centre of the wing and fuselage was calculated using eq. (5.38). In this equation, c_g is the geometric chord and is determined by dividing the surface area of the wing by the span. The variables used are defined in fig. 5.19.

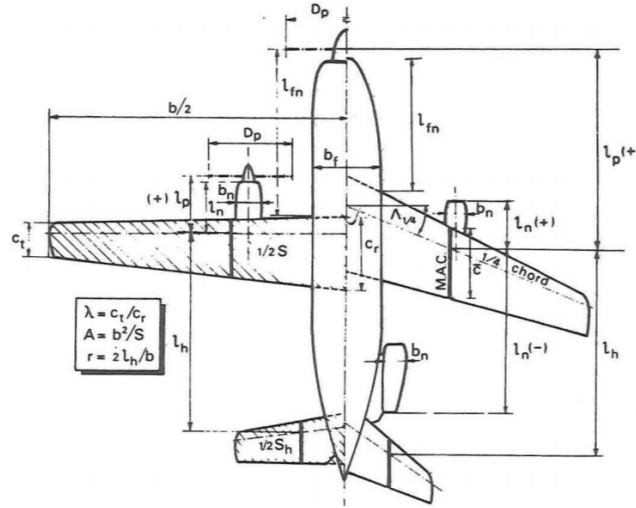


Figure 5.19: Showing how the variables used in the equations are defined (Torenbeek, 1982)

$$\left(\frac{x_{ac}}{c}\right)_{wf} = \left(\frac{x_{ac}}{c}\right)_w - \frac{1.8}{(C_{L\alpha_{wf}})} \frac{b_f h_f l_{fn}}{Sc} + \frac{0.273}{1 + \lambda} \frac{b_f c_g (b - b_f)}{c^2 (b + 2.15 b_f)} \cdot \tan \Lambda_{0.25c} \quad (5.38)$$

The DEP propellers were modelled as nacelles and the contribution to the aerodynamic centre was calculated with eq. (5.39). Where k_n is equal to -4.0 for nacelles mounted in the front of the LE of the wing and b_n and l_n are the width and length of the nacelles, these were provided by Flight performance. (Torenbeek, 1982).

$$\Delta \frac{x_{ac}}{c} = \sum k_n \frac{b_n^2 l_n}{Sc(C_{L\alpha_{wf}})} \quad (5.39)$$

This resulted in the aerodynamic centre of the aircraft less tail $\left(\frac{x_{ac}}{c}\right) = -0.094$. This means that the aerodynamic centre of the wing, fuselage and nacelles is in front of the wing. The downwash of the wing was modelled using the equation derived in Slingerland (2005), resulting in a downwash gradient of 0.17. Furthermore, using the equation on page 317 in Torenbeek (1982), the extra downwash gradient due to propellers was taken into account. This was necessary as the tail is within the region of influence. This resulted in a total downwash gradient of 0.18.

The commonly used NACA0012 airfoil was selected for the horizontal tailplane and the $C_{L\alpha_h}$ for an aspect ratio of 5 was found to be equal to 4.38^{-1} . Equation (5.40) was used to calculate $C_{L\alpha_{A-h}}$ and was taken from Torenbeek (1982), this equation is valid for near-circular cross-section with $\frac{b_f}{b} < 0.2$. The ratio of the vehicle is equal to 0.15, therefore the equation was used. S_{net} was calculated by using the width of the fuselage where the wing acts (1.85 m) and the root chord (0.782 m). This resulted in $C_{L\alpha_{A-h}}$ being equal to 6.49 rad^{-1} .

$$C_{L\alpha_{A-h}} = C_{L\alpha_w} \left(1 + 2.15 \left(\frac{b_f}{b}\right)\right) \left(\frac{S_{net}}{S}\right) + \frac{\pi}{2} \frac{b_f^2}{S} \quad (5.40)$$

As was mentioned before a T-tail configuration is used, this results in $(\frac{V_h}{V})^2 = 1$ (LaRocca, 2017a). The tail arm (l_h) was found to be equal to 4.9 m, which is 58% percent of the total fuselage length. In Raymer (1999) a value of 50-55 % is mentioned for wing mounted engines aircraft. The stability margin, the distance between the centre of gravity and the aerodynamic centre was set at 10% of the MAC. The result is plotted as a line in fig. 5.21.

$$\frac{S_h}{S} = \frac{\bar{x}_{cg}}{\frac{C_{L,\alpha_h}}{C_{L,\alpha_{A-h}}} (1 - \frac{d\epsilon}{d\alpha}) \frac{l_h}{\bar{c}} (\frac{V_h}{V})^2} - \frac{\bar{x}_{ac} - s.m.}{\frac{C_{L,\alpha_h}}{C_{L,\alpha_{A-h}}} (1 - \frac{d\epsilon}{d\alpha}) \frac{l_h}{\bar{c}} (\frac{V_h}{V})^2} \quad (5.41)$$

Controllability

Equation (5.43) was used to determine the required horizontal tail size as a function of the centre of gravity position \bar{x}_{cg} . The controllability of the aircraft is assessed at the stall speed that would occur during landing, as the aircraft still needs to be controllable in that case. This is the scenario with the highest C_L and the flaps at their maximum position. Assuming that the lift coefficient of the aircraft less tail is equal to the lift coefficient of the wing, $C_{L,A-h} = 3.98$. The aerodynamic moment of the flapped wing was provided by aerodynamics, $C_{m,ac,w} = -0.805$. The contribution of the fuselage and nacelles was calculated using equations present in appendix E of Torenbeek (1982), (LaRocca, 2017b). This equation is shown in eq. (5.42), where C_{L_0} is the lift coefficient of the flapped wing at zero angle of attack. This resulted in a total $C_{m,ac} = -1.86$.

$$(C_{mac})_{wf} = C_{mac,w} - 1.8 \left(1 - \frac{2.5b_f}{l_f} \right) \cdot \frac{\pi b_f h_f l_f}{4Sc} \cdot \frac{C_{L_0}}{C_{L_{\alpha_{wf}}}} \quad (5.42)$$

$$\frac{S_h}{S} = \frac{\bar{x}_{cg}}{\frac{C_{L,h}}{C_{L,A-h}} (\frac{V_h}{V})^2 \frac{l_h}{\bar{c}}} - \frac{\frac{C_{m,ac}}{C_{L,A-h}} + \bar{x}_{ac}}{\frac{C_{L,h}}{C_{L,A-h}} (\frac{V_h}{V})^2 \frac{l_h}{\bar{c}}} \quad (5.43)$$

From eq. (5.43) it becomes clear that in order to decrease the slope of the curve and hence allow for a more forward c.g. location during operations, the denominator should be as large as possible. Compared to regular general aviation aircraft, the $C_{L,A-h}$ is much higher due to the use of DEP. In order to be able to achieve an acceptable tail size, $C_{L,h}$ should be as high as possible, which resulted in employing a fully movable tail, also known as a stabilator. This would allow the CL_h in landing configuration to be -1.0 (LaRocca, 2017b). A stabilator is mostly found on military aircraft, however it is not uncommon for general aviation aircraft, the PA-44-180T, Cessna 177 and Piper Cherokee among others have a fully movable tail.¹⁸ In order to make sure that the pilot knows he is rotating the tail plane, the pilot's input should be resisted. An anti-servo tab which moves in the same direction as the stabilator provides this resistance. However this anti-servo tab is not analysed further. The result of the controllability analysis is plotted as a line in fig. 5.21.

As was mentioned in section 5.1 the angle of attack of the aircraft during landing stall speed is 10.6 degrees. The height of the car at it's end is 0.41 m with respect to the ground. The distance from the rear wheels contact point with the ground to the back of the car is 1.075 m. This results in an angle of 21 degrees. Furthermore, the angle of the tail boom extending from the back of the car to the end of the fuselage is 15 degrees. This is visualised in the rendering of the final design shown in section 5.6. Therefore, it is concluded that in this worst case landing scenario the tail will not touch the ground.

Take-off rotation

The horizontal tail should be able to provide a large enough force that allows the aircraft to rotate the nose during take-off. In this analysis the effect of thrust and drag are incorporated and the moment is taken around the rear wheels (main landing gear). The worst case was analysed which occurs at the most forward centre of gravity location, as this increases the moment arm of the weight, $x_{cg} = 3.0$ m and $z_{cg} = 0.77$. In order to have some controllability left at rotation, the moments are not set equal to zero but equal to $I_{yy_{mg}} \ddot{\theta}$. In Roskam (1997c) a design value of $\ddot{\theta}$ for light aircraft was taken, $\ddot{\theta} = 10 \text{deg/s}^2$. The moment of inertia around the y-axis, I_{yy} was found using a class II method, eq. (5.44) and was equal to 2463 kg·m². Comparing this with a rough class I method shown in eq. (5.45) where a reference value for the radius of gyration ($R_y = 0.33$) was taken from Roskam (2003) for reference aircraft, resulted in a $I_{yy,ref} = 3218 \text{kg} \cdot \text{m}^2$. The value that resulted from the class II method is in the same order of magnitude, however it deviates by a few hundred. This can be explained because a lot of the heavy equipment, such as the engine and generator are close to the x_{cg} and z_{cg} , which decreases their effect. In conventional single engine aircraft the engine is

¹⁸<http://janes.ihs.com>, (Retrieved on January 19 2018)

in the front, which has a larger arm with respect to x_{cg} , which increases the moment of inertia. In conventional twin engine aircraft the engines are located at the propellers on the wing, which also increases the arm with respect to x_{cg}

$$I_{yy} = \sum_{i=1}^{i=n} m_i \{(z_i - z_{cg})^2 + (x_i - x_{cg})^2\} \quad (5.44)$$

$$I_{yy,ref} = \frac{L_{fus}^2 (W/g) R_y^2}{4} \quad (5.45)$$

The moment of inertia of the aircraft around the y-axis, I_{yy} , was needed to calculate the pitching moment of inertia about the main gear contact point, eq. (5.46). (Roskam, 1997c)

$$I_{yy,mg} = I_{yy} + \frac{W}{g} \{z_{mg}^2 + (x_{mg} - x_{cg})^2\} \quad (5.46)$$

The assumptions used for this analysis are presented below.

- The analysis is performed at the moment the aircraft would start to rotate, therefore the force that acts on the front wheels is assumed to be equal to zero.
- It is assumed that the drag force acts at the centre of gravity in this case.

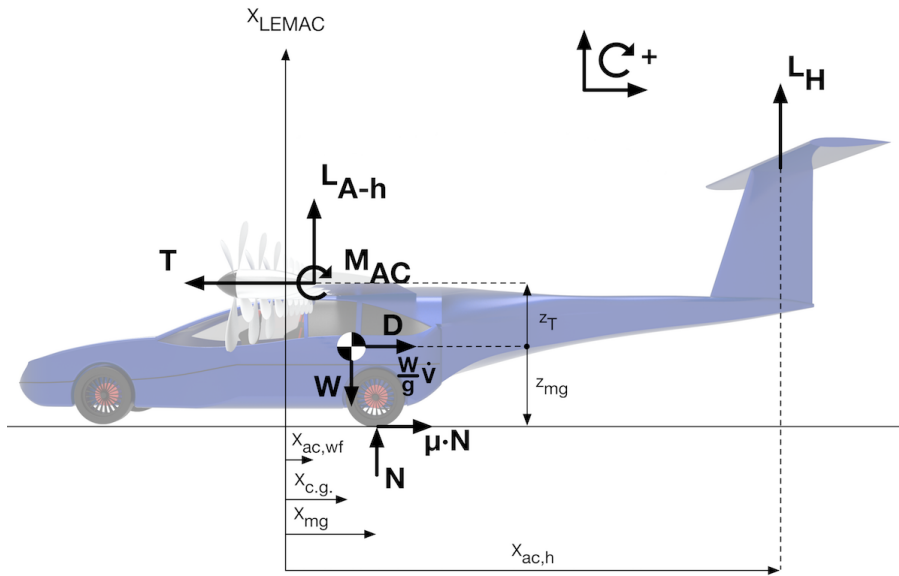


Figure 5.20: The diagram used for the take-off rotation analysis

This analysis was based on the analysis performed in Roskam (1997c), the equation is rewritten into the form shown in eq. (5.47), the resulting line is plotted in fig. 5.21.

$$\frac{S_h}{S} = \frac{C_{m,ac,to} - \frac{T_{to}(z_{mg} + z_T) - W(x_{mg} - x_{cg}) - (I_{yy,mg}\ddot{\theta})}{q_{to}S\bar{c}} + C_{L_{A-h,to}} \frac{x_{mg} - x_{ac}}{\bar{c}} + C_D \frac{z_{mg}}{\bar{c}} + \left[\frac{T_{to} - \mu W}{q_{to}S} - C_D - C_{L_{A-h,to}} \right] \left(\frac{z_{mg}}{\bar{c}} \right)}{C_{L,h} \left(\frac{V_h}{V} \right)^2 \frac{(x_{ach} - x_{mg})}{c}} \quad (5.47)$$

The $C_{m,ac,w}$ of the wing was provided by aerodynamics and equal to -0.7688. The contribution of the fuselage and nacelles was calculated using equation, eq. (5.42), present in appendix E of Torenbeek (1982). This resulted in the total aerodynamic moment of $C_{m,ac} = -1.37$. The $C_{L_{A-h}}$ at rotation speed was equal to 2.37, the C_D followed from aerodynamics and was equal to 0.253. The thrust at take-off was equal to 3200 N. Furthermore, $z_{mg} = 0.45$ m, $z_T = 0.76$ m, $x_{mg} = 0.325$ m, $x_{ach} = 4.84$ m. The horizontal tail lift coefficient, $C_{L,h} = -1$, as explained in Controllability.

As was mentioned in section 5.1 the angle of attack of the aircraft at lift-off is 6 degrees. The height of the car at its end is 0.41 m with respect to the ground. The distance from the rear wheels contact point with the ground to the back of

the car is 1.075 m. This results in an angle of 21 degrees. Furthermore, the angle of the tail boom extending from the back of the car to the end of the fuselage is 15 degrees. This is visualised in the rendering of the final design shown in section 5.6. Therefore, it is concluded that during take-off the tail will not touch the ground.

Horizontal tail size

The scissor plot, fig. 5.21 graphically plots all of these lines into one figure, that has the horizontal tail size fraction $\frac{S_h}{S}$ on the y-axis and the x_{cg}/MAC plotted on the x-axis.

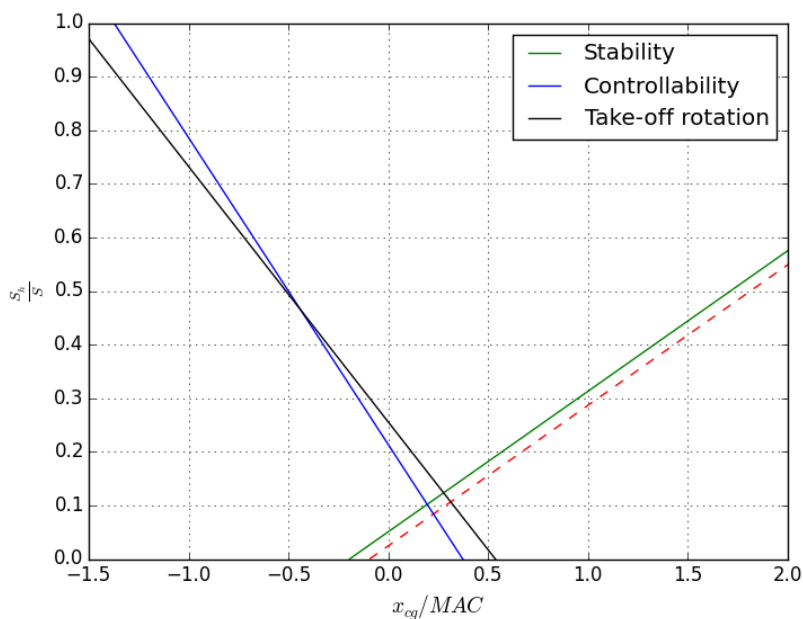


Figure 5.21: The scissor plot showing the Controllability, Stability and Take-off rotation line.

The scissor plot, fig. 5.21 and the c.g. range for different wing locations, fig. 5.17, are used together to determine the minimum required tail size at the most optimal/feasible wing location. As can be seen from fig. 5.21 the take-off rotation will determine the sizing of the tail. The $\frac{S_h}{S}$ resulting from combining the two diagrams was equal to 0.25 at a wing location (XLEMAC) equal to 2.97 m with respect to the nose. Because a T-tail was selected, a factor of 15% was added to the $\frac{S_h}{S}$ ratio to account for deep stall, this resulted in a value value of 0.2875. The horizontal tail surface is then equal to 2.42 m² at a wing location of 2.97 m. Based on this surface, the span and chord was calculated. An aspect ratio of 5 was chosen for the horizontal tail based on reference aircraft found in (Roskam, 1997b), furthermore, no sweep was selected and therefore the taper ratio was set to one. This eases fabrication and hence saves costs. This resulted in a span of 3.48 m and a chord of 0.695 m. These values were then used to perform the second iteration to see if changing the wing location (XLEMAC) in the scripts and consequently changing the tail arm (l_h) and other parameters would influence the obtained $\frac{S_h}{S}$ value. Moreover, the c.g. of the full configuration was updated and consequently also the c.g. range during operation. Combining the new scissor plot with the new c.g. range plot showed that at the wing location (XLEMAC) of 2.97 m, the $\frac{S_h}{S}$ was again equal to 0.25, and to 0.2875 after adding the 15% increase for T-tail. It was not analysed whether a smaller surface could be obtained by moving the wing further forward as then problems arise in the linkage of the flight hardware to the road hardware. Therefore, it was concluded that the final value of the horizontal tail surface was equal to 2.42 m² at a wing location of 2.97 m with respect to nose. The resulting tail size was compared to another fully movable tail aircraft, with similar characteristics, PA-44-180T Seminole which has a $S_h = 2.27$ m². Therefore, the obtained value was deemed reasonable. The updated values for the c.g. of the operative empty weight and during operations are shown in table 5.20.

Discussion of results

The equations used were verified by re-calculating them by hand. Furthermore, the obtained values were compared to data from reference aircraft as much as possible. Moreover, sanity checks on the order of magnitude were performed.

Table 5.20: Showing the centre of gravity corresponding to the initial wing location and the final wing location.

	First iteration (XLEMAC = 3.1 m)	Second iteration (XLEMAC = 2.97 m)
$x_{cg,oew}$	3.20 m (37.8% of fuselage length)	3.16 m (37.4% of fuselage length)
$z_{cg,oew}$	0.91 m	0.91 m
Most forward c.g. during operation	2.99 m	2.97 m
Most aft c.g. during operation	3.15 m	3.12 m

The obtained horizontal tail surface was deemed reasonable, however, as distributed electrical propulsion is a new propulsion method, the semi-empirical relations used throughout the analysis might not be able to correctly model the stability of the aircraft. The aspect ratio of 17 combined with the small surface area of 8.42 m² due to DEP might not be within the range of these semi-empirical relations. Moreover, the horizontal tail values obtained could not be validated with the analysis on DEP NASA performed in their Leapttech articles (Stoll et al., 2015), (Stoll et al., 2014), as the tail was left out of the analysis. The recommendations for further research can be found in chapter 13.

5.3.5. Directional and Lateral Stability and Control

The directional and lateral stability of the aircraft depends on the size and shape of the wing, fuselage, horizontal stabiliser and vertical stabiliser. The planform of the wing was determined in section 5.2.1. The size and shape of the fuselage was decided in section 5.3.1 and the planform of the horizontal stabiliser was concluded in section 5.3.4.

This subsection will start by validating an initial estimate for the planform of the vertical tail. Next, the equilibrium equations derived from the asymmetric equations of motion will be discussed for the most critical control situations. To satisfy these equilibrium equations, the stability and control derivatives will be calculated using the estimated planform of the vertical stabiliser. The sign of the derivatives will be checked to prove static stability of the aircraft. Using an iterative process the planform of the vertical stabiliser will be optimised for size.

Planform of the Vertical Stabiliser, Rudder and Ailerons

An initial estimate for the surface area of the vertical stabiliser can be calculated using eq. (5.48) from Torenbeek (1982). To validate this initial estimate, it is compared to the surface area of vertical tails of reference aircraft presented in Roskam (1997b). The reference surfaces are in general twice the surface of the initial estimate. Since the surface areas of the wings of these reference aircraft are twice the surface area of the wing of the vehicle, this deviation is as expected.

$$S_v = 0.05 \cdot \frac{S \cdot b}{l_v} \quad (5.48)$$

Where, l_v is the distance between the centre of gravity and the aerodynamic centre. As a first estimate this can be set to 50% (Torenbeek, 1982) of the fuselage length. This value was validated by reference aircraft in Roskam (1997b) and by comparing the result with the distance between the centre of gravity locations determined in section 5.3.1 and the fuselage length.

Next, the airfoil has to be chosen. At this stage of the analysis the airfoil will not be optimised. As a NACA0012 airfoil is a standard airfoil for vertical stabilisers, this airfoil will be used to determine the stability, and control derivatives.

The vertical stabiliser in a T-tail configuration has the advantage that it stays out of the prop wash and wing wake, which increases its effectiveness. Additionally, the horizontal stabiliser will function as an endplate for the vertical stabiliser, which increases its effectiveness even more. Hence, a reduction in size could be anticipated from a stability and control point of view. However, the vertical stabiliser needs to carry the loads of the horizontal stabiliser. Therefore, the minimum length of the tip chord of the vertical stabiliser needs to be restricted to at least 90% of the root chord of the horizontal stabiliser. (Hetteema, 2015) As a starting point, the tip chord of the vertical stabiliser is set equal to the chord of the horizontal stabiliser.

Another structural restriction is the ratio of the span over the fuselage depth near the tail. A ratio higher than 7 should be avoided. (Roskam, 2000b) Since the boom, connecting the the car and the empennage, is modelled as a right angled rectangle, the fuselage depth near the tail can be found using similar triangles. It appears that the fuselage depth near the tail is relatively small. Therefore, the span should be restrained. Moreover, to provide a sufficient thickness division along the span the maximum taper ratio is 0.6. (Hetteema, 2015, Roskam, 1997b) In order to restrain the span, the taper ratio will be set to 0.6 as an initial estimate.

The surface of the rudder and ailerons can be approximated by the surface of the vertical tail and wing respectively. The rudder's surface is on average 45% of the vertical tail's surface and the ailerons' surface is on average 6.5% of the

wing's surface. (Torenbeek, 1982) Due to possible structural difficulties of mounting a full movable horizontal stabiliser on top of the vertical stabiliser, it is assumed that only 90% of the span of the vertical stabiliser can be used as rudder. Additionally, no aft sweep is assumed to obtain maximum rudder effectiveness.

Finally, using the estimated surface area, tip chord and taper ratio, the mean aerodynamic chord, span, aspect ratio and sweep at the leading edge, quarter chord point and half chord point can be calculated by substituting the relevant parameters of the vertical tail in eq. (5.2), eq. (5.6) and eq. (5.7). It should be noted that these equations are set up for wing parameters. The span of a wing is defined from tip to tip, while the span of a vertical tail is defined from tip to root chord. Therefore, the span and aspect ratio of the vertical tail should be multiplied by two before substitution.

Asymmetric Equations of Motion in Critical Control Situations

The vertical tail will influence the aircraft's response to small perturbations. Certain responses are required or desirable for stability and good control characteristics. Furthermore, the control surfaces have to be big enough to provide sufficient control over the aircraft in normal and abnormal flight. The surface of the vertical tail will be reduced until one of the stability derivatives will become unstable or until the rudder size will become insufficient. The two situations for which the rudder's effectiveness will be tested are take-off with one engine inoperative and landing with crosswind. The equilibrium equations describing the aircraft in these situations can be derived from the aircraft's equations of motion in steady asymmetric flight presented in Mulder et al. (2013). The assumptions made in Mulder et al. (2013) to linearize the equations of motion will also apply to the derived systems in steady flight. Yawing moment due to aileron deflection and rolling moment due to rudder deflection are assumed negligible. The systems presented in eq. (5.49) and eq. (5.50) are the systems used to determine the rudder size in a climb on take-off with one engine inoperative and in a cross wind landing respectively. In these systems ϕ , β , δ_a and δ_r represent the aircraft's bank angle, angle of sideslip, aileron deflection and rudder deflection respectively. The derivatives with respect to sideslip, $C_{Y\beta}$, $C_{l\beta}$ and $C_{n\beta}$, represent the non dimensional yawing force, rolling moment and yawing moment respectively. $C_{l\delta_a}$ and $C_{n\delta_r}$ represent the rolling moment due to aileron deflection and yawing moment due to rudder deflection respectively. Additionally, due to the expected high rudder deflection, the lateral force $C_{y\delta_r}$ cannot be neglected. (Mulder et al., 2013)

Critical engine off in take-off

Failure of the critical engine will result in a large yawing moment, C_{n_e} , due to both loss of thrust and an increase in drag. Due to the loss of thrust, lift over the wing with the inoperative engine will decrease. This will cause the aircraft to roll towards the dead engine. Maximum aileron deflection should be sufficient to maintain wings level. However, this rolling moment will be neglected for now. If the aileron size appears to be a critical factor, it can be taken into account at a later stage. The propellers on the vehicle are counter rotating outward. Therefore, the critical engine is either one of the most outboard engines. The lateral force created by the torque will create an extra yawing moment towards the dead engine when the centre of gravity is in front of the leading edge. However, an aft centre of gravity is assumed to be more critical due to the reduced tail arm of the rudder. To be on the conservative side, the torque reducing the yawing moment in this situation is neglected. Investigating the different flight phases on speed, thrust setting, flap setting and number of engines operating, it was determined that a critical engine failure on take-off will cause the largest yawing moment. Steady straight flight in this situation can be achieved using a combination of roll and yaw. (Hetteema, 2015) Aileron and rudder deflection are both restricted to a maximum of 25 degrees of deflection. Since the aircraft does not have to change the power setting to remain the required climb rate, the yawing moment due to the failed engine is calculated using take-off thrust rather than full thrust. This moment together with the yawing moment due to sideslip need to be complemented by a yawing moment created by deflection of the rudder. Maintaining wings level, $\phi=0$, results in the largest sideslip angle. Hence, this results in the largest yawing moment for the rudder to overcome. For an acceptable sideslip angle of 5 degrees and zero bank, the system will be evaluated. The vertical stabiliser should be just large enough to allow a rudder size that can counter the yawing moment, while the stability derivatives remain acceptable. Furthermore, it will be checked that the maximum rudder deflection and aileron deflection provide enough lateral force and rolling moment respectively to equal the lateral force and rolling moment due to sideslip. Finally, the situation of a forward centre of gravity taking the extra moment due to torque into account will be checked.

$$\begin{bmatrix} C_{Y\beta} & 0 & C_{y\delta_r} \\ C_{l\beta} & C_{l\delta_a} & 0 \\ C_{n\beta} & 0 & C_{n\delta_r} \end{bmatrix} \begin{bmatrix} \beta \\ \delta_a \\ \delta_r \end{bmatrix} = - \begin{bmatrix} 0 \\ 0 \\ C_{n_e} \end{bmatrix} \quad (5.49)$$

Crosswind landing

According to regulation (23.75) the aircraft must still be fully controllable enduring a crosswind on landing of 20% of its take-off speed. The equilibrium equations corresponding to a landing with crosswind in landing configuration are presented in eq. (5.50). To be on the conservative side it is assumed that the aircraft is flying at touchdown speed, as this is the lowest speed encountered on approach. From Pythagoras's theorem it can be calculated that this results in an angle of sideslip of 12.8 degrees. For validation this is compared to the translated angle of sideslip presented in literature of 11.5 degrees. (Raymer, 1999, Torenbeek, 1982) This angle is lower, because it is calculated for an aircraft flying at approach speed rather than touchdown speed.

To satisfy the equilibrium equations in eq. (5.50), a bank angle of five degrees is assumed acceptable. (Torenbeek, 1982) However, the propeller tip of the most outboard propeller on the downward wing will touch the ground on touchdown for a bank of more than 4.9 degrees. Therefore, the bank angle on approach is limited to three degrees.

$$\begin{bmatrix} \frac{mg}{Sq} & C_{Y\beta} & 0 & C_{y\delta_r} \\ 0 & C_{l\beta} & C_{l\delta_a} & 0 \\ 0 & C_{n\beta} & 0 & C_{n\delta_r} \end{bmatrix} \begin{bmatrix} \sin(\phi) \\ \beta \\ \delta_a \\ \delta_r \end{bmatrix} = \begin{bmatrix} 0 \\ 0 \\ 0 \end{bmatrix} \quad (5.50)$$

Stability and Control Derivatives

For stability of the aircraft certain sign conventions of the stability derivatives are desirable. In general it is required that the aircraft reacts in a statically stable convention to a small perturbation. Therefore, the natural reaction of the aircraft to a positive angle of sideslip should be to decrease this angle. This translates to a positive yawing moment and a negative lateral force due to a negative angle of sideslip. Hence, $C_{n\beta}$ should be positive and $C_{Y\beta}$ should be negative. An aircraft subject to a perturbation causing positive roll, experiences a positive angle of sideslip due to the lateral force caused by gravity. In order for the aircraft to be statically stable, the aircraft should react to this positive angle of sideslip by rolling in the negative direction. Therefore, the sign of $C_{l\beta}$ should be negative.

The main contribution to the value of $C_{Y\beta}$ is the size of the surface and the lifting capability of the vertical tail. Due to the horizontal stabiliser increasing the aspect ratio of the vertical stabiliser (Roskam, 2000b), $C_{Y\beta}$ has a relative high absolute value. For the calculation of $C_{Y\beta}$ the contribution of the wing and fuselage have been neglected for simplicity. This is on the conservative side from a stability point of view, because the contributions of the wing and fuselage would make the derivative even more negative.

Next, $C_{l\beta}$ will be calculated. Since the vehicle has no dihedral and almost no sweep, it will get its main contribution from the wing fuselage interaction. A lower lift coefficient of the main wing and lower speed negatively influence its value.

The aircraft's directional stability, $C_{n\beta}$, has a negative contribution from the fuselage. It gets its desired positive value from the planform of the vertical tail and the vertical tail's distance to the centre of gravity.

The vertical tail will provide longitudinal and directional trim, while the wing will provide lateral trim. The aircraft's lateral control characteristic is influenced by the planform of the vertical stabiliser. Therefore, the size of the ailerons will be determined alongside the calculations on the size of the rudder. From the span and location of the flaps, the span and location of the ailerons were determined. As initial estimate it is assumed that the span of the aileron runs from the flap end to the tip of the wing.

The side force due to rudder deflection depends mostly on the lifting capability of the vertical tail and its surface with respect to the wing's surface. The yawing moment due to rudder will become higher for a higher absolute value of $C_{Y\beta}$.

Discussion of the Results

The final most optimal planform for the vertical stabiliser is presented in table 5.21. The results are as expected and are validated using reference data. Due to the structural limitations of taper ratio and span, the sweep angle is relatively low. This reduces the lift coefficient of the vertical tail, which will reduce the absolute value of $C_{Y\beta}$ and $C_{Y\delta_r}$. The stability derivatives can be found in table 5.22. As expected, the absolute value of $C_{Y\beta}$ is relatively low. This can also be ascribed to the neglected wing and fuselage contribution. However, the value of $C_{Y\delta_r}$ is relatively high. This is due to the fact that full rudder deflection is assumed in an engine off on take off or crosswind landing situation. Assuming no rudder deflection results in a $C_{Y\delta_r}$ of 0.149, which is really close to the reference aircraft's value.

The situation which appeared limiting is the one engine off situation, where the rudder cannot overcome the lateral force due to sideslip anymore. The lateral force due to sideslip is already relatively small. Neglecting this failure the next limiting factor becomes the yawing moment in this situation. The yawing moment due to sideslip depends mostly on the absolute value of the lateral force due to sideslip. Again, this value is already relatively low. Therefore, it is believed that optimising the vertical stabiliser can best be done by increasing the rudder's effectiveness. It is recommended to find out whether the rudder's surface could be increased.

Table 5.21: Planform of the Vertical Stabiliser

Planform Parameter	Value	Reference Roskam (2000b)	Initial Value
S_v	1.1 m ²	-	1.1 m ²
λ_v	0.6	.6-1.0	0.6
A_v	1.3	0.7-1.8	-
MAC_v	0.935 m	-	-
b_v	1.2 m	-	-
$\Lambda_{c/4}$	16 degrees	18-45 degrees	-
b_{rudder}	0.98 m	-	-
c_{rudder}	0.46 m	-	-
$b_{aileron}$	1.98 m	-	1.98
$c_{aileron}$	0.27 m	-	0.27 m

Table 5.22: Lateral-Directional Derivatives

Lateral-Directional Derivatives	N-1	Crosswind	Reference Roskam (2000b)
$C_{Y\beta}$	-0.33	-0.33	-0.59
$C_{l\beta}$	-0.088	-0.079	-0.13
$C_{n\beta}$	0.0969	0.093	0.080
$C_{Y\delta_r}$	0.223	0.225	0.144
$C_{n\delta_r}$	-0.089	-0.086	-0.0758
$C_{l\delta_a}$	0.29	0.29	0.156

Moreover, it is recommended to research how the controls will be effected by deflection of the wings in flight. Also, the increase in yawing moment due to outward turning propellers and a hing wing configuration in case of an engine failure should be calculated. (Mulder et al., 2013) If the deflection of the wing can be assumed as dihedral, it will effect the stability derivatives as well. In specific the rolling moment due to sideslip will become more negative. From a stability point of view this will not be critical as this derivative can be influenced by adding anhedral.

Furthermore, an increase in dynamic pressure in the slipstream might change the sign of the rolling moment due to sideslip derivative, resulting in an unstable aircraft. (Mulder et al., 2013) The directional and lateral stability derivatives were calculated using an estimated sidewash. This sidewash was determined using the methods in Roskam (2000b). As these equations are based on reference aircraft having in general a different fuselage shape, a lower aspect ratio wing and less propellers, it is recommended to test the wing-fuselage interference and the slip stream interference in a windtunnel.

According to regulations the minimum controllability in a steady heading sideslip with one engine inoperative needs to be sufficiently high. (Koolstra, 2017) Therefore, the situation on take-off was evaluated for the minimum control speed of 35m/s as well. It appeared that full controllability was still possible in this situation. Since this speed is only 1.5 m/s slower than the speed on take-off, this is as expected.

Moreover, a critical engine failure for the most forward centre of gravity where a lateral force due to torque results in an undesirable yawing moment, is checked. As expected, the rudder will be able to overcome the lateral force and yawing moment in this situation as well.

For the aircraft to be dynamically stable, eq. (5.51) should be satisfied. Where, C_{n_r} represents the yawing moment due to yaw rate and C_{l_r} represents the rolling moment due to yaw rate. To estimate the value on the left hand side of eq. (5.51), an prediction is made to the stability derivatives C_{n_r} and C_{l_r} . In general they have a negative and positive sign respectively. The relatively high aspect ratio and low sweep of the wing will make C_{n_r} more negative compared to reference aircraft. On the other hand, the relatively high zero-lift drag may reduce this effect. Therefore, the yawing moment due to yaw rate is believed to be comparable to reference aircraft. Furthermore, the value of $C_{Y\beta}$ will make C_{n_r} more negative than it will make C_{l_r} more positive. The wing influence on C_{l_r} depends mainly on the lift of the

wing, which is comparable to other aircraft. As the value of C_{n_β} and C_{l_β} are comparable to reference aircraft as well, eq. (5.51) is expected to be satisfied. Hence, dynamic stability is expected.

$$C_{l_\beta} C_{n_r} - C_{n_\beta} C_{l_r} > 0 \quad (5.51)$$

Finally, to proceed the control and stability analysis the hinge moments derivatives should be calculated. Moreover, controllability in gliding flight should be checked and the stall angle of the vertical stabiliser should be calculated.

5.4. Materials and Structures

In order to have a safe flight, the structure of the vehicle cannot fail. This section will therefore analyse the major components of the aircraft and size them in such a way that the vehicle will be safe to fly. The materials used, wing, truss structure and landing gear will be discussed.

5.4.1. Materials

In order to design a structure, materials need to be selected. This is an iterative process as some loads need to be calculated in order to assign materials, whilst material properties are needed for structural calculations as well. The vehicle will consist of several different materials, which will be presented here.

First of all, several truss structures will carry the loads during flight. Aluminium and steel seem to be the best options for the truss structure as they are both commonly used and have proven to be reliable materials in the aerospace industry. Due to the fact that steel is heavier and more expensive aluminium was preferred. The aluminium that is used for the trusses is not the common AL7075-T6 but a different aluminium alloy. The trusses are to be welded together and AL7075-T6 is very prone to microcracking during the welding process. Therefore, AL5182-H19 was selected. This is also a very strong, even lighter aluminium but it has a different alloy composition which makes it weldable.

For the wing two materials can be used. One of them is AL7075-T6. The wing does not need to be welded and hence AL5182-H19 is not needed. AL7075-T6 has a higher yield strength and since the wing has to endure a high ultimate load a higher yield stress is preferable. The choice was made to make the whole wing out of one material and not just the wingbox. This is due to the fact that interaction between different materials in the wing, especially aluminium with carbon fibre reinforced plastic (CFRP), will bring a lot of extra difficulties such as galvanic corrosion and adhesive problems. Production will also be more expensive, and hence the whole wing will be made of one material. The other material which can be used for the wing is CFRP. The advantage of using CFRP is its specific stiffness. CFRP weighs significantly less than aluminium but still has the same strength and Young's modulus if you use the right laminate. CFRP is however very expensive, especially the production as it requires a high skill-level and a lot of man-hours. The choice between these materials will be made in section 5.4.2

For the skin, several materials have been evaluated. It is assumed that the skin is not carrying any loads, and hence it should not weigh too much. However, it should be able to resist at least some impact, which eliminates very brittle materials. At first several thermoplastics were evaluated, as these have good qualities when it comes to recycling. After a thorough investigation it turned out that almost all thermoplastics are either not suitable for this project or are too expensive. Materials such as PP, PET, PC, PVC and foams are not suitable because they become brittle below 0°Celsius, which is not favourable as the temperature at 10000 ft is about -4°Celsius. Materials such as PEEK, PEI and PEK are used in the aerospace industry but are very expensive, which is not favourable for a simple shell. When looking at thermosets it turned out that Polyester with glass fibres was the most favourable material, as it is light and not too expensive. This material is also used in the automotive industry for low density exterior body panels, which is exactly what it will be used for. It is compatible with a foam or balsa core if the skin needs some extra stiffness without adding a lot of mass. Since the skin is made of fibres, it will carry some of the loads in real life. This is something that has to be looked into in a future stage in the project, but for now it is assumed that 2mm of skin with a foam core of negligible mass will be used for the skin of the car and the flight hardware. All the material properties can be seen in Table 5.23. All of the properties have been obtained from the CES EduPack database¹⁹, except for the properties of the CFRP laminate, those have been provided by Dr. C. Kassapoglou.²⁰

Table 5.23: Material properties

Material		AL5182-H19	AL7075-T6	CFRP	Polyester with glass fibre
Price	USD/kg	1.95	3.92	40-80	3.58
Density	kg/m ²	2650	2800	1636	1270
Young's Modulus	GPa	72	72	73	7
Yield Strength	MPa	393	480	-	50
Tensile Strength	MPa	440	507	230	50
Compressive Strength	MPa	413	462	743	7
Shear strength	MPa	-	350	130	-
Fatigue strength @30000 cycl.	MPa	190	300	-	-
Eco cost	€/kg	2.14	2.14	2.64	1.13

¹⁹<http://www.grantadesign.com/education/edupack/edupack2017.htm>, 2017 version of database

²⁰Personal communication with Dr. C. Kassapoglou, 12 January 2018, TU Delft

5.4.2. Wing Box Structure

When analysing the structural components of the vehicle, one of the main components has to be the wing. The wing should be able to carry all the loads during flight and is not allowed to yield when it is subjected to the ultimate load. In order to analyse the wing, a few assumptions have been made in order to simplify the analysis. The following assumptions have been made:

- Plane cross-sections remain plane and normal to the longitudinal fibres of the beam after bending (Megson, 2007)
- Stresses are uniformly distributed over each surface (Megson, 2007)
- The material of the beam is assumed to be linearly elastic (Megson, 2007)
- The material of the beam is assumed to be homogeneous (Megson, 2007)
- The wing is modelled as a beam with a rectangular cross-section, which represents the wingbox in the wing
- The wing is attached to the side of the car. Therefore, it is assumed that the wing has no deformation and no slope at that point, which means it can be modelled as a cantilever beam.
- Only the vertical forces have been taken into account for the bending calculations
- Carbon fibre laminate can have every desired thickness for now, even though a laminate in production will have a certain preset thickness.

Figure 5.22 shows the free body diagram of the wing. It also shows what the cross section of the wing box will look like. As can be seen, the engines have been modelled as point loads, while the lift and weight forces have been modelled as distributed loads. The shape of the lift was approximated by using a parabolic equation and the weight load was approximated using a rectangular distribution in combination with a triangular distribution, as this resembles the shape of the wing itself. As there are many different loads, the principle of superposition will be used.

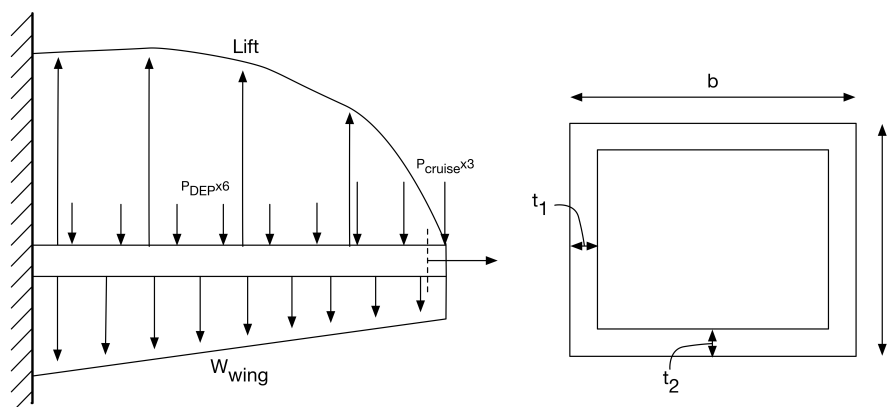


Figure 5.22: The free body diagram of the the FH structure.

In order to analyse what happens to the wing under certain loads, formulas from Megson (2007) and Hibbeler (2011) were used. The basic formulas for bending are shown in eq. (5.52).

$$v = \delta \quad \frac{dv}{dx} = \theta \quad \frac{d^2v}{dx^2} = \frac{M}{E \cdot I} \quad \frac{d^3v}{dx^3} = \frac{V}{E \cdot I} \quad (5.52)$$

First, the deflection of the beam can be calculated. All of the specific deflection formulas used for the different loads can be found in Hibbeler (2011). One must take into account that a point load which is not applied to the end of the beam causes a parabolic deflection until the point where it acts, and has a linear deflection slope after that point. Using the deflection formulas and their differentials (eq. (5.52)), the bending moment and shear force can be calculated. Once the bending moment and shear force are known, the stresses in the beam can be calculated. The stress due to the bending moment will be calculated at the point furthest from the neutral axis to obtain the maximum stress.

This stress can either be compressive or tensile depending on the load case. The stress due to the shear forces will be calculated in the middle of the vertical spars in order to see if they are thick enough. When these values have been obtained, the Von Mises yield criterion can be computed, which will show whether the beam will yield or not. Formulas for the maximum stress and the Von Mises yield criterion are shown in eq. (5.53), eq. (5.54) and eq. (5.55) and can also be found in Hibbeler (2011) and Megson (2007)

$$\sigma_x = \frac{M \cdot y}{I_{xx}} \quad (5.53)$$

$$\tau = \frac{V \cdot Q}{I_{xx} \cdot t} \quad (5.54)$$

$$\sigma_Y = \frac{1}{\sqrt{2}} \sqrt{((\sigma_{xx} - \sigma_{yy})^2 + (\sigma_{yy} - \sigma_{zz})^2 + (\sigma_{zz} - \sigma_{xx})^2 + 6\tau_{xz}^2 + 6\tau_{yz}^2 + 6\tau_{zx}^2)} \quad (5.55)$$

In order to accurately model the wing and calculate the deflections and stresses due to the different loads, a Matlab program was created. The beam was subjected to four different load cases: no external load, load during cruise, ultimate upwards load and ultimate downwards load. The weight of the beam was calculated and used for optimisation of the dimensions while still being able to endure the loads. Four different structural designs have been considered when trying to find the most optimal design for the wingbox. These four cases are:

- **Concept 1:** An aluminium beam without taper. As the wing is actually tapered the cross-section used is the average cross-section of the beam. The cross-section can fit into a NACA4412 profile, has dimensions of 0.4x0.08 m at the root and has the best performance when both t1 and t2 (Figure 5.22) equal 8 mm.
- **Concept 2:** A carbon fibre beam without taper. As the wing is actually tapered the cross-section used is the average cross-section of the beam. The cross-section can fit into a NACA4412 profile, has dimensions of 0.4x0.08 m at the root and has the best performance when both t1 equals 12 mm and t2 equals 8 mm.
- **Concept 3:** An aluminium beam with linear taper. The cross-section can fit into a NACA4418 profile, has dimensions of 0.23x0.13 m at the root and has the best performance when t1 equals 10 mm, t1_{tip} equals 8 mm, t2 equals 5 mm and t2_{tip} equals 1 mm.
- **Concept 4:** A Carbon fibre with linear taper. The cross-section can fit into a NACA4418 profile, has dimensions of 0.23x0.13 m at the root and has the best performance when t1 equals 10 mm, t1_{tip} equals 8 mm, t2 equals 8 mm and t2_{tip} equals 5 mm.

The weight of the wing is calculated using the weight of the wing box. Using the cross-sections of each case and the density of the material of each case a rough estimate of the box can be made. The structural weight is equal to 70% of the total wing weight (Ajaj, 2013). Therefore, multiplying the weight of the wingbox by 1.4, multiplying this weight by 2 for both wings and adding a penalty of 10 kg for the wing part above the car will result in the total mass estimate of the wing.

First concept 1 was analysed. In this concept the beam would either be too heavy or yield, as can be seen in Table 5.24. As this is not acceptable, concept 2 is considered. Since carbon fibre has a better specific stiffness it was expected to have better results. However, carbon fibre does have a lower maximum tensile strength and hence it would fail in tension quite easily when using this concept. Table 5.24 shows that in concept 2 the wing is indeed significantly lighter, even though more thickness has been added to the walls. The new thickness of the beam does not pay off and in concept 2 the beam will still yield during ultimate load. Since the beam will still yield, some adjustments to the beam have to be made. The airfoil of the beam had been changed into a NACA4418 airfoil, allowing for a bigger box. The beam would also be modelled using taper, in an attempt to lower the weight while still being able to withstand stresses at the root. The taper does introduce a new difficulty into the calculations. The cross-section is changing from the root to the tip and hence the moment of inertia changes. The beam will therefore be discretised into pieces of 1 cm where the cross section is assumed to be constant. The same calculation methods apply. After an initial calculation of the tapered beam it was decided to change the taper from 0.6 to 0.8 in order to have a larger cross-section at the tip of the beam and therefore decrease the deflection at the tip. The results for concept 3 with these new dimensions can once again be seen in Table 5.24. In this concept the beam does not yield during ultimate load. It is a bit too heavy compared to the Class II weight estimate as seen in Table 4.2 but this can probably be explained by the uncommon long, slender shape of the wing which is not accounted for in a general Class II method. For completeness sake concept 4 will also be analysed, even though concept 3 proves to work in this stadium. The dimensions of concept 4 are determined in such a way that the beam will not fail in tension, as carbon fibre does have a lower tensile strength Table 5.23. As can be seen in Table 5.24 concept 4 does perform better than concept 3 in terms of weight, even though its cross-section has a significantly larger thickness. However, the difference is only 10 kg for half the wing, while a tapered, carbon

fibre box will cost significantly more, according to Dr. C. Kassapoglou.²¹ Carbon fibre prepreg can be up to 80 times more expensive than aluminium, and the production of taper in a carbon fibre wing will be even more expensive. Therefore, concept 3 is the most cost-efficient and will therefore be the most suitable option as it does not yield and has acceptable deflection values during cruise. Note that the yield stress in the structure is still 100 MPa below the maximum yield strength. This leaves some space for forces such as thrust and drag that have not been taken into account right now. As can be seen in Table 5.23, AL7075-T6 has a fatigue strength of 300 MPa for 30000 cycles. During a normal flight where the wing does not encounter ultimate load it should not undergo stresses of more than 300 MPa. The wing will therefore not fail due to fatigue within 30000 cycles.

Table 5.24: Results wing box loading

		Concept 1	Concept 2	Concept 3	Concept 4
No external force:	Deflection (m)	-0.1	-0.06	-0.05	-0.04
	Yield stress (MPa)	32.2	21.8	12.7	7.4
	Maximum shear stress (MPa)	3.3	2.9	2.1	1.3
	Mass of half wing (kg)	126.1	103.7	95.7	85.7
Load during cruise:	Deflection (m)	0.2	0.2	0.2	0.2
	Yield stress (MPa)	92.5	77.4	53.5	35.8
	Maximum shear stress (MPa)	14.2	15.4	12.1	8.1
Ultimate upwards load:	Deflection (m)	1.7	1.3	1.2	1.1
	Yield stress (MPa)	312.5	543.3	364.6	238.8
	Maximum shear stress (MPa)	96.4	101.8	79.1	52.5
Ultimate downwards load:	Deflection (m)	-0.8	-0.6	-0.5	-0.5
	Yield stress (MPa)	126.1	244.8	161.6	104.5
	Maximum shear stress (MPa)	42.6	44	34.2	22.5

For verification of the program system unit tests were performed. Parts of the program were compared with calculations done by hand to see if they matched. For every piece of code it was also checked whether the results were in compliance with Megson (2007). Figure 5.23 shows the deflection, shear and bending moment graphs that can be plotted from the code. The 6th small engine is used as an example to show that the theory of the book is translated into the code. The engine was modelled as a single point load. The first graph shows the deflection due to the point load. Just like the book tells us, the first part of the deflection graph is curved while the deflection curve is linear after the point where the load acts. The second graph shows the bending moment and the third graph shows the shear force. Both the shear force and bending moment should be zero at the point where the load acts. This is represented in the graphs, and hence shows that the program properly models the theory given in Hibbeler (2011) and Megson (2007). The beam has a deflection of 1.2m under ultimate load. One can compare this value with the maximum deflection of the Boeing 787, which deflects about 0.13m/m during ultimate load. (Dodt, 2011) The designed wing box will deflect about 0.2m/m during ultimate load without any webs or stringers, which is a realistic value.

5.4.3. Flight Hardware Structure

The Flight Hardware (FH) structure has the important structural job of transferring the loads of both wings, main and tail, to the Road Hardware (RH). This load transfer will later also impact the design of the RH structure and the design of the linkage. Some assumptions were made beforehand to help set-up and simplify the FH structure, these are:

- Standard static truss-structure assumptions will be used.
- The main wing's aerodynamic centre and loads will act at point 1. These are lift L_w , weight W_w and drag D_w .
- The tail wing's aerodynamic centre and loads will act at point 3. These are lift L_t , weight W_t and drag D_t .
- The engines thrust T act on and at the aerodynamic centre of the main wing.
- All aerodynamic moments of both the main and tail wing are zero.
- The linkages are at point 1 & 4, one link per point and modelled as a pin at 1 and as a roller at 4.
- To model going from a 3D truss to a 2D truss all forces can be halved, because the 2D cross-section represents half of the full 3D truss-structure and will thus only needed to carry half of the loads.
- Normal force failure are considered, tensile yield, compression yield or buckling, for truss beams 12 and 14.
- Normal force failures and root bending failure are considered for truss beams 23 and 34.
- Hoops are added to decrease buckling failure rate by shortening the effective lengths of the main truss beams.
- All calculated forces will be multiplied by a safety factor of 1.5, as stated in CS-23.

²¹Personal communication with Dr. C. Kassapoglou, January 2018, TU Delft

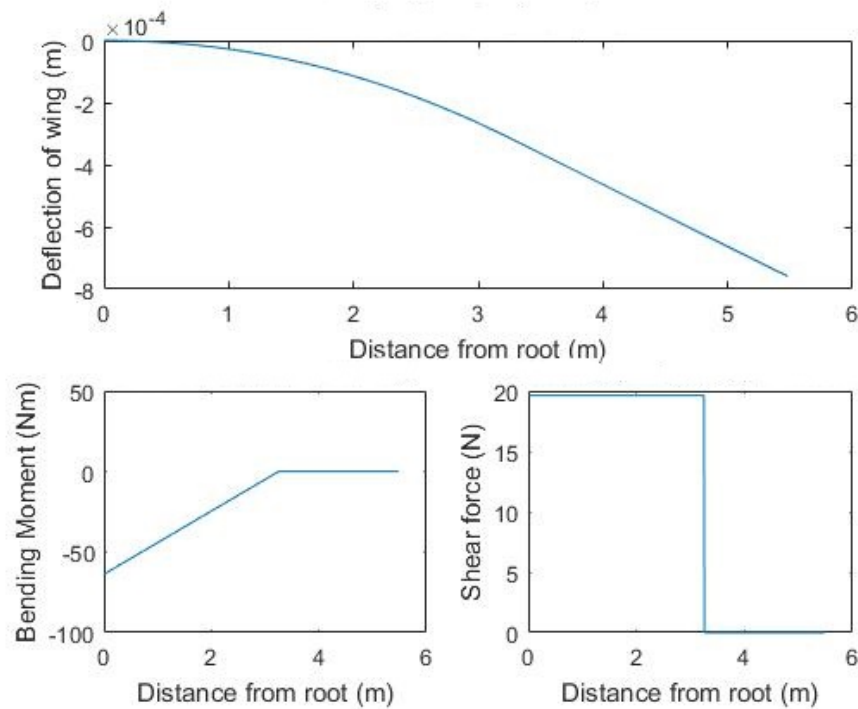


Figure 5.23: Deflection, shear and bending moment graphs of one single small engine.

Figures 5.24 and 5.25 show the chosen truss design, the free body diagram, all forces acting on it and the sign convention. Hollow green arrows represent reaction forces, while solid red arrows represent external wing loads. Following this the static equilibrium equations can be set-up, see eqs. (5.56) to (5.58).²² (Hibbeler, 2010)



Figure 5.24: The FH truss-structure and its pin and roller connections.

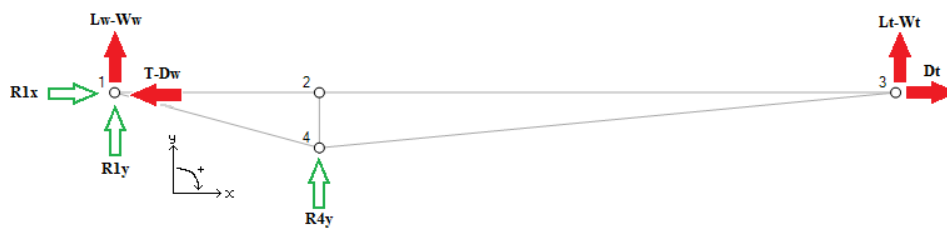


Figure 5.25: The free body diagram of the the FH structure.

$$\sum F_x \rightarrow + : 0 = R_{1x} + (D_w - T) + D_t \quad (5.56)$$

$$\sum M_4 \circlearrowleft + : 0 = L_{12}(L_w - W_w + R_{1y}) + L_{23}(W_t - L_t) + L_{24}(R_{1x} - T + D_w + D_t) \quad (5.57)$$

$$\sum F_y \uparrow + : 0 = R_{1y} + R_{4y} + (L_w - W_w) + (L_t - W_t) \quad (5.58)$$

The static equilibrium equations must be rewritten to find the three unknown reaction forces $R_{1x,y}$ and R_{4y} . It can also be noted that filling in eq. (5.56) into eq. (5.57) helps to drop the last part of that equation. The rewritten static

²²Personal communication with Dr. J. van Campen, 11 January 2018, TU Delft

equilibrium equations are as followed, also in the right order needed to solve them all.

$$R_{1x} = T - D_w - D_t \quad (5.59)$$

$$R_{1y} = W_w - L_w - \frac{L_{23}}{L_{12}}(W_t - L_t) \quad (5.60)$$

$$R_{4y} = (W_w - L_w) + (W_t - L_t) - R_{1y} \quad (5.61)$$

Using these rewritten static equilibrium equations at ten different load cases a maximum expected load can be found and designed for. For sizing the FH structure, RH structure and linkage this maximum load found will be used. Each load case represents a different flight configuration and horizontal tail setting. These ten cases are:

1. Standard one g load at take-off speed with maximal horizontal tail down deflection
2. Standard one g load at take-off speed with maximal horizontal tail up deflection
3. Standard one g load at take-off speed with no horizontal tail deflection
4. Standard one g load with only wing weights, no main and horizontal tail wing lift
5. Minimal manoeuvre g load at cruise speed with maximal horizontal tail down deflection
6. Minimal manoeuvre g load at cruise speed with maximal horizontal tail up deflection
7. Minimal manoeuvre g load at cruise speed with no horizontal tail deflection
8. Maximal manoeuvre g load at cruise speed with maximal horizontal tail down deflection
9. Maximal manoeuvre g load at cruise speed with maximal horizontal tail up deflection
10. Maximal manoeuvre g load at cruise speed with no horizontal tail deflection.

Manoeuvre load factors were used, because they were calculated to be worse than gust load factors. Both load factors were multiplied by a safety factor as mentioned in CS-23.

After checking for each load case and using the correct number found for both thrust T and drag ($D_w + D_t$), it is noted that the maximum horizontal reaction force at point 1 R_{1x} is magnitudes smaller, roughly ten times, than both maximum vertical reaction forces R_{1y} and R_{4y} . Thus a new assumption is made that R_{1x} can be neglected for any further structural analysis. For the vertical reaction forces four maximum forces can be found, a maximum positive y-direction force at point 1 and 4 and a maximum negative y-direction force at point 1 and 4. Of these four forces the highest force is chosen and then assumed that both points 1 and 4 must be able to not fail at the chosen force in both positive and negative y-directions. This maximum found force will also be passed on to the RH structure design and the linkage design. The method of joints was used to find the maximal internal force of each of the four main truss beams. These four beam are beams 12, 23, 34 and 14. Using this maximum calculated internal force the main truss beam cross-sections can be calculated as well. Simple hollow beam will be used to help keep the weight down, but the moment of inertia high. For now the truss beam will have a circular cross-section where the outer radius r_2 is twice that of the inner radius r_1 . Equations (5.62) and (5.63) give the equations for the area and the moments of inertia for the hollow beam, while eq. (5.64) give the moment of inertia for bending and only consists of the beams Steiner terms.

$$A = \pi(r_2^2 - r_1^2) \quad (5.62)$$

$$I_{Buckling} = \frac{\pi}{4}(r_2^4 - r_1^4) \quad (5.63)$$

$$I_{Bending} = 4(3\pi r_1^2) \left(\frac{L_{24}}{2} \right)^2 \quad (5.64)$$

Hibbeler (2011), Megson (2007) gives the following equations to calculate the required areas and moments of inertia.

$$A = \frac{F}{\sigma_{Y_{t,c}}} \quad (5.65)$$

$$I_{Buckling} = \frac{P_{cr} L^2}{\pi^2 E} \quad (5.66)$$

$$I_{Bending} = \frac{My}{\sigma_{Y_{t,c}}} \quad (5.67)$$

$$W = \rho AL \quad (5.68)$$

As stated in section 5.4.1 the chosen material for the truss beams and hoops was aluminium 5182-H19. The aluminium material characteristics can be seen in Table 5.23. Substituting eqs. (5.62) to (5.64) into eqs. (5.65) to (5.67) the minimum radius per beam can be found and therefore its weight can be calculated. It turns out that buckling is one the main design drivers. This is the reason hoops were considered from the first place. Each hoop place halves

the effective length a beam can buckle over. Optimising for the right amount is then crucial. Not enough hoops and buckling becomes a problem and too many hoops the truss structure becomes too heavy. Furthermore, root bending failure is also checked for the long tail arm, beams 23 and 34. The final design has a total 19 hoops, 4 on the front part, beams 12 and 14 excluding 24, and 15 on the back part, beams 23 and 34 including 24. These hoops have an inner radius r_1 of 5 mm Table 5.25 shows the rest of the final dimensions of the FH truss structure. It can be noted that the hoops are doing their job, because none of the truss beams fail in buckling.

Table 5.25: Flight Hardware structure final design dimensions

	Beam 12	Beam 23	Beam 34	Beam 14
Length (m)	1.3	3.66	3.88	1.84
Radius r_1 (mm)	6.6	6.8	6.8	8.3
Failure mode	Tensile yield	Bending	Bending	Tensile yield

The FH structure also requires a skin for aerodynamic reasons. The skin is simply the outer area of the truss. Two exceptions are made for the skin area, which are; minus the part touching the RH, plus an extra area to the sides that fill the gap between the bottom of the RH and the FH. The skin is none load carrying and will be of thin light material. This was chosen to be glass-fibre polyester resin with an 2 mm thickness. The final weight that is calculated for the full FH structure, truss, hoops and skin, is 71 kg. Comparing this to the initial weight estimate of 60 kg tells us that the FH structure is close to the mass budget.

5.4.4. Road Hardware Structure

The Road Hardware (RH) structure has to carry the Flight Hardware (FH) and all the weights of the components inside the car. For this preliminary design phase the most important weights are known and used as an estimation for the truss structure weight. These weights are the fuel, internal combustion engine (ICE), batteries, passengers and luggage. The cabin of the RH structure is split up into two: the passenger cabin and the rear part of the cabin. The passenger cabin has two large door openings and needs to keep the aerodynamic shape, resulting in a structure which cannot be analysed in detail during this phase of the vehicle development. Therefore it is assumed that the rear part of the cabin carries all FH loads, the weight of the ICE and part of the fuel which will be located inside the rear part of the cabin. The flight hardware loads will act at point D and E (Figure 5.26) and will be transferred through the back truss structure of the car cabin (Figure 5.27).

The manoeuvre load which has the highest values out of the ten load cases described in section 5.4.3 is considered as the ultimate load for sizing of the beams.

The following assumptions were made to determine the area of the beams and the weight of the whole cabin:

- Massless static truss-structure²³ (Figure 5.26)
- Two- dimensional truss due to symmetry in x-axis
- FH loads points of action are at joints D and E
- ICE+generator and fuel loads act in joints A and F
- All FH loads go through back structure of the car (Figure 5.27)
- Back car truss structure is attached to the car by a roller at point D and a pin at point A
- All loads are equally divided at points of action

To determine the loads in each beam of the rear part of the cabin truss a Free Body Diagram with the external loads and reaction forces is drawn as shown in Figure 5.27. The reaction forces at joint A and D are determined as followed:

$$\sum F_z \uparrow + = 0: \frac{1}{2}FH_1 + 2 \cdot \frac{1}{2}FH_2 - \frac{1}{2}W_f - 2 \cdot \frac{1}{4}W_{ICE+generator} + R_{zA} = 0 \quad (5.69)$$

$$\sum M_A \odot + = 0: -\frac{1}{2}W_f \cdot L_{BF} - \frac{1}{4}W_{ICE+generator} \cdot L_{BF} + \frac{1}{2}FH_2 \cdot L_{CE} + (T - D) \cdot L_{AD} - R_{xD} \cdot L_{AD} = 0 \quad (5.70)$$

$$\sum F_x \rightarrow + = 0: R_{xA} + R_{xD} = 0 \quad (5.71)$$

²³Personal communication with Dr. J. van Campen, 11 January 2018, TU Delft

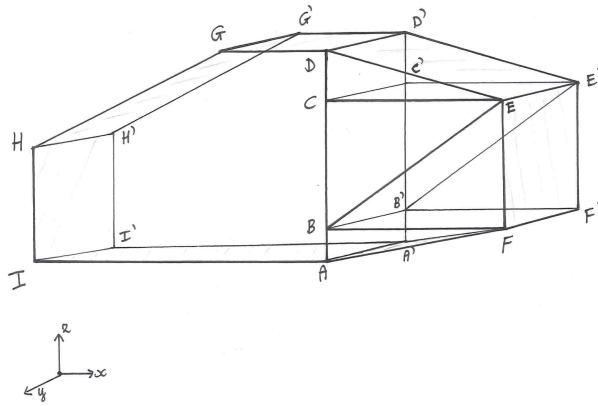


Figure 5.26: Cabin Truss Structure

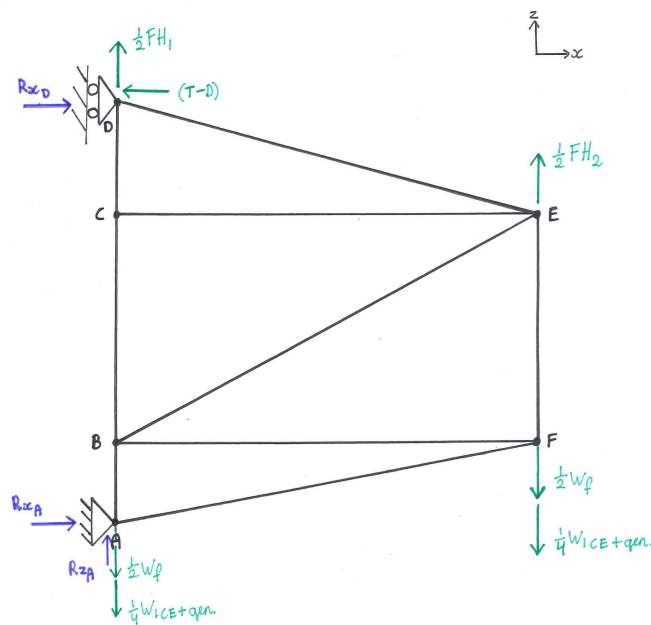


Figure 5.27: Free Body Diagram of Rear Truss Structure

$$R_{zA} = -\frac{1}{2}FH_1 - \frac{1}{2}FH_2 + W_f + \frac{1}{2}W_{ICE+gen} \tag{5.72}$$

$$R_{xD} = \frac{(-\frac{1}{2}W_f - \frac{1}{4}W_{ICE})L_{BF} + \frac{1}{2}FH_2L_{CE} + (T - D)L_{AD}}{L_{AD}} \tag{5.73}$$

$$R_{xA} = -R_{xD} \tag{5.74}$$

An assumption for truss structures is that the beams only carry normal loads(Hibbeler, 2010). The required area of the beams is determined in order for the truss structure to withstand the tensile stress, compression stress and critical

buckling without failing. Of these mentioned failure modes buckling is the highest which resulted in sizing the beams based on this failure mode. With this load case a part of the truss structure will be in tension and the other part in compression.

With the reaction forces calculated, the loads in each of the beams are determined using the method of joints (Hibbeler, 2010). The sum of forces in x-direction and the sum of forces in z-direction for each joint A, B, C, D, E and F are used to determine the normal loads in each beam.

A hollow beam will be used to keep the weight down with a circular cross-section where the outer radius r_2 is twice that of the inner radius r_1 . Equations (5.62) and (5.63) as described in Section 5.4.3 give the equations for the area and the moments of inertia for a hollow beam.

The material chosen will be the same as the material for the FH structure with material characteristics which can be seen in Table 5.23. With the length L , the Young's modulus E and the normal loads of each beam known the area can be calculated with the buckling formula eq. (5.66) as mentioned in Section 5.4.3 (Megson, 2007). Finally, the weight can be calculated with eq. (5.68) as described in section 5.4.3.

The beam loads, dimensions and weight are presented in the table below:

Table 5.26: Rear Cabin Structure Dimensions and Weights

Beam	AF	AB	BF	EF	BE	BC	CD	DE	CE
Length (m)	1.75	0.24	1.30	0.71	1.48	0.71	0.35	1.35	1.3
Radius r_1 (mm)	21.4	8.8	17.2	8.5	18.9	16	11.2	32.7	8.5
Area (mm ²)	361	60	2.31	56.8	281	201	99	840	56.8
Weight (kg)	1.6	0.04	0.80	0.11	1.10	0.38	0.09	3.01	0.2

The weight of each beam is calculated by eq. (5.68). Due to symmetry the size and hence the weight of beams A'F', A'B', B'F', E'F', B'E', B'C', C'D', D'E' and C'E' are similar to the beams stated in Table 5.26 and can be seen in Figure 5.26. For the areas of the beams AA' BB' CC' DD' EE' E'F' in y-direction for a conservative weight estimation the largest area of the beams in the xz-plane is chosen which is 840 mm². The length of these beams equals 1 m. The weight of these beams is calculated by eq. (5.68) as well. The total weight of the rear cabin truss structure resulted in 28kg.

To determine the conservative weight of the passenger cabin the area 840 mm² of the thickest beam of the rear cabin truss structure is used as well. In Table 5.27 the lengths of the passenger cabin beams are presented.

Table 5.27: Passenger Cabin Beam lengths

Beam	HI	HG	GD	AI	GG'	HH'	II'
Length (m)	0.7	1.25	0.75	1.85	1	1	1
Weight (kg)	1.56	2.78	1.67	4.12	2.23	2.23	2.23

The total weight of the cabin truss structure results in 55.03 kg which is inside the initial mass budget.

The normal stresses in each beam are calculated with eq. (5.65) and ranges between 95.3 MPa and 100 MPa. These stresses are below the fatigue stress of 190 MPa at 30.000 cycles as described in Table 5.23. These calculations were first considered with solid beams after which the hollow beams were considered. It turned out that the weight of the total truss structure is twice as small as the weight of the solid beam truss structure and is still able to withstand the ultimate loads.

The case where the vehicle is not flying is also taken into consideration. The loads acting in each beam were all smaller than the loads during flight hence the areas are determined based on the vehicle in flight configuration.

5.4.5. Car Suspension & Landing Gear

To take the landing impact and to damp the vehicle oscillations an Oleopneumatic shock absorber will be used as the vehicle suspension. This shock absorber is most commonly used in many large and small aircraft and combines a spring effect using compressed air with a damping effect using a piston which forces oil through a small hole (Raymer, 1999). The shock absorber will be attached to the electrical powered wheels. The cables of the suspension will move together with the deflection. The required shock absorber stroke depends only on the vertical velocity V_{vert} and the gear load-factor N_{gear} . Assuming general aviation a factor of 3 (Raymer (1999)) is chosen for the gear load-factor. The worst vertical velocity of the vehicle during landing will be 2.0 m/s which is lower than most Short Take-Off and

Landing (STOL) aircraft, taken from section 5.1.7. The shock absorber stroke is calculated by:

$$S = \frac{V_{vert}^2}{2g\eta N_{gear}} - \frac{\eta_T}{\eta} S_T \quad (5.75)$$

$$S_T = \frac{1}{2} \frac{3L}{p\sqrt{D_T b_T}} \quad (5.76)$$

With the following: $g = 9.81$, η = shock absorber efficiency of 0.8, η_T is the tire absorber efficiency and S_T = tire stroke. For the calculation worst case scenario is considered hence S_T is assumed to be zero. For these conditions the shock absorber stroke results in 8.5 cm with a safety margin of 3 cm added resulting in 11.5 cm. But a stroke of at least 25 - 30 cm is desirable for most aircraft. This is considered a soft landing by Raymer (1999). For these calculations the method in (Raymer, 1999) is used and Kundu (2010), Roskam (2000a), Torenbeek (1982) are used for number estimations and verification.

5.5. Linkage Design

This section will give the full technical details of the linkage design for the system. However, before beginning a simple description of the linkage system concept will be given. All of the major linkage systems are in the rear of the Road Hardware (RH) and on the front of the Flight Hardware (FH). The linkage starts at the airport where the RH will be parked in front of the FH, the RH will then reverse itself into the FH. The FH will have four wedge shaped linkage lugs which will slide into the RH. To help with linking down-scaled Scharfenberg train couplings will be used, which are attached to the front part of each lug. When the lugs are in the correct position threaded pins will automatically move into place. These threaded pins will be placed in RH. When the FH has linked with the RH there will also be an electric and electronic coupling done. Figure 5.28 gives a sketch of the final linkage concept design and all the components.

The linkage system was designed in reverse of the basic operations described above. Sections 5.5.1 and 5.5.2 will go into the design of the pins and the threads that are needed. Section 5.5.3 will show how the wedge shaped linkage lugs were design and how the Scharfenberg coupling was integrated. However, section 4.3.3 will give a description of how power and data signals will be transferred from the RH to the FH. Furthermore, for a detailed explanation of the linkage operations and how each step takes place take a look at chapter 7.

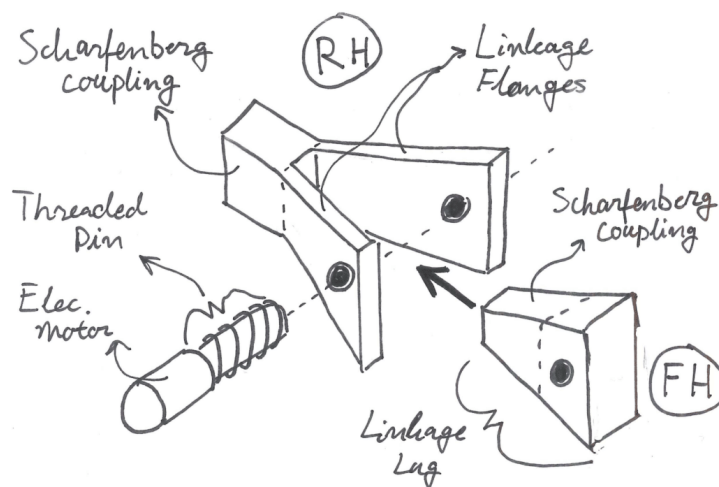


Figure 5.28: Sketch of one linkage system and all of the required components

5.5.1. Linkage Pins

In section 5.4.3 the loads applied on the linkage system were determined. These loads were then used to design the structural components of the linkage system. The first components to be examined were the load carrying pins, as explained at the beginning of this chapter. The design process starts with the design of these pins, since these components are expected to have a high risk of failure compared to other linkage components. Throughout the design, maximum loads on the linkage system were subjected to large changes. As a result, an excel document was made to easily calculate the required pin dimensions by simply filling in the forces on the linkage system. This section provides an explanation of the excel file by means of an example of the procedures followed with the final numbers that were used.

The maximum loads on the linkage system are transferred between the road and flight hardware through the pins. In section 5.4.3, it was found that vertical loads are leading in the design of the pins. For optimisation and simplified linkage purposes the pin cross section will be circular. The method from section 5.4.3 concluded that the maximum vertical force (F_L) on the upper or lower part of the linkage system equals 53 kN. Other forces acting on the pins are the car's weight and reaction forces. It is assumed that the loads act on the pin as distributed loads, since the entire pin is in contact with the surrounding lug. The loads are shown in fig. 5.29.

Major assumptions made during the pin design are:

- Loads are evenly distributed over pin length and act as distributed loads (shown in fig. 5.29).
- The load carrying parts of the pin in and outside the lug are of equal length.
- Total pin length is set by Scharfenberg coupling constraint and equals approximately 10.2 cm, from section 5.5.3.

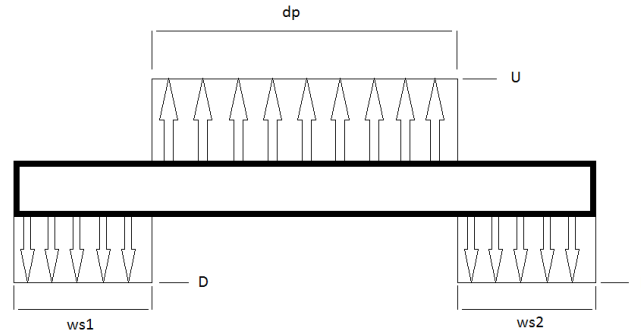


Figure 5.29: Schematic drawing of the loads acting on a pin

The next step is to determine the reaction forces on the pins. At the maximum load case, which resulted from section 5.4.3, the vertical upward force exerted on the linkage equals 53 kN, while the RH vertical downward force (F_{RH}) that was chosen equals 15 kN. This value resulted from the initial weight estimation of the entire vehicle, that was approximately 1500 kg. A worst case scenario where only two pins carry all the load was considered, which resulted in a RH weight of 15 kN acting on the linkage system. Consequently, the reaction forces on the linkage system could be calculated due to force equilibrium. From the values above, the reaction force (F_R) equals: $53 - 15 = 38$ kN and acts downwards at the locations of ws1 and ws2 shown in fig. 5.29. Each link carries half of the total forces acting on the linkage system, resulting in an upward lift force, downwards RH force and resultant force of 26.50, 7.50 and 19.0 kN respectively. Then, the distributed loads on dp (U) and ws1 & ws2 (D) are found using eq. (5.77) and eq. (5.78), respectively. In these calculations, a safety factor (n) of 1.5 was used in order to make the system safe for linkage failure.

$$U = \frac{nF_L}{wp} \quad (5.77)$$

$$D = \frac{n(F_R + F_{RH})}{ws1 + ws2} \quad (5.78)$$

Filling in eq. (5.77) and eq. (5.78) results in a distributed load of 782 kN/m acting upwards at the middle section of the pin (dp) and downwards at both sides (ws1 & ws2). This is a result of the assumption that the sum of forces equals zero and the total length of ws1 and ws2 equals wp.

At this point, all the values shown in fig. 5.29 are known and the required pin diameter can be determined. First, material properties are required. Several materials, such as steel, carbon and various types of aluminium have been considered. If steel is used, the linkage becomes unnecessarily heavy and no volume benefits are a result. The only positive effect is a lower price, but considering larger benefits regarding volume and weight obtained by using aluminium this was considered the best material. Carbon fibre is not suitable due to the shapes of these parts and its costs. Finally, aluminium 5182-H19 was considered the best option due to its relative low weight, its compliance with the volume requirements set (section 5.5.3), acceptable price and desirable material properties such as manufacturability, availability and recyclability (section 5.4.1). The material has a compressive strength of 413 MPa, which is lower than the tensile strength and therefore used for further analysis.

The load cases considered are shear and bending. First, shear is analysed. All loads act as shown in fig. 5.29, therefore it makes sense that the maximum shear force acts at the most inward locations of ws1 and ws2. From symmetry, the loads acting at the left side of the pin are equal to the ones at the right. The shear forces throughout the length of the pin are shown in fig. 5.30.

The maximum shear force acting on the pin is equal to 19.9 kN. To find the required radius eq. (5.79) is rewritten to eq. (5.80). The maximum shear stress on a circular closed cross-section is equal to four thirds times the average shear stress (Hibbeler, 2011). Therefore, the term $\frac{4}{3}$ is added to eq. (5.79).

$$\frac{4}{3}\tau = \frac{F}{A} = \frac{F}{\pi r^2} \quad (5.79)$$

$$r = \sqrt{\frac{3F}{4\pi\tau}} \quad (5.80)$$

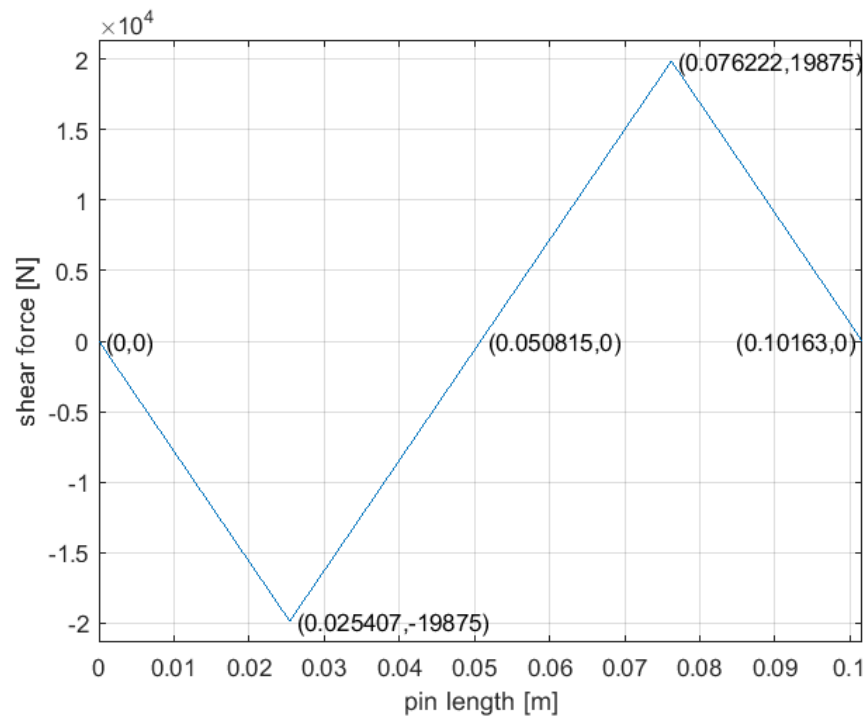


Figure 5.30: Internal shear distribution over pin length

The material's shear strength equals 240 MPa.²⁴ The shear force is also known and equals 19.9 kN. After these numbers were filled in eq. (5.80), the minimum diameter for shear equals 0.89 cm.

For bending, the maximum moment has to be found. From analysis, it was determined that the maximum bending moment acts at the centre, so at 5.1 cm. Taking the moments around this point resulted in a maximum moment of 505 Nm. The cross section is circular and closed, resulting in the bending stress formula shown in eq. (5.81). The radius can be found by rewriting eq. (5.81) to eq. (5.82).

$$\sigma = \frac{My}{I} = \frac{Mr}{\frac{1}{4}\pi r^4} = \frac{4M}{\pi r^3} \quad (5.81)$$

$$r = \sqrt[3]{\frac{4M}{\sigma\pi}} \quad (5.82)$$

In eq. (5.82), the highest moment (M) is used and equals 505 Nm. The lowest yield strength (σ) of the material is 413 MPa. As a result, the required diameter for bending is 2.4 cm. It follows that the bending stresses on the pin are leading for the design and the lowest required pin diameter equals 2.4 cm.

5.5.2. Pin Threads

The linkage has to provide a non-permanent joint between the FH and RH. In order to make this possible, the pins will become threaded pins. The introduction of threaded pins should make it easier to design an automated system. Once the lug holes are aligned with the pins, electric motors are used to move the threaded pins through the lugs. The threaded pin will pull itself through the hole due to its rotation, so no mechanism to move the electric motors is required. This section explains how the thread design is determined and what electric motors will be used.

The thread design is relatively straight forward. A method from Budynas et al. (2010) is used. A relation between the tensile stress area calculated in section 5.5.1 and the threaded pin dimensions is given in the book. Figure 5.31 shows the minor, pitch and major diameter definitions used throughout this section.

²⁴<https://www.makeitfrom.com/material-properties/5182-H19-Aluminum>, (Retrieved on 9 January 2018)

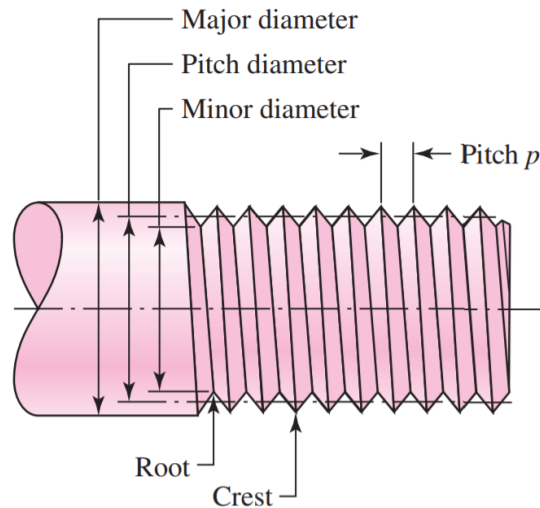


Figure 5.31: Explanation of the minor, pitch and major diameters of a threaded pin. (Budynas et al., 2010)

The first step to find the thread dimensions was to determine the relation between the so called tensile stress area and the minor diameter area. The relation is approximately 1.06, so the tensile stress area equals 1.06 times the minor diameter area (table 8-2, page 413 of Budynas et al. (2010)). The diameter of 2.4 cm, as found in section 5.5.1 is used to find the tensile stress area. Using the ratio of 1.06, it was found that the minor diameter has to be 2.33 cm. The tensile stress area is the average of the minor and pitch diameters (Budynas et al., 2010). Therefore, the major diameter could easily be calculated and was found to be 2.64 cm. From the same table, it also followed that the required pitch, as shown in fig. 5.31 is approximately 0.21 cm.

The automated system to move the pins requires electric motors. The motors could be chosen after the required torque output and the maximum dimensions were known. The electric motor diameter should not be larger than the height of the linkage box. The required torque (T_R) can be found using eq. (5.83) (Budynas et al. (2010)).

$$T_R = \frac{F d_m}{2} \left(\frac{p + \pi f d_m}{\pi d_m - f p} \right) \quad (5.83)$$

In eq. (5.83), F is the longitudinal force acting on the pin. During linkage, this force should be minimal since it acts in a horizontal plane on which no forces should act during the linkage procedure. In order to take small misalignment into account, F is taken as 500 N. Other values were a pitch (p) of 0.0021 m, minor diameter (d_m) of 0.0232 m and a friction coefficient (f) of 0.3. The friction coefficient of lubricated aluminium is used.²⁵ The system will be lubricated in order to decrease wear during operation. Finally, the engine should produce a torque of approximately 1.92 Nm. An electric motor (from a cnc machine) that weights only 900 grams with a maximum diameter of 63 mm and a length of 75 mm is available and will be used.²⁶

5.5.3. Linkage Lugs

RH packaging wise the linkage lugs should be as small as possible to fit in the already cramped RH structure. Smaller lugs will also help keep the extra weight the linkage system brings with it down. The current design demands four linkage lugs, two at the top of the FH structure and two at the bottom of the FH structure, see points 1 and 4 of fig. 5.24. These will slide into the RH structure at either the roof height or just above the rear packaging compartment, see points D and E of fig. 5.27. Here in the RH structure there will be two side flanges per lug. As state before a threaded pin will pass through both flanges and lug at each of the four linkage locations. To help these lug slide in better a wedge shape was considered. Taking inspiration from woodworking a convenient wedge angle was looked up. Sources say

²⁵https://www.engineeringtoolbox.com/friction-coefficients-d_778.html, (Retrieved on 11 January 2018)

²⁶<https://dutch.alibaba.com/product-detail/28v-brushless-dc-electric-motor-torque-4nm-electric-vehicle-brushless-dc-motor-60697515358.html?spm=a2700.8699010.29.47.641c3373cqDPak>, (Retrieved on 11 January 2018)

that a wedge should have an angle of about 8° till 10° .^{27,28,29} However, using these angles would mean our lugs would increase in rear size a bit too fast. Choosing for a 4° angle on all sides helps decrease the fast widening of the lugs, but still retains roughly a total 8° slope of a wedge. The front of the lug must be kept free to place a Scharfenberg coupling in it. That leaves the rear of the lug to be used for a pin insert. Figure 5.32 shows a correctly scaled 3D model of one wedge shaped linkage lug.

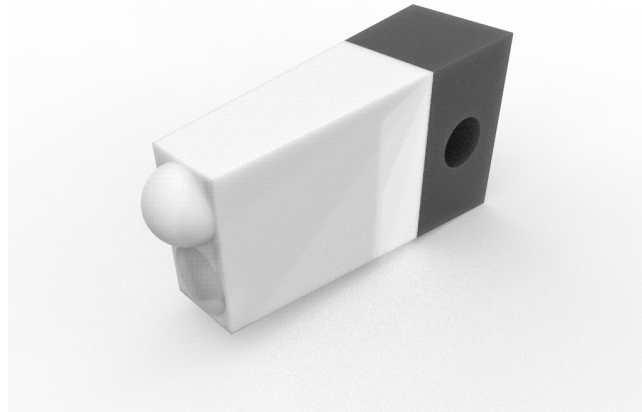


Figure 5.32: 3D scaled model of the wedge shaped linkage lug

As stated before, a Scharfenberg train coupling is desired in the front part of the linkage lug. The reasoning is as followed. When the lugs slide into the RH structure no left to right as well as up and down movement is possible, due to the lug rubbing against the side flanges. The Scharfenberg coupling will prevent movement along the last free axis, forward and backwards, by linking just like a train does.³⁰ This means there is an opposite Scharfenberg coupling at the end at each of the four linkage 'holes' in the RH structure. Choosing to use train technology does bring some problems with it. It is unsure if these couplings can be scaled-down to this size. Using VOITH (2012) it was determined that if scaled-down the following scale needed to be used. Length:Width:Height must be 3:1:2. Furthermore, the Scharfenberg coupling will not be load carrying during operations. All the loads will be carried by the lugs and pins, flanges and thread pin. In fig. 5.32 the lighter coloured front two thirds of the linkage lug represent the Scharfenberg coupling and the rest the load carrying lug.

With the front dimensions of the linkage lug nearly set, the rear of the lug is also pretty constraint. Keeping rear lug height in mind an assumed minimum Scharfenberg coupling length of 10 cm was chosen. This gives the front of the lug a 3.33x6.67 cm surface face. Using the same logic of trying to keep the lug as small as possible, only a 5 cm long load carrying lug is chosen. This length is also the lug width w . The total linkage lug length is now brought to 15 cm. Having these outer dimension values, wedge angles and the pin diameter from section 5.5.1 the final important lug design dimension can be calculated. These are edge distance e and lug thickness t from/at the centre of the diameter. The lugs do have a slope, but these two lengths are assumed to be correct for any further calculations. Using simple geometry these two final dimensions can be found and are shown in table 5.28 together with the rest of the linkage lug dimension. Figure 5.33 gives a reference of all basic lug dimensions.³¹ It is assumed that the linkages flanges inside the RH will have the same shape as the load carrying linkage lugs, but only have half the thickness of 2.05 cm. Taking the lug thickness and twice the flange thickness gives the final total minimum thickness needed for packaging and also give the earlier defined pin length of 10.2 cm.

After determining the major dimensions, it can be calculated if the lugs are big enough. The graphs from Bruhn (1973, pp. D1.6-D1.9) were used to calculate for the lugs. Important area equations and strength equations are given by eqs. (5.84) to (5.90). Furthermore, the following ratios are needed: w/D , t/D , e/D and A_{av}/A_{br} . Using these ratios K_t , K_{brY} and K_{Yt} can be found in Bruhn (1973). Note that all ratios are in acceptable ranges, except t/D which is quite high. For these K values the worst one is taken from each chart, from Bruhn (1973), for further calculation, this has to do with the material selection. The linkage lugs are made out of aluminium 5182-H19, just as the FH and RH

²⁷<https://www.canadianwoodworking.com/plans-projects/make-wood-hand-plane-afternoon>, (Retrieved on 11 January 2018)

²⁸<http://wiki.diyfaq.org.uk/index.php?title=Wedge>, (Retrieved on 11 January 2018)

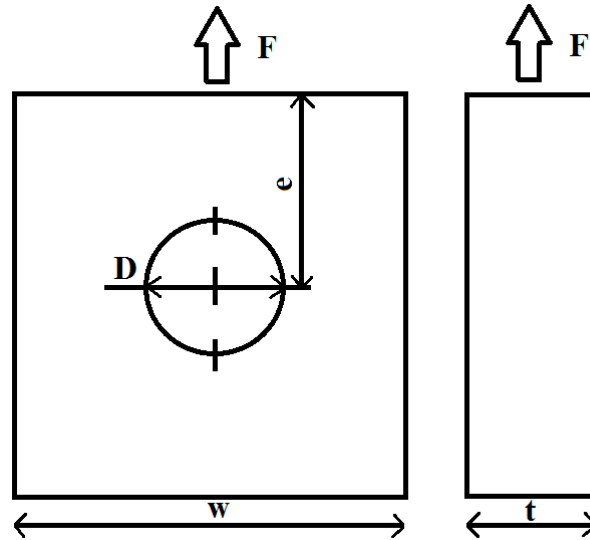
²⁹<http://www.finewoodworking.com/1992/04/01/clamping-with-wedges>, (Retrieved on 11 January 2018)

³⁰<https://dcab-public.sharepoint.com/en/products>, (Retrieved on 11 January 2018)

³¹<https://mechanicalc.com/reference/lug-analysis>, (Retrieved on 22 January 2018)

Table 5.28: Final linkage lug dimensions at total lug length of 15 cm

	width	height	diameter D	edge distance e	lug width w	lug thickness t
front	3.33 cm	6.67 cm	-	-	-	-
back	5.43 cm	8.76 cm	-	-	-	-
lug	-	-	2.4 cm	4.2 cm	5.0 cm	5.1 cm

Figure 5.33: Basic lug dimensions D , e , w and t , not to scale

structures. The material properties can be found in table 5.23. The calculated ultimate load from section 5.4.3 is once again used as the force input of eqs. (5.87) to (5.90). However, this force is multiplied by an aerospace safety factor of 1.5 (for CS-23) and then divided by the number of lugs at each point, which is 2 for both the top and bottom linkage locations.

$$A_t = w \cdot t \quad (5.84)$$

$$A_{br} = D \cdot t \quad (5.85)$$

$$A_{av} = \frac{6}{\frac{4}{(e-0.5\cos(45^\circ)D)t} + \frac{2}{(e-0.5D)t}} \quad (5.86)$$

$$A_t = \frac{F_Y}{K_t \sigma_{Y_t}} \quad (5.87)$$

$$A_{br1} = \frac{F_{br} Y_t}{K_{br} \sigma_{Y_t}} \quad (5.88)$$

$$A_{br2} = \frac{F_{br} Y_c}{1.85 \sigma_{Y_c}} \quad (5.89)$$

$$A_{br3} = \frac{F_t Y}{K_{Y_t} \sigma_{Y_t}} \quad (5.90)$$

With all ratios, current design areas, K values and the force known the required lug areas can be calculated and compared with the current design ones. The results can be seen in table 5.29. This table clearly shows that the lug will not fail in any of the possible failure modes. The main reason is that the current design has a really big thickness of on average 5.1 cm. Furthermore, the flanges will also not fail. Although, they have half the areas as the lugs, they also only have half the force acting on them. These two halves cancel each other. At the current design the pins will fail first.

Finally, a quick and rough weight check can be done. Calculating for four square aluminium blocks of 15x10.86x8.76 cm gives a mass of about 15 kg, eq. (5.68). These lengths represent the length x width, both flanges and the lug, x height. This is a very conservative estimate, because the slope angle, hollow Scharfenberg coupling parts and threaded pin

Table 5.29: Comparison between current design lug areas and required lug areas

current lug areas		required lug areas	
A_t	25.41 cm ²	A_t	1.56 cm ²
A_{br}	12.11 cm ²	A_{br1}	0.58 cm ²
A_{av}	16.46 cm ²	A_{br2}	0.52 cm ²
-	-	A_{br3}	6.02 cm ²

hole were all neglected. However, for a first weight estimate of 15 kg for only the major structural parts of the linkage systems is within the technical resource allocation section 4.2.

5.6. The Final Product

The final design resulted in a two-configuration vehicle, a road configuration that drives electrically and a flight configuration that uses distributed electric propulsion (DEP) and clip-on wings technology. This section will give a top-level description of the major design choices throughout the technical designing phase. Considering technical sizing with respect to Flight Propulsion & Power, Aerodynamics, Stability & Control, Structures and Linkage of both configurations, the most important parameters will be stated. Furthermore, the compliance of the design with respect to the requirements is demonstrated in the form of a compliance matrix in section 5.6.1.

The vehicle has a hybrid powertrain in both configurations as a result of the sustainability and range requirements. Electric propulsion in both road and flight configurations increase the efficiency of the vehicle and therefore its environmental impact and range. The main power source is bio-ethanol stored in two 35 and one 135 litre tanks and is converted to electric power by a Rotax 915 internal combustion engine and a generator. In addition to the combustion engine, a battery pack of 10 kWh is installed. All these parts are stored in the road hardware to improve safety and simplicity of the linkage system.

The vehicle has a high wing design that uses distributed electric propulsion (DEP). This is visualised in Figure 5.34. The use of DEP results in a highly efficient and sustainable wing design, with an aspect ratio of 17. The propellers increase the airflow over the wing, resulting in:

- Greatly increased lift at low speeds
- Reduced drag during cruise due to smaller, optimised wing size
- Reduced aircraft noise
- Extreme redundancy
- Optimised propellers for small and high speeds
- Ability to actively manipulate boundary layer, vortexes and lift distribution (beyond the scope of this report)

The use of DEP caused an increase in the lift coefficients during landing and take-off, which are 3.09 and 2.37 respectively. This majorly improved the overall aerodynamic efficiency (L/D) of the vehicle, however the drag is quite high due to the fuselage being shaped as a car which is not optimised for flight. However, the overall effect due to DEP is favourable. The lift to drag ratio for cruise, landing and take-off are, respectively, 12.93, 7.74 and 9.48.

The vehicle has a T-tail configuration in order to keep the horizontal tail surface as far as possible outside the destabilising downwash region of the wing. The usage of DEP results in unconventionally high lift coefficients, which required a fully movable horizontal tail in order to achieve an acceptable tail size. The isometric view of the vehicle is shown in Figure 5.34.

As a result of its lightweight applications and relative simplicity during calculations, the main structural elements of the vehicle are made of truss structures. The car chassis, rear compartment and the flight hardware's tail are all made of an aluminium 5182-H19 truss structure. Only the wing box is made of a different aluminium, namely Al7075-T6. The main structures use the 5182-H19 aluminium for manufacturing reasons. In this report only the middle and rear sections of the road hardware are designed. These are harder to design due to the unconventional attachment of flight hardware to the rear and roof of the vehicle. The front section, on the other hand, is similar to the chassis of conventional lightweight sports cars and was not designed in detail. Finally, the middle and rear sections of the road hardware truss structures have masses of 27 kg and 28 kg, respectively. The flight hardware truss structure has a mass of 71 kg.

The unique linkage system of the vehicle, which is installed in order to attach the flight hardware to the road hardware, consists of three major components: load carrying pins, wedge shaped lugs attached to the flight hardware and a Scharfenberg coupling mechanism. When the linkage procedure is started, four holes located at the rear of the car - two in the roof and two at both sides at middle height - open and the car automatically aligns with the flight hardware. Subsequently, the lugs are aided by their shape and slide into the rear of the road hardware. When these lugs reach the end of the holes, the mechanical Scharfenberg couplings couple and attach both configurations. If all four couplings attach, the holes in the lugs should align with the threaded pins. This mechanism is only installed to aid the alignment of the load carrying pins. Each lug has one load carrying pin that is moved through the lugs by electric motors from a cnc machine. After all four pins pulled themselves through and reached the end, the motors stop working and a go sign is presented to the user. After the structural coupling is finished, the electric and control couplings are activated.

This major parameters of the design are clearly shown in Table 5.30.

The maximum range indicated in Table 5.30 allows the vehicle to reach the major cities in Europe, this is graphically

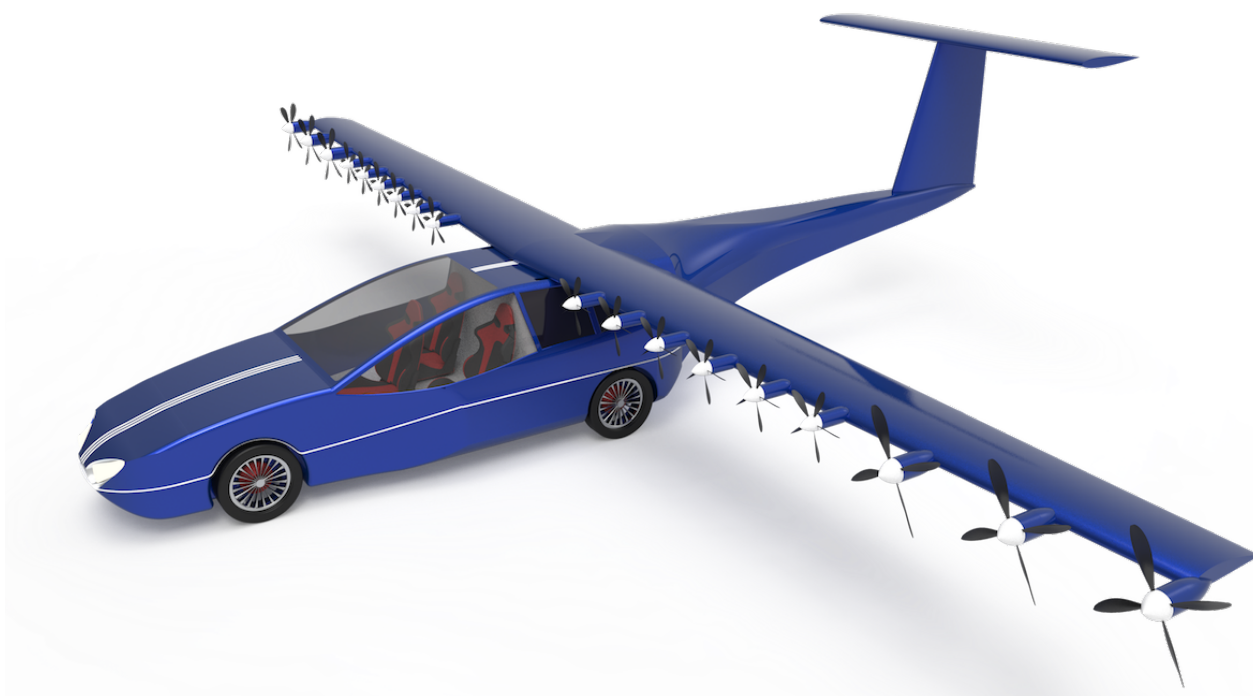


Figure 5.34: Isometric view of the vehicle

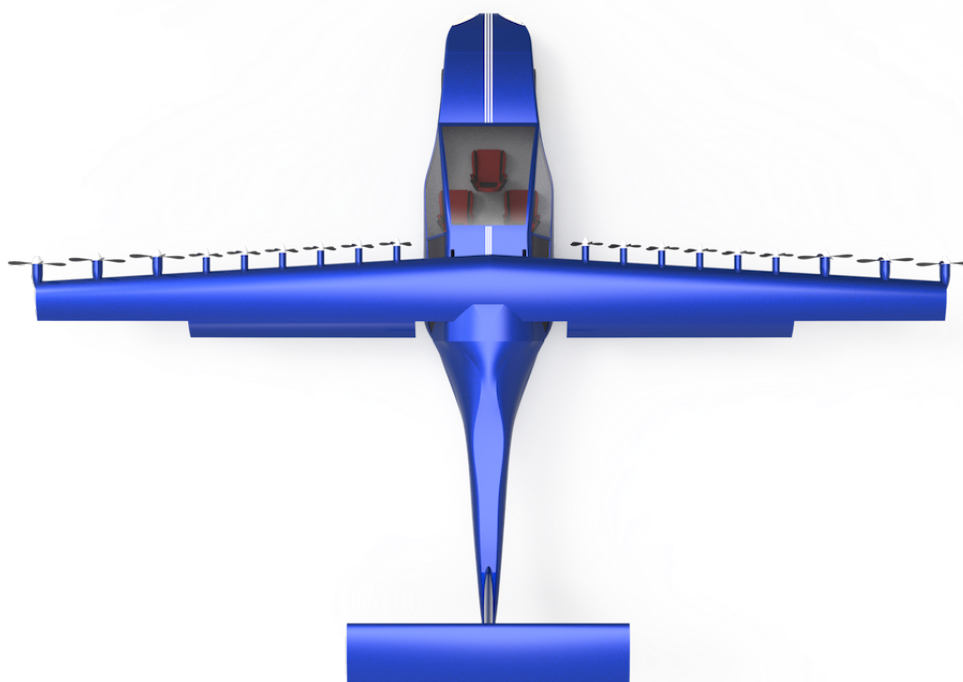


Figure 5.35: Top view of the vehicle

displayed in Figure 5.37. The small circle represent the range of 556 km at maximum payload using E85 fuel (excluding reserves) The large circle represents the maximum range of 940 km with the pilot and fuel as only payload and using E10 fuel. A reserve of half an hour at maximum cruise speed has been subtracted, but the climb distance of 39 km has been included in the maximum range.³²

³²<http://obeattie.github.io/gmaps-radius/?lat=52.354714&lng=4.898623&z=5&u=km&r=556>, (Retrieved on 23 January 2018)



Figure 5.36: Rear view of the vehicle showing the flaps and the separate configurations

Table 5.30: Table summarising the major design parameters for the flight configuration

Parameter	Value	Unit
Aspect ratio	17	-
Surface area	8.42	m ²
Span width	11.96	m
Maximum take-off weight	1600	kg
Empty mass	1176	kg
Maximum payload	360	kg
Capacity	3 adults	-
Drivetrain	Series hybrid	-
Number of engines	18	-
Maximum road speed	140	km/h
Cruise speed	296	km/h
Engine power	132	kW
Automotive dimensions	4.5 (L), 1.85 (W), 1.47 (H)	m
Aerospace dimensions	8.45 (L), 11.96 (W), 2.75 (H)	m
Maximum height of the fuselage	1.3	m
S_h	2.42	m ²
S_v	1.1	m ²
Maximum range	940	km
Fuel economy (cruise, E85)	19.6L/100km	-

5.6.1. Compliance Matrix

Now that the design of the product is completed, it is necessary to check whether the product meets the requirements. This will be done with a compliance matrix. This can be seen in Tables 5.31 and 5.32. The requirements are numbered according to the scheme of Chapter 3 in the first two columns of the tables.

As can be seen in the compliance matrix, there are still a lot of requirements that still need to be determined. This is due to the product still being in the preliminary design phase and that further research, development and testing is required to see if these undetermined requirements are met. This is discussed in more detail in Chapter 12. Further-

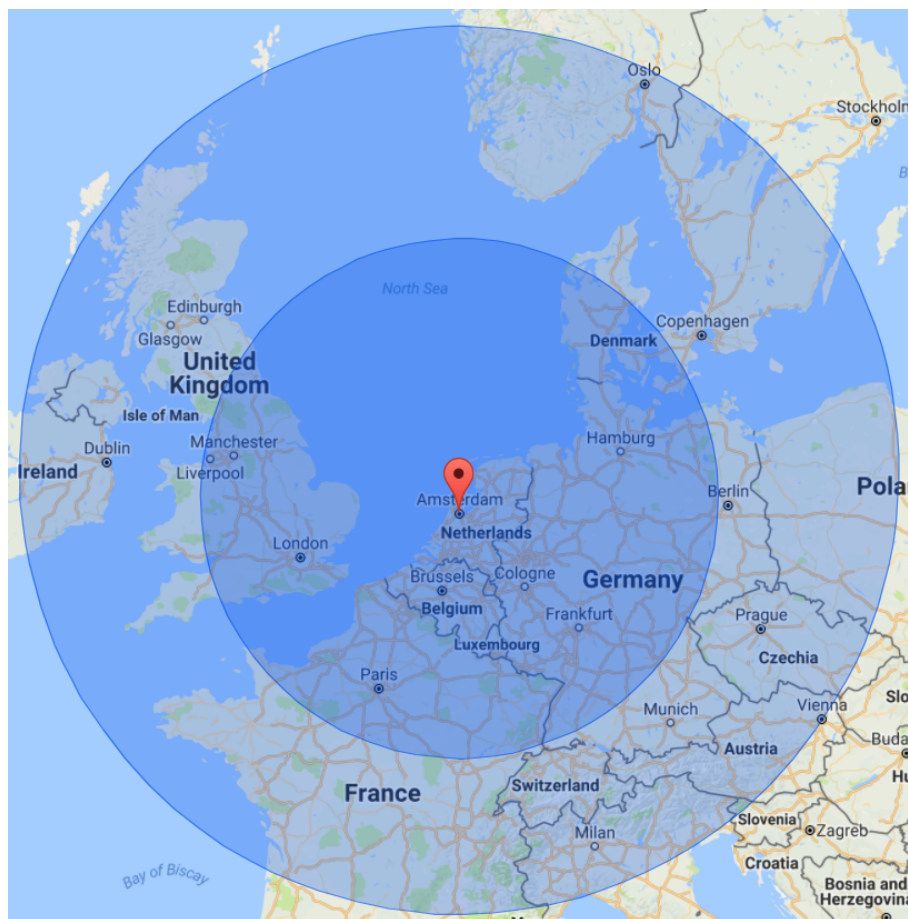


Figure 5.37: Map showing the maximum range of 940 km using E10 fuel and the range of 556 km at maximum payload using E85 fuel.

more, there are some requirements that were not met. The reason for these requirements not being met are discussed below.

For **CoW-Sys-Air-2.4** (Chapter 3), the gliding distance at the landing phase of the vehicle increased due to the increased thrust from the DEP propellers, causing it to need a longer landing field length than what was required. For **CoW-Mis-Mar-1.2** (Chapter 3), the purchase cost that the road vehicle was designed for is €150000 instead of €80000 for reasons that are explained in Chapter 10. Moreover, **CoW-Mis-Sus-1.Air** (Chapter 3), the fuel consumption in flight configuration was not made. The aircraft is designed for a maximum payload of 360 kg and is therefore relatively heavy. In addition to this, the cruise speed that should be achieved at this weight is relatively high. Therefore, the fuel consumption was higher than the stated requirement. Recommendations that could result in achieving these requirements are mentioned in Chapter 13.

Table 5.31: Technical Compliance Matrix

Requirement Type	Requirement	Check (Y/N)
CoW-Sys-Tech	1.1	Y
	1.2	Y
	1.3	Y
	1.4	Y
	2.1	Y
	2.2	Y
	3.1	Y
	3.2	Y
	3.3	Y
	3.4.0	Y
	3.4.1	Y
	3.5.0	Y
	3.5.1	Y
	3.5.2	Y
	CoW-Sys-Car	1.1
2.1		Y
2.2		Y
3.1		Y
3.2		Y
3.3		Y
4.1		TBD
CoW-Sys-Air	1.1	TBD
	2.1	Y
	2.2	Y
	2.3	Y
	2.4	N
	3.1	Y
	3.2	Y
	3.3	Y
	4.1	TBD

Table 5.32: Non-technical Compliance Matrix

Requirement Type	Requirement	Check (Y/N)
CoW-Mis-Sus	1.Car	Y
	1.Air	N
	2.Car.0	TBD
	2.Car.1	Y
	2.Car.2	TBD
	2.Car.3	TBD
	2.Car.4	TBD
	3.Car	Y
	3.Air	Y
	4.1.0	Y
	4.1.1	TBD
	4.1.2	Y
	4.1.3	TBD
	4.1.4	Y
	4.1.5	TBD
	4.2	TBD
	4.3.0	TBD
	4.3.Car	Y
	5.1	Y
	5.2.Car	Y
5.2.Air	Y	
CoW-Mis-Mar	1.1	N
	1.2	TBD
	2.1	Y
	2.2	Y
	2.3.0	TBD
	2.3.1	TBD
	2.3.2	TBD
	2.3.3	TBD
	2.3.4	TBD
	2.3.5	TBD
	2.3.6	TBD
	2.3.7	TBD
	2.3.8	TBD
	2.3.9	TBD
	2.3.10	TBD
2.4	Y	
3.1	Y	

6

Technical Sensitivity Analysis

In order to check the robustness of the design, the sensitivity of technical design parameters is investigated in this chapter. The factors that will have the most impact on the overall design are the aspect ratio (section 6.1), taper ratio (section 6.2), $C_{L_{max}}$ (section 6.3) and mass (section 6.4).

6.1. Effect of Decreased Aspect Ratio

The vehicle has an aspect ratio of 17, which is high compared to other aircraft. In order to examine the sensitivity of the design with respect to aspect ratio, the aspect ratio will be decreased by 30% to a value of 11.9. The span is kept the same, otherwise the 18 propellers would not fit on the wing. This will have an effect on the performance, aerodynamics, structural design, tail size and linkage.

6.1.1. Effect on Cruise Performance

The baseline aircraft needs 122 kW in shaft power. With a 30% lower aspect ratio of 11.9, the increase in induced drag leads to an increase to 130 kW, the Oswald factor is also changed. This decreases the span to achieve this lower aspect ratio. Another way of decreasing the aspect ratio is to increase the chord, this would drive the design to a more normal size, because the span was the same as reference aircraft, with a far smaller area. The area is increased from 8.47m^2 to 12.02m^2 . This leads to a different C_{D_0} . The power requirement is increased to 133 kW shaft power. The fuel economy is proportional to the required power, since the speed is kept the same.

6.1.2. Effect on Aerodynamics

Aspect ratio has a large effect on the wing parameters and the aerodynamic characteristics. When decreasing it by 30%, the surface area of the wing increases greatly if the span is constant. This leads to higher chord lengths and larger sweep angles. For the lift curve however, the gradient decreases as they are directly proportional. This means that the curve is less steep, meaning lower C_L values at the same angles of attack and larger stall angles at all configurations. As the overall C_L values decrease, the induced drag coefficients increase and the aerodynamic centre moment coefficients become more positive for all configurations as well. The results of this analysis can be seen in tables 6.1 to 6.5:

Table 6.1: Effect of Aspect ratio on Wing Planform

Wing Parameters	A	S	C_r	C_t	\bar{C}	Λ_{LE}	$\Lambda_{0.25C}$	$\Lambda_{0.5C}$
Standard	17	8.41	0.782	0.625	0.706	1.50	1.12	0.749
30% Decrease	11.9	12.02	1.12	0.893	1.01	2.14	1.60	1.07

Table 6.2: Effect of Aspect ratio on Lift Characteristics (Part I)

Lift Characteristics	A	$C_{L\alpha}$	$C_{L\alpha,landing}$	$C_{L\alpha,take-off}$	α_s	$\alpha_{s,landing}$	$\alpha_{s,take-off}$
Standard	17	0.0935	0.105	0.102	11.96	9.76	12.59
30% Decrease	11.9	0.0892	0.101	0.0976	12.63	10.72	13.55

Table 6.3: Effect of Aspect ratio on Lift Characteristics (Part II)

Lift Characteristics	A	$C_{Lcruise}$	$C_{Llanding}$	$C_{Ltake-off}$	$C_{L0,cruise}$	$C_{L0,landing}$	$C_{L0,take-off}$
Standard	17	0.561	3.09	2.37	0.374	2.36	1.66
30% Decrease	11.9	0.535	2.95	2.26	0.357	2.27	1.60

Table 6.4: Effect of Aspect ratio on Moment Characteristics

Moment Characteristics	$C_{m_{ac,wing}}$	$C_{m_{ac,landing}}$	$C_{m_{ac,take-off}}$
Standard	-0.0939	-0.805	-0.769
30% Decrease	-0.0898	-0.801	-0.765

Table 6.5: Effect of Aspect ratio on Drag Characteristics

Drag Characteristics	C_{D0}	$C_{Dcruise}$	$C_{Dtake-off}$	$C_{Dlanding}$
Standard	0.0338	0.0434	0.2504	0.3993
30% Decrease	0.0261	0.0391	0.2966	0.4901

6.1.3. Effect on Structural Design Wing

Due to the different wing area, the wing box can become larger. This results in a more stiff box, which has a better endurance when it comes to bending. If the same wing box thicknesses are used as before the wing will have very small deflections but will weigh about 300 kg. However, one can optimise the new wing box to have a mass of 165 kg with a maximum deflection of 0.7m during ultimate load, which is still an acceptable value. This means that with the new aspect ration the wing weight can be decreased by 35 kg.

6.1.4. Effect on Horizontal Tail Size

When changing the aspect ratio from 17 to 11.9 quite some important stability parameters will be influenced. First of all, because of the increase in wing surface area while keeping the wingspan the same, the mean aerodynamic chord increases. This has a negative influence on controllability. As was mentioned in the previous subsection, the weight of the wing decreases from 200 to 164 kg. This influences the $x_{cg,oeuw}$ of the flight configuration, which changes from 3.21 m to 3.26 m. Moreover, taking into account the changes in the moment around the aerodynamic centre, the lift at zero-angle of attack and other aerodynamic parameters used in the horizontal tail surface analysis, the horizontal tail surface would increase from 2.42 m² to 4.84 m², which is a 100% increase.

This shows that the horizontal tail is very sensitive to a change in aspect ratio. This is also expected, as changing the aspect ratio, while keeping distributed electrical propulsion, would overpower the wing. As not only the C_L is high in this case due to DEP, but the wing surface is also large. This would require a large horizontal tail surface in order to keep the aircraft longitudinally stable. Therefore, it can be concluded that DEP would only prove beneficial with a high aspect ratio.

6.1.5. Effect on Linkage

A major change of the horizontal tail has a major effect on the the linkage system. This was already seen during the technical development of the whole system. A bigger horizontal tail creates higher loads and moments on the FH structure which must pass through the linkage lugs into the RH structure. The linkage will become bigger or more numerous. Bigger or more lugs will increase the weight and bring up packaging problems.

6.2. Effect of Increased/Decreased Taper Ratio

The taper ratio will be increased/decreased by 10%. This will have an effect on the aerodynamics and the structural design of the wing. It will also affect the oswald efficiency, but this effect is very small and hence it is neglected in this section.

6.2.1. Effect on Aerodynamics

After analysing the taper ratio effects on aerodynamics, it can be observed that it does not affect the aerodynamic characteristics but it does affect the wing planform. When increasing the taper ratio by 10% to 0.88, the root chord decreases and the tip chord increases if the span and wing area is constant. This change also decreases the sweep angles. However, if the taper ratio decreases by 10% to 0.72, it has the opposite effect. Decreasing taper ratio increases the root chord and decreases the tip chord at constant wing span and area. This also leads to higher sweep angles. This is shown in table 6.6:

Table 6.6: Effect of Taper ratio on Wing Planform

Wing Parameters	λ	S	C_r	C_t	\bar{C}	Λ_{LE}	$\Lambda_{0.25C}$	$\Lambda_{0.5C}$
Standard	0.80	8.41	0.782	0.625	0.706	1.50	1.12	0.749
10% Increase	0.88	8.41	0.748	0.659	0.704	0.860	0.502	0.143
10% Decrease	0.72	8.41	0.818	0.589	0.710	2.19	1.80	1.41

6.2.2. Effect on Structural Design Wing

Just like the new aspect ratio, a new taper will lead to a different wing box size. When the taper is decreased, the wing box will become larger and hence more efficient in bending. With the 10% taper increase the wing box can once again be optimised and a new total wing box weight of 180kg can be found, while still having the same deflection as the initial wingbox. When the taper is decreased the wing box will be smaller at the tip and needs a larger thickness in order to have a reasonable deflection. The wingbox will therefore have an increase in weight and will weigh 222 kg when the taper is decreased.

6.3. Effect of Increased/Decreased C_{Lmax}

The C_{Lmax} will be increased/decreased by 10%. This will have an effect on the aerodynamics, cruise performance and structural design of the wing. It does not effect control and stability as the slope of the C_L curve remains the same and C_L values for the take-off, landing and cruise do not change.

6.3.1. Effect on Aerodynamics

When C_{Lmax} is taken into account, there are no changes in the wing parameters, the moment curves or the gradient of the lift curve. Therefore, the only thing that changes are the stall angles for each configuration, which increase with increasing C_{Lmax} and decrease with decreasing C_{Lmax} . This can be seen in table 6.7:

Table 6.7: Effect of C_{Lmax} on Lift Characteristics

Lift Characteristics	$C_{Lmax,cruise}$	$\alpha_{s,cruise}$	$\alpha_{s,landing}$	$\alpha_{s,take-off}$	$C_{Lmax,landing}$	$C_{Lmax,take-off}$
Standard	1.30	11.96	9.76	12.59	3.34	2.68
10% Increase	1.43	13.34	10.99	13.86	3.47	2.81
10% Decrease	1.17	10.57	8.53	11.32	3.19	2.55

6.4. Increase/Decrease in Mass

The mass of the aircraft is considered an important parameter, as this influences the design point that follows from the wing loading/power loading diagram. This in turn influences the wing surface area and consequently the values that follow from that. For this analysis the mass will be increased/decreased by 10%. This will have an effect on the performance, horizontal tail size and structural design.

6.4.1. Effect on cruise performance

An increase of 10% in mass will increase the power needed from 122 kW to 130 kW shaft power, which is just 6.6%. The effect is limited because of the high aspect ratio. The Oswald factor hardly changes.

6.4.2. Effect on Takeoff and Landing Distance

An increase in MTOW of 10% would lead to higher speeds for lift-off and touchdown, leading to larger take-off and landing runs. The opposite effect is present for a lower MTOW.

6.4.3. Effect on Aerodynamics

An increase/decrease in weight will result in an increase/ decrease in lift as they are directly proportional. This will in turn increase/decrease drag and pitching moment.

6.4.4. Effect on Structural Design Wing

An increase/decrease in mass will result in larger or smaller forces on the wing. In both cases the current wing will not yield, but the deflection of the wing will either become larger/smaller. When the mass decreases it is possible to optimise the wing even more, leading to a reduction in mass of the wing.

6.4.5. Effect on Horizontal Tail Size

An increase/decrease in mass will result in larger or smaller lift coefficients for the landing, take-off and cruise case. A lower mass and hence a lower C_L value of the aircraft less tail will decrease the slope of the controllability curve, however the slope of the stability curve would remain the same, as a change in mass does not change the lift curve slope, $C_{L,\alpha}$. This would allow the horizontal tail size to decrease, assuming the c.g. range would remain the same.

Operations and Communications

This chapter goes into the operations of the linkage system and the communication between all stakeholders and systems.

7.1. Linkage Operations

In chapter 4 the top two levels of the Function Flow Diagram (FFD) were shown. As already mentioned there, being able to link both Flight Hardware (FH) and Road Hardware (RH) sets this system apart from others. For that reason an in-depth FFD and later Functional Breakdown Structure (FBS) were constructed. A quick recap of function 2.0 second level function were; Receive information, Provide FH attachment, Verify vehicle and Provide fuelling/charging availability. This second step, 2.2 provide FH attachment, is the most important one for linkage operations and for this function there a third level of detail within the FFD was already composed, see fig. 7.1.

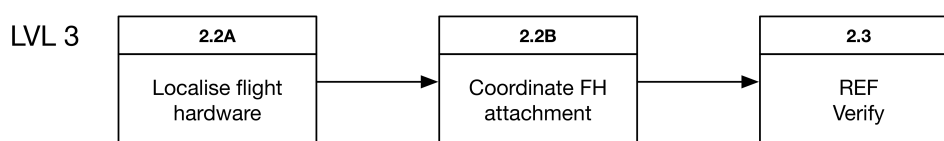


Figure 7.1: Zoom in on level 3 functions of main function 2.0

The "localise FH" function has to do with all the small steps that need to be done before the actual linking. However, after the user has decided to fly, all the required steps are taken to alert all other stakeholders/systems. The FBS, fig. 7.3, shows some of these smaller steps of function 2.2A. The next function, 2.2B "Coordinate FH attachment", discusses the physical interaction of the FH and RH. For this function a further level of detail was constructed, which can be seen in fig. 7.2.

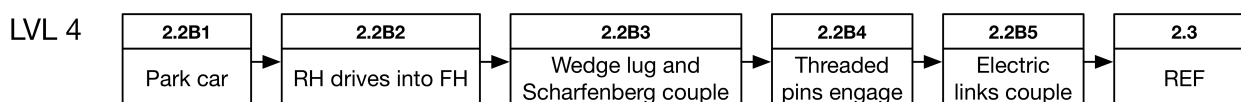


Figure 7.2: Zoom in on level 4 functions of main function 2.0

This detailed level of the FFD finally discusses and explains the linkage operation. The full linking consists of five major functions and at each function there are some further minor steps. All these major and minor functions can be seen and read from both the FFD level 4 (fig. 7.2) and the FBS (fig. 7.3). The linkage operation is undertaken in the following steps. First, the user parks the car in a predetermined space at the airport. Parking is verified and the user exits the vehicle, ensuring user safety and a fully autonomous linking system. At the command of a button the coupling procedure is started. Now the RH drives back into the FH with a tolerance of ± 5 mm.¹ This is similar to automated

¹https://bib.irb.hr/datoteka/816062.warehousing_localization.pdf, (Retrieved on 11 January 2018)

parallel parking of cars. Then the sloped wedge lugs slide into the RH and further self align until the Scharfenberg coupling locks. The combination of wedge lugs and Scharfenberg coupling ensure that the threaded pins and the holes in the lug align as designed for. Now the threaded pins can be turned into place with the help of electric motors. There will be multiple sensors placed to ensure full correct alignment of the pins. Finally, the electric and electronic linkage will couple. This completes the linkage process. After this, an important verification step is performed in order to ensure successful linking of the FH and RH. A full breakdown of all functions related to providing the attachment of the FH can be seen in fig. 7.3. A major requirement that was set for this project was that the attachment of the FH to the RH should be able to happen within 5 minutes. These five level 4 relatively simple functions help insure that this requirement can be met. No manual work is needed, all operation are automatic which also saves time.

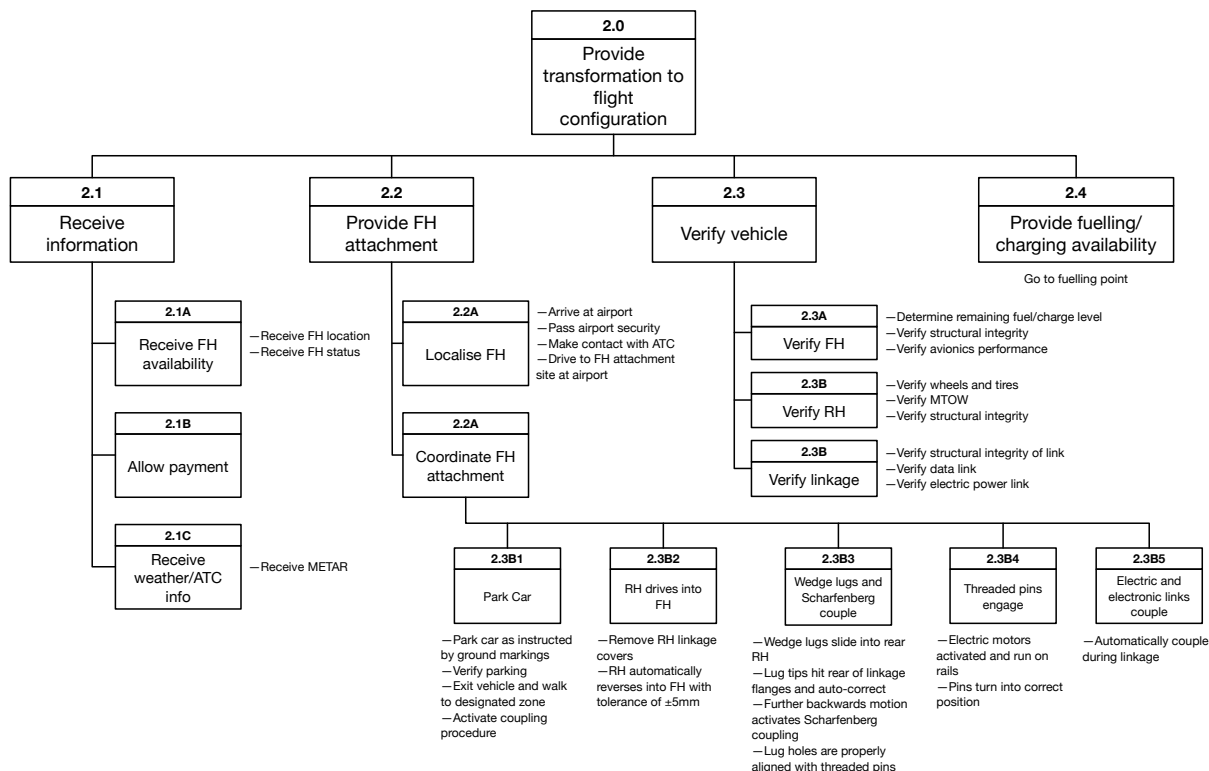


Figure 7.3: FBS of main function 2.0

Considering function 4.0 "Provide transformation to road configuration" a lot of the same lower level functions are used as with function 2.0. Function 4.2 "Coordinate FH detachment" is similar as function 2.2B "Coordinate FH attachment", however all functions are now done in reverse. This entails decoupling of the electric and electronic link and ending with the RH driving away from the FH to a predetermined spot in front of the FH. Using the same functions once again ensures that it can be done fast and autonomously. It also means that one system must be designed so the system can operate in both directions.

7.2. Communication during Operations

A general communication scheme of the operational phase is shown in fig. 7.5. The diagram shows five different systems, namely: the vehicle, flight configuration, road configuration, linkage system and the environment. The user is taken as the central and most important point in the diagram. The diagram generally is self-explanatory. Nevertheless, this section will explain the communication between the vehicle and the environment in more detail.

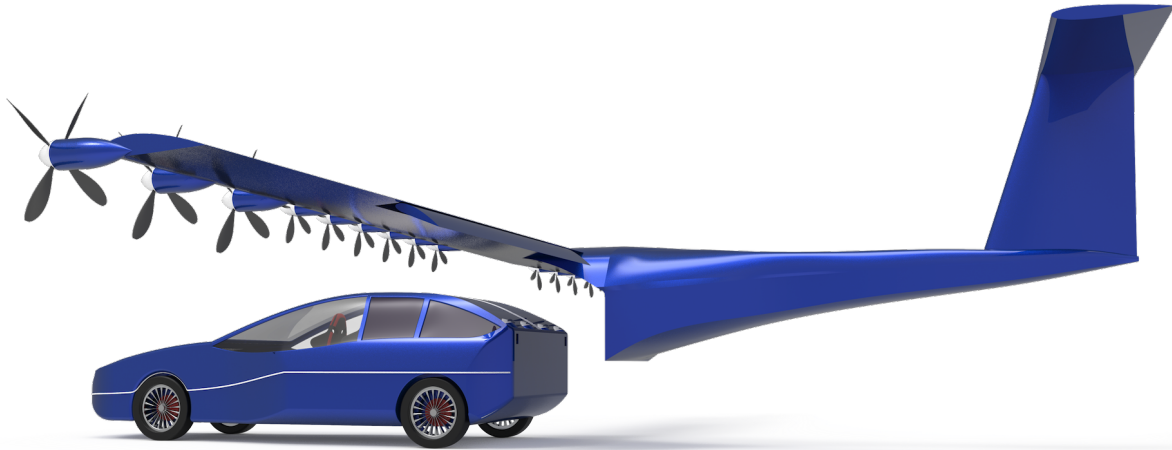


Figure 7.4: Road hardware reversing into flight hardware

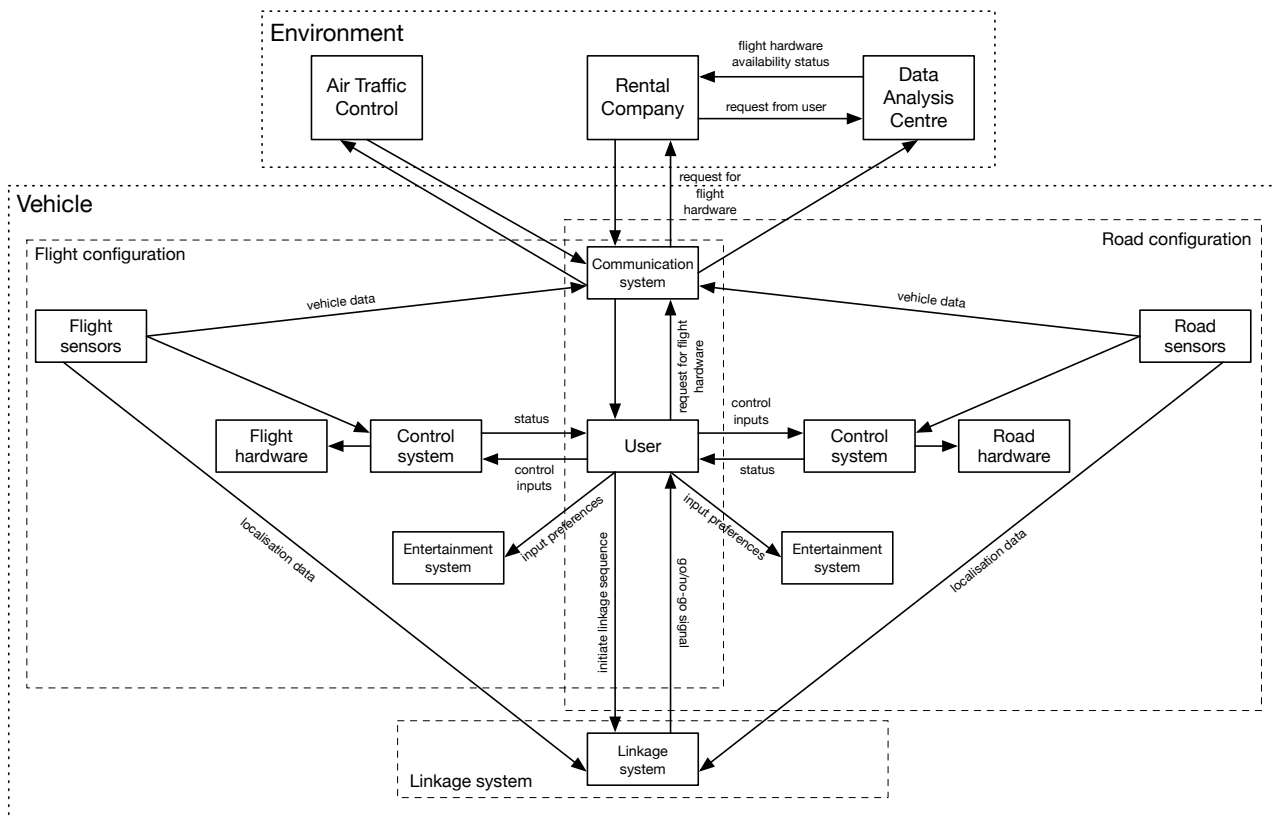


Figure 7.5: Communication system during operations

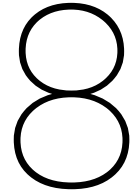
During operation, the vehicle (this system includes the user) communicates with an environment consisting of air

traffic control, the rental company and a data analysis centre. Communication with air traffic control will be similar to general aviation procedures and will be executed through a general aviation radio. Consequently, these communications are of lower interest at this stage of the project and will not be discussed. Communications with the rental company and the data analysis centre are specifically designed for the vehicle and need to be explained.

Communications with the rental company can be done via traditional methods, such as e-mail or telephone. However, a new product like the Chesta I would not be complete without more user focused functionalities. Therefore, Chesta has its own mobile app. More about the app itself is explained in chapter 10, but communications-wise the application is simple. It will be possible to see FH availability at the desired airport, live prices and airport specific logistic procedures are visible through the application. The user can also connect the mobile application to the vehicle's on board tablet, which is integrated in the dashboard. Therefore, one can access the application on a larger screen and reservations can be made/cancelled while sitting in the vehicle. No internet connections have to be installed in the vehicle, since the application is connected with the car via the user's mobile phone and uses the phone's internet connection. As a result, the lines between the communication system and the Rental company are generated by the user's mobile phone. However, once the mobile phone is connected to the vehicle, all actions like calling (hands-free), making a reservation or requesting airport logistic procedures can be done through the vehicle's dashboard.

The lines between the communication system and the data analysis centre are based on the concept of internet of things. The internet of things is a concept where regular devices get equipped with sensors, which share live data with surrounding systems. Nowadays, fleet management systems with live data tracking abilities are more frequently installed in company fleets.² As a result, off the shelf systems can be used and only a small or even no extra R&D budget has to be reserved for such a system. A similar system will be operated by either the producer, the rental company or both. A more elaborate explanation of this division is given in chapter 10.

²<http://keltronitac.org/> (Retrieved on 12 January 2018)



Production Strategy

In order to create a good product, the right production methods must be used. Since the vehicle consists of many small parts, it was chosen to look at the large main components and their connection. The materials have been selected with ease of manufacturing, and sustainability in mind, see section 5.4.1.

8.1. Part Manufacturing

In this section several parts and their manufacturing methods shall be discussed.

Wing

The wing will consist of a wingbox as core, with a cap on one side of the box and a pointy tail on the other side, which together make the airfoil shape. The wingbox itself made from 4 tapered sheets of metal. In order to simplify the production, the taper can be achieved by cutting the wing into 6 different parts of 1m which all have a certain thickness, which is a bit smaller than the one before, resulting in a taper effect. The front and back of the airfoil will be made from sheets of metal which will be formed into the right shape. All sheet deformations that have to be made can be done using hot forming. Moulds for the hot forming will have to be designed in order to achieve the right dimensions, while taking springback into account. The sheets of aluminium will be attached to each other using rivets. (Sinke et al., 2004)

Tail

The tail will be produced in the same way as the wing. The same aluminium is used and hence hot forming and riveting the separate parts together is a good way to produce the tail. Once again, moulds need to be designed to allow the hot forming.

Truss structure

The truss structures will consist of aluminium beams with a constant thickness. These beams can either be bought externally and cut into the right size or can be produced using extrusion. The first option is the cheapest option, and requires the least amount of work. The trusses will be welded together to form one big structure. Since the welding of aluminium is more difficult than the welding of steel a specialist has to be found in order to prevent inaccuracies. (Sinke et al., 2004)

Skin Car

The skin of the car is made of polyester with 30% glass fibre, which is a thermoset. The skin of the car will consist of 1-2 mm of skin with possibly a core in between where necessary. Since the car skin does not need to transfer any major loads (and is not a monocoque) it is not necessary to produce the whole car skin in one piece. The skin will therefore be made of several plates, which can either be glued together or bolted to the trusses, depending on the location of the plates with respect to the trusses. When the plates are bolted to the truss structure hi-loks will be used as they have a better compatibility with composites. The plates can be glued together using flanges, which should be accounted for in the design process. The plates will be made using vacuum infusion. Vacuum infusion is a low cost, short series production method which can produce very large structures. Three to four layers of dry fibres will be stacked on top

of each other. If necessary a core will be added, followed by another three to four layers. The polyester resin will be infused and the plate will be cured. (Sinke et al., 2004)

Skin Flight hardware

The skin of the flight hardware will be manufactured in two pieces. These two pieces will be glued together using flanges, which once again should be accounted for during the design process. It is important that the flanges are on the sides of the flight hardware and not on the top and bottom for structural reasons. The flight hardware will be produced in the same way as the car plates. Vacuum infusion will be used as it is ideal for large structures and core will be added if necessary.

8.2. Assembly

After all the parts of the vehicle have either been bought or produced they have to be assembled. Since car manufacturing and aircraft manufacturing are different branches it was chosen to produce the flight hardware and road hardware separately in order to have the right specialists working on both parts. Figure 8.1 shows the assembly of the car. The truss structure will serve as the base for the assembly and all separate parts will be assembled at different times. First the basics such as the steering system will be added. These can either be welded or bolted to the structure, depending on the material. After that more specific parts will be added such as the electronics and the battery. The skin and closures will be added to the structure using hi-loks and adhesives where necessary and finally the interior will be inserted. (Sinke et al., 2004)

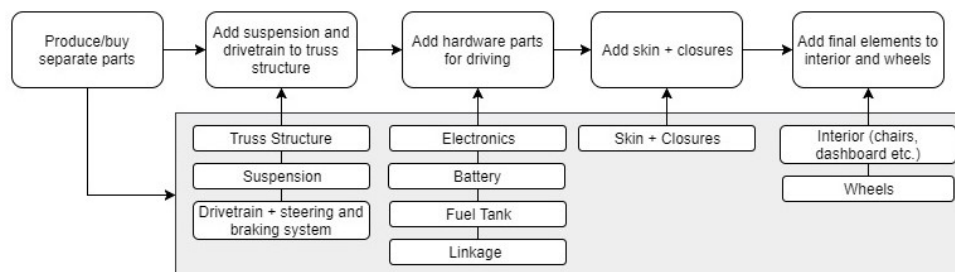


Figure 8.1: Assembly plan car.

Figure 8.2 shows assembly of the flight hardware. The linkage can be welded onto the truss structure since it is made of the same material. After that, the DEP engines plus propellers will be integrated into the wing and at the same time the tail can be assembled. After this, the tail and wing can be added onto the flight structure using bolts and rivets. They cannot be welded together as the truss structure is made from a different aluminium. The electronics can now be added as well and finally the skin can be assembled, functioning as a covering aerodynamic shell.

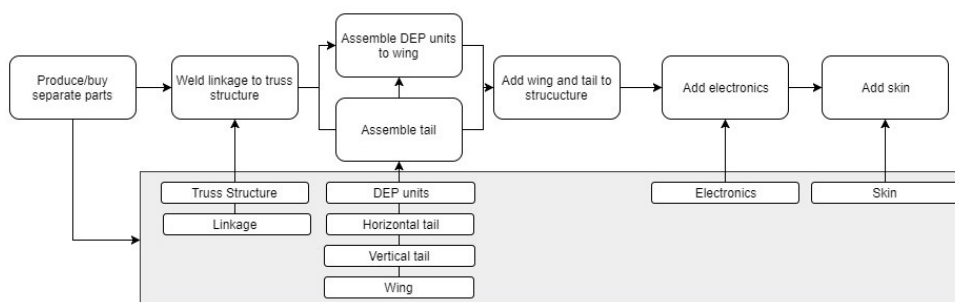


Figure 8.2: Assembly plan aircraft.

8.3. End of Life Cycle and Recycling

In order to have a sustainable design, extra attention is paid to the end of life cycle of the product. Only recycling is considered in this section. The materials used have been chosen with recycling in mind. Eco-cost is utilised to determine the value of recycling. For an overview of the Eco-cost of raw material, see section 9.4. The aluminium alloys can both be melted for use in other applications. In the case of aluminium, only virgin material is used to ensure high

quality. This is not common, since the "market mix" is only 66% virgin material. This complicates the analysis of the recycling credit. There is still debate going on of how to deal with such examples of downcycling. (Vogtländer, 2014) The attributional modelling for the recycling of this material would fall in the category "open loop-different primary route". (JRC, 2010) The complex proposed methods in the LICD book are beyond the scope of this report. In closed loop recycling 100% of the material is used in the same product. The only Eco-cost of a chain would in that case be the cost of recycling itself, production, and of course the use phase. (Vogtländer, 2014) The Idemat database (Vogtländer, 2017) has a list of recycling credit for the closed loop recycling only.

As far as recycling car components goes, special attention shall be paid to EC (2005), which prohibits certain parts from being re-used in the construction of a new vehicle, for example due to safety reasons or wear on exhaust systems. They can not be called reusable, and thus they do not contribute to recycling recovery rates. Part of the skin is a thermoset, and although Edupack¹ mentions downcycling, meaning the material is recycled to lower quality material, no value is attributed to that in this report. Some components in the car, to which no material has been assigned yet, can be made of thermoplasts in the detailed design phase. This ensures better recycling properties. The laminated glass which is used in the car can be recycled. Recycling the electronics will cost a lot of effort and energy. The recycling of lithium batteries is uncertain, however a lot of research is conducted on this topic at the moment. Since many batteries just lose some capacity without failure, they are re-used on a large scale for back-up power of energy grids.

The total return Eco-cost credit can be calculated. E.g. secondary aluminium has 0.25€/kg in Eco-cost. To calculate the recycling credit for aluminium, where virgin aluminium is initially used, the Eco-cost of secondary aluminium is subtracted. By this method the next user "pays" for the recycling process. This is also applied to glass components. The total return Eco-Cost credit, with the method proposed in this report is: 214€, for a total mass of 842 kg. This 842 kg is 71% of the OEW. If the batteries and avionics are recycled, 75% of the OEW is already recyclable, without accounting for the 228 kg that is not yet included in section 9.4. How much of the material can be used in aerospace applications after decommissioning is uncertain; the engine and avionics have been recycled in this consideration.

¹<http://www.grantadesign.com/education/edupack/edupack2017.htm>, 2017 version of database

System Sustainability

In this chapter, the "life cycle design" strategy applied to achieve a Cradle to Cradle design is discussed. The resulting improvement in the impact of flying on bio fuels is discussed in detail. The recycling strategy is discussed in section 8.3.

9.1. Cradle to Cradle, Life Cycle Context

Two major subjects of Cradle to Cradle have been applied into the traditional life-cycle of the product, namely:

- Special attention has been paid to recycling when selecting the materials. The material choices can be found in section 5.4.1 and recycling methods in section 8.3.
- The Biosphere has been incorporated into the design by the use of bio-fuel; the sun will provide the primary energy of the ethanol itself, it only has to be harvested, processed, and transported.

These loops turn the design from cradle to grave to cradle to cradle.

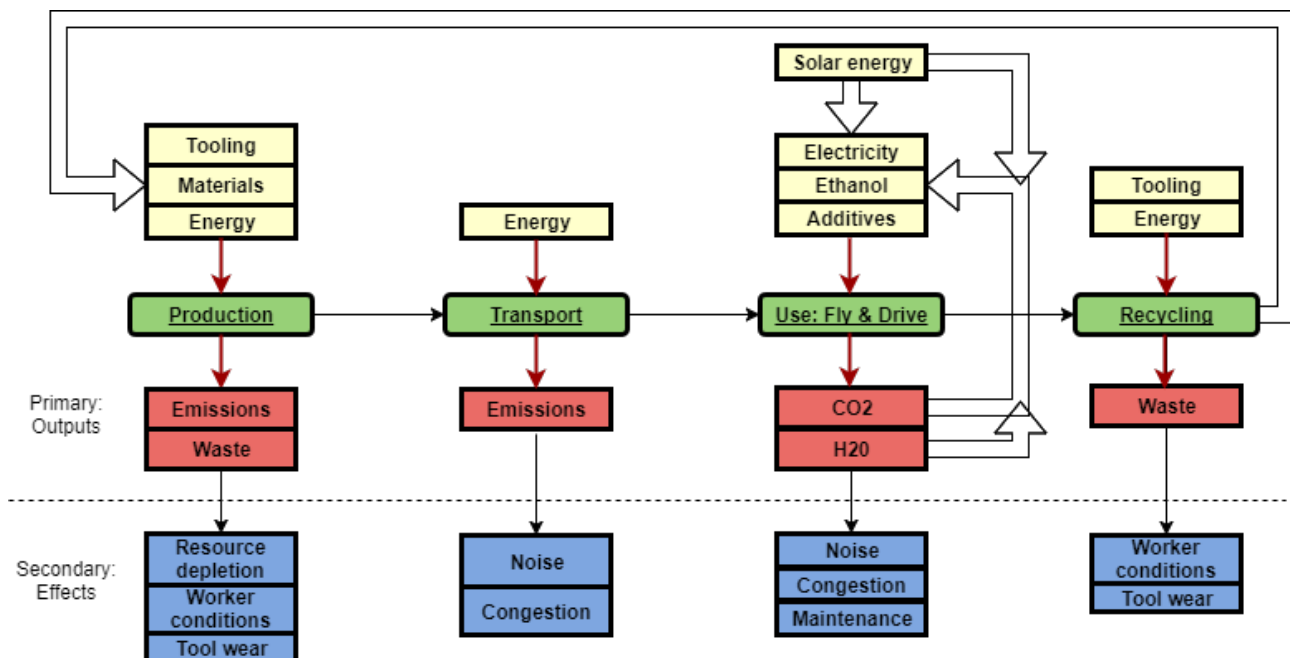


Figure 9.1: The life cycle context of the vehicle. C2C elements marked with a bold arrow.

LCA's have been applied from early on in the design, when choosing materials or fuel. This so called "life cycle design" ensures that there is still room to intervene after conclusions about sustainability are drawn. The environmental impact is evaluated by using Eco-cost from the Idemat database (Vogtländer, 2017). This database includes the impact

from CO₂, material depletion, effect on human health and toxicity. The sustainable strategy wheel, first published by Brezet and van Hemel (1997) has also been used to explore sustainability options. Some elements can be recognised throughout this chapter. It is shown in fig. B.1

9.2. "Well to Wheel" LCA (Fuel Use)

The car fuel is used to charge the battery. Since the Renault Zoe drives 200 km on a 22kWh charge, it is expected 100km on a 10 kWh charge (36MJ) is possible, especially with the low empty mass of our vehicle. The efficiency for charging is 96%. Li-ion batteries have charge efficiencies of up to 99%, so this efficiency is ignored for now. The engine has to provide 10.4 kWh, consuming 3.1 kg of regular fuel, or 3.8 kg of E85. This corresponds to 4.0 and 4.9 L, respectively. This means that the vehicle has a theoretical range of 4000km on E85 ethanol or 5000 on gasoline E10, because of the 200L fuel capacity. For reference, this is the distance from Amsterdam to Moscow, and back. The EcoCost of E10 is calculated by taking 90% of the petrol value and 10% of the E85 value. Including the increased consumption of ethanol, it is still **70% more sustainable than E10 gasoline**.

Bio-Ethanol is often made from sugars or corn, which may compete with farmland used for food production. Some ethanol is made from agricultural waste (cellulose), and much research is underway to make this process more efficient. There is also research into making synthetic ethanol with solar energy. Advantages of using Ethanol for combustion engines is the great anti-knock properties, which enable the use of higher compression ratios and increased combustion timing resulting in more power.

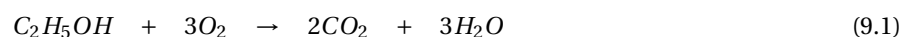
A disadvantage of Ethanol is the lower economy, and the corrosive properties; rubber hoses and some (aluminium) alloys are corroded by ethanol. Ethanol does cause lower cylinder temperatures, which may increase the life of the engine. In E85, the remaining 15% fuel consists of petrol and additives, since pure ethanol is hard to start in cold conditions.

The vehicle is flex-fuel: it will be designed to run on regular gasoline as well. This is much more sustainable than Avgas 100LL, which contains lead as an anti-knocking additive, which is needed in some general aviation ICE's.

Table 9.1: Fuel economy and environmental impact.

	MJ/100km	L/100km	kg/100km	Eco-cost [€]
E10 petrol (road)	157	4.2	3.1	3.77
E85 (road)	99	4.9	3.8	1.13
E10 petrol (combined)	928	24.9	18.3	22.23
E85 (combined)	586	28.8	22.5	6.68
E10 petrol (cruise)	644	17.3	12.7	15.43
E85 (cruise)	399	19.6	15.3	4.54

The CO₂ emissions also have to be calculated. Ethanol has a molar mass of 46, with 2 carbon atoms. CO₂ has a molar mass of 44. This means that for every 46 kg of ethanol, 88 kg of CO₂ is emitted, see eq. (9.1). For road use, this equals around 7.30 kg of CO₂/100km, which is just 73g/km Gasoline releases approximately 3 kg CO₂ per kg.¹ Resulting in around 90g/km.



9.3. Sustainable Business Model

Sustainability is taken into account in the business model. Maximising utilisation of the product really helps to decrease the relative emissions of production. Usual general aviation aircraft spend most of their time on the ground, and are only flown by their owners in the weekend.

Maintenance is performed by the lease organisation, which ensure effective maintenance, preventing issues leading to decreased economy. Expertise and spare parts are always at hand. Flight hardware can be re-manufactured, and receive new components. At the end of the lifetime, the flight hardware can be recycled by means of a special recycling programme. This standardisation leads to quick and efficient recycling process, within a desirable timeframe, with a high recovery rate of precious materials.

¹<https://www.scientificamerican.com/article/experts-weight-ratio-co2-fuel/>, (Retrieved on 23 January 2018)

9.4. Material Choice

The LCAs are performed for a single flight hardware and road hardware, meaning that the Eco-cost per user will be less, if the flight hardware is shared. During the material choice, preference was given to materials with lower Eco-cost for production, and a high return for recycling. Besides cost, one of the reasons not to use CFRP for the main wing was the use of resources during production and poor recycling potential.

Table 9.2: Eco-cost of raw material

	Eco-cost €	kg
Aluminium alloys	871	406.8
FRP's	77.2	68
Glass	13.2	35
Battery	359	30
Drivetrain, chassis	856	400
Avionics	226.9	10
Total	2176	950

Since the OEW is 1178 kg, 25% is added to account for unaccounted materials, which will mainly be found in the interior and car equipment. Afterwards, a 50% contingency is added to account for unaccounted materials with high impact, and the production processes. For aluminium, casting is less than 10% of the material impact. For avionics, the normal impact of 2 desktop computers is used. The total estimate of the production Eco-cost, without recycling credit, is 4080€. Recycling credits are determined in section 8.3.

10

Business Case

Chesta plans to open an entirely new market segment, which will be difficult and challenging. Nevertheless, Chesta believes in a future for personalised air transport and researched the possibilities of making the dream come true. In chapter 2 the existing travel methods and the opportunities for a new personal transportation vehicle were already shown. This chapter will elaborate on the business case that surrounds the aforementioned vehicle concept. First, section 10.1 provides an overview of the company's philosophy and core activities. Then, section 10.2 continues with the flight hardware rental strategy, section 10.3 explains the vehicle's connectivity concept and section 10.4 will conclude this chapter by presenting the financial strategy and profitability of the start-up.

10.1. Company Vision and Strategy

The biggest challenge of a flying car concept will be the implementation of both technical and financial feasibility. This section elaborates on the business strategy. As mentioned in the introduction, it will be launched under the name of Chesta: Car Hybrid Electric Short Take-off Aircraft. The company logo is shown in fig. 10.1.

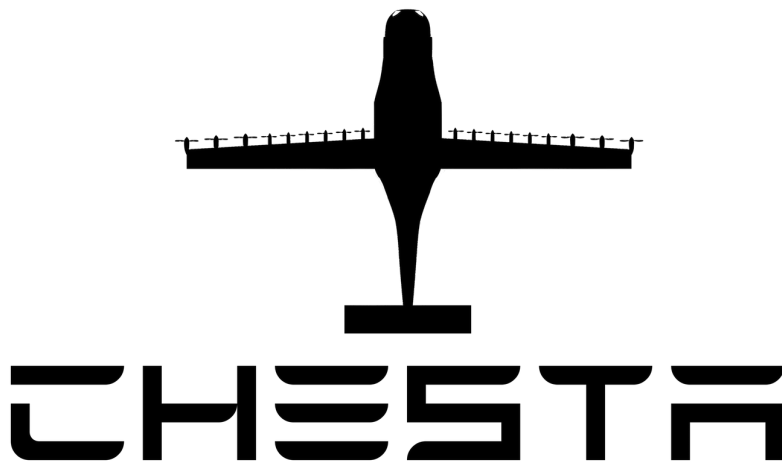


Figure 10.1: Chesta company logo

Chesta believes in personal, fast and comfortable door to door travel within Europe. Therefore, its mission is to develop and produce such a vehicle. It is believed that a hybrid vehicle that possesses both flight and road configurations is the answer. The result is the Chesta I, as described in previous chapters of this report. The Chesta I makes it possible to travel over medium long distances within Europe through the air. Besides the comfort of travelling these distances through the air in a personal vehicle, Chesta also offers maintenance by its own specialised engineers. As a result, the customer can be purely focused on the performance and comfort of the Chesta, without having to worry about maintenance issues.

"It is not easy to be a pioneer - but oh, it is fascinating! I would not trade one moment, even the worst moment, for all the riches in the world. " This quote of Elizabeth Blackwell ¹ embodies the mindset expected by some of Chesta's customers. Chapter 2 already mentioned how companies such as Aeromobil and Pal-V target the adventurous and pioneering urges of the public, whilst also targeting customers acquainted to an exclusive lifestyle who can afford to acquire the entire vehicle (road and flight hardware) and store it themselves. Similarly, Chesta embodies the adventurous and exclusive image through an original production line of more luxurious and customised vehicles. These will be sold at higher prices, with continuation in production allowing the costs per vehicle to be driven down. Unlike the competition, Chesta will target an additional audience other than the wealthy pioneers. The separation of flight and road hardware for optimisation purposes should reduce the product prices, as explained in section 10.4. Consequently, the product becomes economically interesting for companies and successful businessmen. Companies with offices spread throughout Europe could acquire a Chesta I and offer their board a faster, cheaper and more time efficient transportation method to travel between offices. Also, the sustainable, pioneering and stable characters of the company can be positively influenced by the exposure gained from its newest company vehicle. This audience, combined with the successful businessmen within Europe are expected to acquire most vehicles.

So far, only the value propositions and customer segment blocks of the business model canvas shown in fig. 10.2 have been described. This also included the vision of the company and the target audience for the marketing department. Now, customer relationships are considered. Chesta products aim for a high market segment, resulting in a high expected quality of the customers. Consequently, all Chesta's exposure should contribute to an image of quality and trust. Customer relations will be executed on a personal level. Sales personnel focuses on long term relationships with customers in both private and business to business sectors. The business' channels are a result of this strategy. Especially business to business fairs and luxurious lifestyle events offer opportunities and will be used to promote the product and get in touch with customers. For marketing, advertisements could be placed in magazines and a vehicle can be offered to tv (car) shows for reviews and exposure. Revenue streams, so the actual turnover of the company, will be created by the sales of the Chesta I road- and flight hardware and vehicle maintenance.










Key partner  <ul style="list-style-type: none"> Road & air transport authorities Suppliers FH rental companies TU Delft Investors App developer 	Key activities  <ul style="list-style-type: none"> Hardware design & production Marketing & sales Maintain customer relations 	Value Propositions  <ul style="list-style-type: none"> Provide vehicle for personal and fast travel over a range of ~500 km within Europe Provide high-quality maintenance 	Customer relationships  <ul style="list-style-type: none"> Professional on a individual customer level 	Customer segments  <ul style="list-style-type: none"> Companies with main offices spread throughout Europe Successful and adventurous businessmen Riviera lifestyle people for personalised 'toy'
	Key resources  <ul style="list-style-type: none"> Unique product design (patents) Production facilities Specialised service personnel 		Channels  <ul style="list-style-type: none"> B to B & high end lifestyle fairs Sales personnel Marketing through magazines 	
Cost structure  <ul style="list-style-type: none"> Software & hardware development Production cost (raw materials) Marketing & sales Operations (services) after-sales Regulations & research/legal costs 		Revenue Streams  <ul style="list-style-type: none"> Sales RH & FH Maintenance 		

Figure 10.2: Business model canvas of Chesta B.V.

The right side of the Chesta's business model canvas, shown in fig. 10.2 has been described. These blocks are considered the points of contact between the company and its customers/audience. Now, the company structure will

¹<https://elizabethblackwell.weebly.com/education.html>, (Retrieved on 18 January 2018)

be explained, starting with its key activities. First, hardware design & production is required. The result is a working and constantly evolving product, as the high end transportation market requires. Then, marketing and sales have to be professionally executed, as described at the beginning of this section. Finally, the customer relations should be maintained. This could be done by activities such as attending fairs, events or personal contact with a sales person about the user's experiences, feedback and available updates of the system.

Several resources will be absolutely essential and create value for the company. For Chesta, these key resources are its unique product design (patents), production facilities and specialised personnel. The patents result from the development of the Chesta I and may follow from its further updates and research during operations. Possible interest from external companies or applications can facilitate in extra revenue streams into the company. The production facilities are required for the actual assembly of the vehicle. Not all parts will be made by Chesta itself, but final assembly will be one of its core activities. The last crucial resource is personnel. Skilled engineers, well trained salesmen and a maintenance crew with strong connections to the customer will become a valuable asset and should be treated as such.

The main partners can be found in fig. 10.2. A division between three types of partners can be made: regulatory, production & operational and financial partners. Regulatory partners are road and air transport authorities, airports, and governments of various European countries. These partnerships will be necessary in order to make the product flight and road legal. Also, contact between these institutions are essential to stay updated about future regulatory changes. Then, production and operational partners were mentioned. Production partners are companies who design and produce specific parts of the product. Operational partners are the airports, app developers and the rental companies. Close collaboration between these parties should lead to the pleasant user experience Chesta strives for. Finally, financial partners are essential. Without these partners, the product will not be able to be developed and enter the market. So far, the investors have not yet been identified. In fig. 10.2 the Delft University of Technology was mentioned. Chesta finds its roots at this university and maybe an institute, such as YES Delft, might be interested in the idea, and a business will emerge. As a result, the TU Delft is mentioned as a partner.

Finally, the company costs are considered. Main cost drivers are:

- Software and hardware development
- Production costs
- Marketing and Sales
- Operational services and aftersales
- Regulatory research & legal costs

More about the costs can be found in section 10.4.

10.2. Flight Hardware Rental

The Chesta I's separation between flight and road configurations does not only provide opportunities regarding vehicle specifications, but also on the business related to the product. A construction where the FH is offered against an hourly rate of €120/hour was examined. This section explains a business structure for the rental of FH, while section 10.4 explains the prices and profitability of the structure.

Similar to Chesta B.V, a potential business model canvas has been made, which is shown in fig. 10.3. The figure is mostly self explanatory. However, to get a better understanding of the structure between Chesta B.V. and Chesta rentals the key activities, key resources and cost structure will be further explained.

The key activities mentioned in fig. 10.3 are operation of FH, contact between Chesta B.V. and customer contacts. The operation of FH contains everything from storage to scheduling and maintenance of the FH. Some parts of the maintenance will be done by the rental company, while bigger checks and maintenance should be done by specialised Chesta B.V. mechanics. Section 7.2 shows how the rental company communicates with the user.

The Key resources box shows that the rental company is responsible for the spaces on airports. This is done in collaboration with Chesta B.V., since both companies strive to maximal use of the FH for cost benefits. The selection of suitable airports and on site logistics are crucial in this regard. Also, flight hardware is owned by the rental company

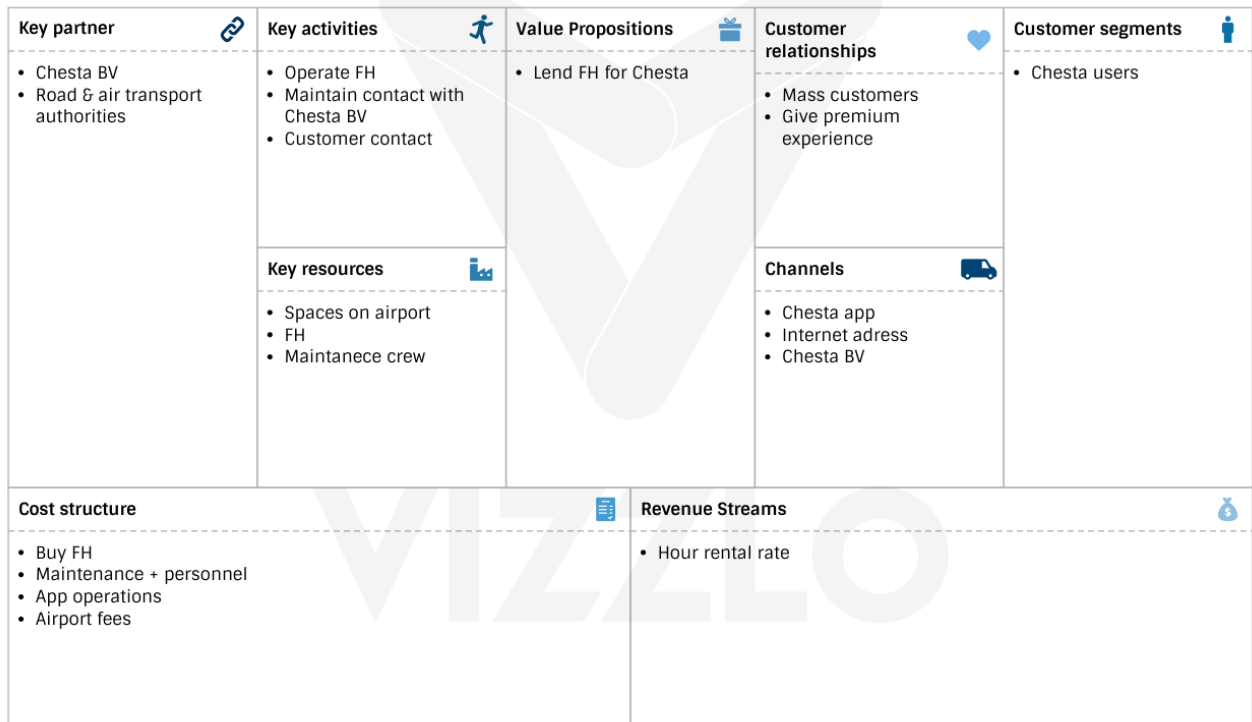


Figure 10.3: Business model canvas of Chesta Rentals

and it is its most important asset. Finally, the personnel available to provide assistance to Chesta I users is an important factor for customer contact and customer satisfaction.

Finally, the costs consists mainly of:

- Flight hardware purchase
- Maintenance and personnel
- Airport fees

Again, the costs will be elaborated on in section 10.4.

10.3. Chesta Vehicle Connectivity

The rental company requires a large investment before operations can start. In order to make the operational costs as low and efficient as possible, the Chesta app combined with the Internet of Things (IoT) applications are implemented. This section explains why these systems are considered and how both users, rental companies and suppliers will benefit from these technologies.

The Chesta app is similar to systems on the market from Volvo² and Tesla³. With the mobile app, the user could activate options such as unlocking the doors, remotely turning on the heater/air-conditioning and see live vehicle data such as available battery power and range. It is mainly a matter of options and should help the user get the premium feeling that the vehicle has to offer.

Implementation of IoT should improve operations of the entire system. Of course, the IoT is closely integrated in the application, but commercial advantages are realised by smart maintenance systems (Molenaar, 2015). The live status data gathered by the data gathering station mentioned in section 7.2 will be useful for both the producer and rental company. Several advantages will be:

²<https://support.volvocars.com/uk/Pages/article.aspx?article=43d4dba8bc6ecf9ec0a80151364bb06a>, (Retrieved on 15 January 2018)

³https://www.tesla.com/nl_NL/support/android-and-iphone-app, (Retrieved on 15 January 2018)

- Efficient preventive maintenance strategy can be implemented.
- FH locations are always known.
- User can use data to improve operations.
- The manufacturer can use data to improve the design and create operational data for the R&D department.

The biggest and driving result of a live data tracking system is the integration of preventive maintenance strategies. In section 10.4 it is mentioned that the costs of FH are high. As a result, the operational time of the FH has to be maximal in order to get the quickest return on investment. The preventive maintenance strategy should decrease FH downtime. Another advantage is achieved through the app. Eventually the app gets data about the operational status of the vehicle and the user's behavior. The application will examine the data to give recommendations about the user's driving/flight behavior. Finally, data gather should provide the manufacturer with valuable data to improve its systems.

10.4. Financial Strategy

Before constructing a more detailed business plan, it is important to consider the overall life-cycle cost of the vehicle. The overall associated costs can only be estimated when considering all cost components throughout the life-cycle of the vehicle. This is necessary in determining a profit scheme.

When considering the overall Life-Cycle of typical aircraft, the following elements are considered:

1. Research, Development, Testing and Evaluation (RDT&E)
2. Production
3. Ground Support Equipment
4. Operations & Maintenance
5. Disposal

When estimating the cost of an aircraft, the RDT&E and Production cycles are often incorporated into single Cost Estimating Relationships (CER). These costs demonstrate some overlap, especially within the areas of engineering and fabrication of testing models. Furthermore, when considering that the flight hardware of the Chesta will typically be sold through distribution centres, it is important to estimate the competitive retail price, typically composed of these two life cycle elements. Initially, this price has been constraint by requirement CoW-Mis-Mar-1.1, as mentioned in chapter 3. However, the product should offer a profitable business case. By initial requirements the sales price is limited to a maximum of €80,000, but from the market presented in chapter 2, it is believed to be acceptable up to €150,000. Regarding costs of other flying cars, which start from €299,000, the vehicle will be the cheapest on the market and the only vehicle with similar specifications (Aeromobil) will cost between 1.2 and 1.5 million euros. Finally, for distribution centres, especially the Operations & Maintenance cost element is important to consider in order to effectively determine the return on investment.

10.4.1. Cost Estimation of the Retail Price

One set of CER for conceptual aircraft design is developed by the RAND Corporation Hess and Romanoff (1987). This particular CER is known as "DAPCA IV", an abbreviation for the Development and Procurement Costs of Aircraft model. Although this particular model is not the most accurate for any particular class of aircraft, it delivers reasonable outputs for a mixture of different types of aircraft. Considering the difficulty of categorising the Chesta into one particular aircraft group, it seems appropriate to estimate the relevant costs using statistical models that represent a large variety of aircraft classes. However, through analysis of both the PAL-V⁴ and Aeromobil⁵, the DAPCA IV relations have been modified to more accurately estimate costs of hybrid vehicles. Using the proposed market prices of the two competitors, similarly to methodology applied in Eastlake and Blackwel (1999), the DAPCA IV relationships were optimised by inversely constructing the cost relationships. The adapted DAPCA IV price approximation is thus altered to portray a relationship between vehicle empty weights (W_E), maximum velocity (V) and proposed production quantity (Q) for the comparable vehicle class of the Chesta. An explanation of cost components included in the calculations will be provided step-wise. The individual elements examined were engineering, tooling, manufacturing, quality control, development support, flight-testing, and manufacturing cost. Next to these costs, the engine and avionics costs are examined individually to determine the final RDT&E and production cost. The following equations, although not modified, are also used within the cost estimation sections of Raymer (1999). Also, similar approaches have been used

⁴<https://www.pal-v.com/>, (Retrieved on 11 January 2018)

⁵<https://www.aeromobil.com/>, (Retrieved on 11 January 2018)

in Roskam (2002).

The engineering hours are considered primarily within the RDT&E budget, but also consider a degree of engineering in the production phase. The hours within this budget are dedicated primarily to the airframe design and analysis, system engineering, test engineering, and configuration control. Also the engine and avionics integration into the vehicle is considered within this cost budget. The actual costs of the engines and avionics, however, will be evaluated separately. Equation eq. (10.1) demonstrates the statistical approximation to determine the engineering labour hours required.

$$H_E = 3.44W_e^{0.777} V^{0.894} Q^{0.163} \quad (10.1)$$

The tooling hours take the typical production preparation into account, and is depicted in eq. (10.2). This, for one, includes the coding of program-assisted manufacturing, preparing molds and dies, designing and producing tools, and creating the necessary equipment needed for testing.

$$H_T = 5.69W_e^{0.777} V^{0.696} Q^{0.263} \quad (10.2)$$

Manufacturing labour considers the immediate hours that go into manufacturing the vehicle. Included within this time estimate are the forming, fastening and machining of parts. Furthermore, the sub and final assembly, routing of electrics, and installation of parts are taken into account when estimating the man-hours required. The following expression approximates the hours of labour required for the manufacturing phase:

$$H_M = 7.12W_e^{0.82} V^{0.484} Q^{0.641} \quad (10.3)$$

The quality control is correlated to the manufacturing man-hour budget, as depicted in eq. (10.4). It primarily considers the inspection, both production and final, of the vehicle sub-assembly and final assembly.

$$H_Q = 0.133H_M \quad (10.4)$$

The aforementioned equations all estimate the hourly labour time for specific tasks of the RDT&E and production life-cycle stages. In order to calculate the appropriate labour costs, the estimated hours must be multiplied by appropriate hourly rates. These rates will be referred to as "wrap rates", as the rates include employee benefits, overhead, and administrative costs (Raymer, 1999), as well as the employee salaries. Typically, the wrap rates are approximately twice the hourly salary rate of an employee. Therefore, using above average Dutch mechanical engineering salaries of €30.00 per hour⁶, and appropriately scaling these salaries according to the labour tasks, the following wages were considered:

1. $R_E = €60$
2. $R_T = €61.4$
3. $R_M = €50.93$
4. $R_{QC} = €56.51$

The individual cost components, besides the man-hour estimations, introduced in the model are costs for development support, flight-testing, and material costs for manufacturing. Development support costs, C_D considers the non-recurring costs of supporting the RDT&E phase. This includes components such as test articles, testing items, sub-system simulators, and creating of mock-ups. The flight-testing costs, (C_F), consider all required actions necessary to confirm the airworthiness of the vehicle for certification. The costs will include the production of testing vehicles, of which three are predicted to be fabricated for the Chesta. Furthermore, costs of flight-test planning, instrumentation, operations, data handling and control, and engineering support are all considered as well. Lastly, the cost estimation regarding the manufacturing materials, C_M , considers all structural raw materials, purchased hardware, and wiring of electrical systems. These three cost estimations are approximated by the following three relationships:

- $C_D = 66.0W_e^{0.630} V^{1.3}$
- $C_F = 1807.1W_e^{0.325} V^{0.822} FTA^{1.21}$
- $C_M = 16W_e^{0.921} V^{0.621} Q^{0.799}$

⁶https://www.payscale.com/research/NL/Job=Mechanical_Engineer/Salary, (Retrieved on 22 January 2018)

Furthermore, the cost estimation excludes the costs for the engine and the avionics system within the Chesta. For the engine, a ROTAX 915 IS/ISC⁷ was considered at this stage, priced at approximately €31,707. However, due to the fact that the Chesta engine requires a slightly higher power than the current ROTAX engine produces, the price is multiplied by a factor of 1.2 to accommodate for upward scaling of the engine. Therefore, the resultant engine cost will be €38,050. It is relevant to mention, however, that with the passing of time, innovation within development of the engines and avionics systems will increase. Therefore, these costs reflect current approximations, which will depreciate with future innovation. The avionics subsystem, at this stage, that was considered was the Garmin500, priced at €13,116.

Therefore, taking all components of the modified DAPCA IV model into consideration, the following cost estimation is presented for the Research, Development, Testing, and Engineering and Production stage of the Chesta. The values underneath are based on a production quantity of 100 vehicles, based on market volume PAL-V proposed to bring to the market.

Table 10.1: Modified DAPCA IV Cost Estimation Relationship for a Production Quantity of 100

Cost Element	Cost (Million Euros)
Engineering Man-hours	5.797
Tooling Man-hours	6.444
Manufacturing Man-hours	24.809
Quality Control Man-hours	3.661
Development Support	1.290
Flight Testing	1.215
Manufacturing Materials	9.284
Engine	3.805
Avionics	1.312
Total Cost	79.685

If a production quantity of 100 vehicles is proposed, the costs of a single vehicle is estimated at €796,850. With a proposed profit margin of 15%, the retail price of the complete Chesta (Road and Flight hardware) will equal approximately €910,000. As proposed within section 10.4, the road hardware would be available for purchase, separately, at a cost of €150,000. This result in the flight hardware selling for €760,000.

10.4.2. Accumulated Financial Impact on Customer

For the customer, two options exist. First, and originally proposed, is purchasing the road hardware for approximately €150,000, and making use of flight hardware rental options. The rental costs were at a prior design stage estimated to equal €120 per flight hour, which would cover costs such as maintenance, logistic costs and personnel. The fuel costs of the Chesta, predicted to equal €73.90 per flight hour, would not be included in this rental fee. Therefore, with the purchase of the road hardware at €150,000, the costs per flight hour would equal €193.90 when profiting from rental options.

The second option that exists is purchasing the Chesta in its entirety, both road and flight hardware. This will cost the customer €910,000 in purchasing costs. With accumulating cost of €73.90 hours and a maintenance estimation cost of €25.47 per flight hour. This maintenance cost was approximated using the predicted Maintenance Man hours per Flight Hour (MMH/FH). According to Raymer (1999), for light aircraft the MMH/FH can be approximated as 0.25. Using the wrap manufacturing rates presented in section 10.4.1, the labour costs for maintenance per flight hour are approximated. The material costs are considered equal to the maintenance costs, resulting in total maintenance costs of €25.47 per flight hour. Additionally, the customer must consider logistic costs with regards to storing the flight hardware and having access to mounting apparatus. At this stage, these costs can not yet be accurately established. In future analysis, these costs should be more thoroughly analysed and discussed with airports in order to provide a cost analysis of increased detail.

The two customer options are plotted against the accumulating cost estimate of competitive companies, the PAL-V and Aeromobil. These are assumed to experience similar maintenance costs as the Chesta, and will experience fuel costs of €117.88 and €72.54 per flight hour, respectively. The cost regression is depicted in fig. 10.4, assuming that

⁷<https://www.flyrotax.com/produkte/detail/rotax-915-is-isc.html>, (Retrieved on 22 January 2018)

the customer flies 8 hours per week on average. Furthermore, an inflation of 2% is taken into account to accurately account for changes in prices of maintenance and fuel.

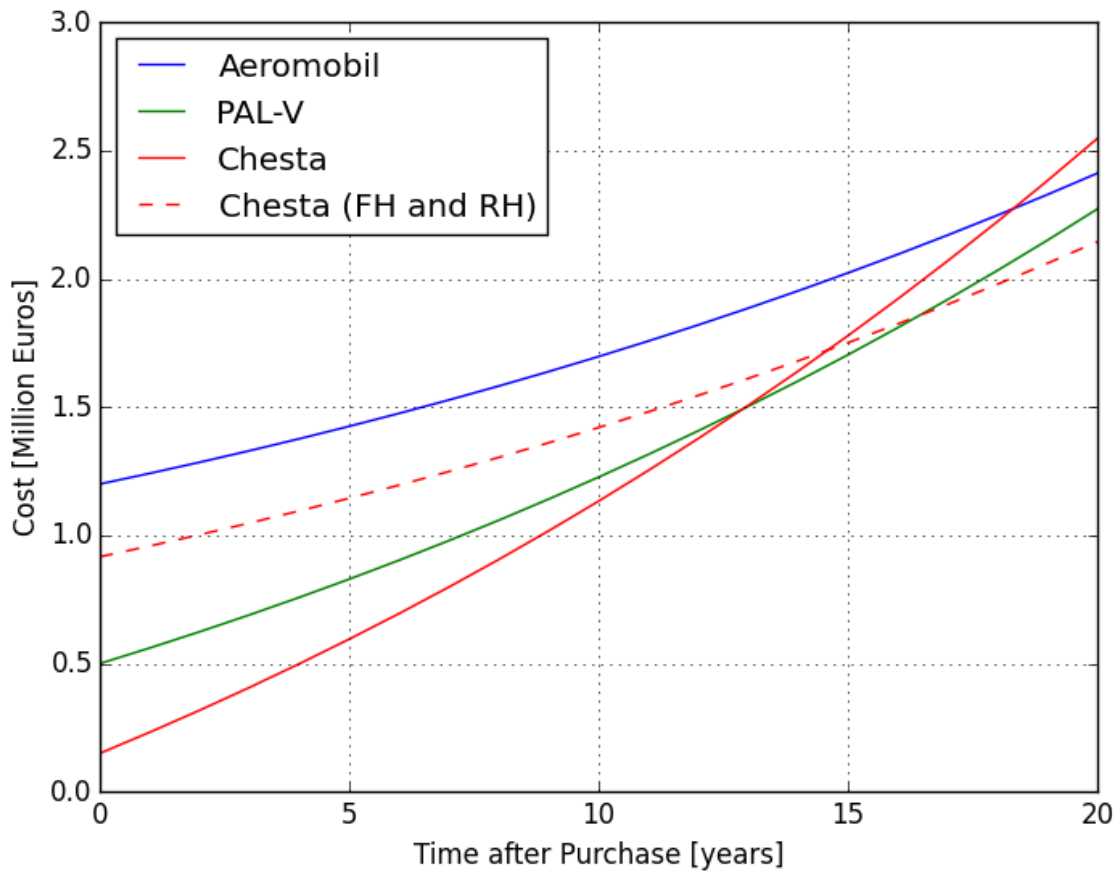


Figure 10.4: Customer Cost Comparison with Average Usage of 4 Flight-hours/Week

By only examining short term investment, it is clear that purchasing the Chesta road hardware, whilst renting flight hardware, is the most optimal solution. Under the current cost analysis, however, the Chesta will become more expensive overall than the PAL-V after 12.89 years, at a total accumulated cost of 1.493 Million Euros. Furthermore, the Chesta will also become more expensive than the Aeromobil after 18.32 years, at a total accumulated cost of 2.273 Million Euros. Once again, however, this is not entirely accurate, as logistic costs of actually owning the flight vehicle are underestimated. If the customer tends to fly less on a weekly basis, the Chesta with rented FH becomes more and more cost efficient with respect to its competitors. It's major additional cost drivers exist in the €120 per flight hour; reducing this on a regular basis will thus reduce accumulated cost over time.

10.4.3. Break-even Analysis and Future Considerations

For the Chesta company, a profit margin of 15% is considered when constructing the retailing price of €910,000 euros. If the flight configuration is not sold through external distribution centres, the return of investment must be considered with Chesta supplying rental flight hardware. This entails that Chesta will charge €120 per flight hour purely for rental costs, but will be responsible for maintenance. With the current proposed production quantity of 100 vehicles, and assuming that a set of flight hardware can be let for 8 hours on average per week, the break-even time is calculated to equal 16.3 years. After this point, all further transactions will be resulting in overall profit. Therefore, from a business perspective and with the current proposed inputs, it would be ideal to increase the rental cost. With a 20% increase, the time required to break-even decreases by approximately 22.8% to 12.6 years, for example. From a business and cash flow perspective selling the entire product immediately against the 15% profit margin would be better. Therefore, the rental company of section 10.1 is proposed. For further research it is recommended to contact existing rental com-

panies available on airports, such as Hertz, Avis, Sixt and propose the business case of renting Chesta-I flight hardware.

It is important to evaluate the outcomes and state future considerations. First off, logistic costs have not been considered in the break-even analysis, with the exception of maintenance cost estimations. In a more extensive cost and break-even analysis, the costs of attachment equipment, storage, and personnel have to be considered. This will inevitably increase the operational costs of the Chesta. Secondly, a ratio of 1:1 has currently been considered for road and flight hardware. This could be optimised by increasing the ratio of road hardware components in comparison to flight hardware. Within distribution centres, flight hardware can be more efficiently distributed, optimising the return of investment per flight hardware set. Through analysis of typical distribution centre rental rates and frequency, a more optimal ratio would be proposed. Lastly, by increasing overall production quantity, the price of individual vehicles will decrease. This is due to the learning capability throughout the production processes. With more vehicles produced, the manufacturer will learn from experience and be able to produce the next vehicles more efficiently, and thus cheaper.

Technical Risk Assessment

The risks that may occur during the next phase of the design and development phase of the vehicle are discussed in this chapter. The identified risks with the probability and impact on performance, schedule and costs are described. In order to manage the risks and to achieve the required performance of the vehicle, mitigations are described for each risk. Risk maps will present the overview of the result of the mitigation.

Most of the calculations were done based on many assumptions which can lead to results that deviate a lot from future test results or reality. In some cases the assumptions had to be done because research on a particular part has not been done yet or not enough data being present. In other cases the assumptions were done due to the preliminary phase of the project and time constraint. Furthermore, this vehicle consists of components which have never been applied in aviation and have more uncertainties and a higher risk of not meeting the requirements. Hence, these calculated and estimated parts of the vehicle have risks of which the probability of occurrence is based on how simplified the calculations are and how much is known about the technology.

The probability of occurrence of these risks is categorised as: rare, unlikely, possible, likely and almost certain. The impact these risks can have on the schedule, costs and vehicle performance is categorised as follows:

- Catastrophic: Mission failure or significant non-achievement of performance
- Critical: Mission success is questionable or some reduction in technical performance
- Marginal: Degradation of secondary or small reduction in technical performance
- Negligible: Inconvenience or non operational-impact

There might be cases where the risk cannot be mitigated or is chosen not to be mitigated because mitigation in these certain cases will lead to even more delay of delivering the product and/or higher costs. In this case the issue has to be accepted and the user's manual might need adjustment.

A clear overview of the risks with the corresponding probability, impact and the way to mitigate is presented in fig. 11.1. The risk map gives a better overview of the impact and probability of the risks. In the upper right corner are the risks with high probability and high impact. These risks are moved to the left and/or down after mitigation as shown in fig. 11.2.

#	Risk	Probability	Impact	Mitigation
1	Short-circuit of electrical cables due to overheating	possible	catastrophic	Evaluate isolation material of cables
2	Electrical engines difficult to manufacture	likely	catastrophic	Start manufacturing at an early stage, have a realistic alternative.
3	Propeller blade detaching in test phase	unlikely	catastrophic	Excessive quality control during manufacturing
4	Certification of DEP is extended over longer time duration	likely	critical	Start application for certification immediately
5	Drag of car during (windtunnel) test turns out to be much larger than assumed	possible	critical	Detailed Computational Fluid Dynamics analysis to estimate the overall design drag
6	Vortex of propellers large effect on wing	possible	marginal	Detailed Computational Fluid Dynamics analysis
7	Inconvenient assumption of induced Delta_Ci due to DEP propellers	unlikely	critical	Choose a different airfoil, detailed Computational Fluid Dynamics simulation
8	Passenger positions have a larger effect on centre of gravity than calculated	unlikely	marginal	Adjust centre of gravity by adding weight at a convenient location
9	Estimated centre of gravity location during the design phase deviates from test results significantly	unlikely	critical	More comprehensive centre of gravity calculations, CATIA modelling
10	Test results show static and dynamic instability	unlikely	critical	Use exact numbers for calculations/not too many assumptions, computational modelling of vehicle
11	Not being able to fabricate the proposed electric coupling linkage	possible	catastrophic	Have a realistic alternative design option
12	Linkage unable to carry ultimate loads	unlikely	catastrophic	Design for ultimate loads and redundancy with a safety factor, structural tests
13	High wing eigenfrequency	unlikely	critical	Design for low eigenfrequencies using the right material and dimensions for a stiffer design
14	Control's, power subpart do not fit inside the wingbox	likely	critical	Take all dimensions of subparts into account during wingbox design
15	Too large wing tip deflection	likely	critical	Choose stiff material, optimize number of stringers and spars
16	Certification of train coupling for aviation takes more time	possible	critical	Start application for certification immediately

Figure 11.1: Overview of Risk, Corresponding Probability, Impact, and Mitigation

		Risk Map before mitigation						Risk Map after mitigation			
		Impact						Impact			
Probability		Negligible	Marginal	Critical	Catastrophic	Probability		Negligible	Marginal	Critical	Catastrophic
Almost Certain						Almost Certain					
Likely				4, 14, 15	2	Likely					
Possible		6		5, 16	1, 11	Possible		16		11	
Unlikely			8	7, 9, 10, 13	3, 12	Unlikely		6, 7, 12, 13, 15		1, 4, 5, 14	2
Rare						Rare		8		9, 10	3

Figure 11.2: Risk Maps before and after Mitigation

Verification and Certification of the Product

Verification of the product is necessary to be able to prove to the customer and airworthiness authorities that the design satisfies the requirements the vehicle had to perform and satisfy the airworthiness regulations. In order to receive a type certificate from the airworthiness requirement, a proof of compliance has to be made which needs to be verified by a verification engineer. This section discusses the compliance proving methods, after which a table summarizes which compliance proving method will be used to verify a requirement, after which the type of tests that will be performed on Distributed Electrical Propulsion (DEP) and Linkage will be discussed in a bit more detail.

The compliance proving methods used for aircraft are listed below:

- Test, type of verification that requires instrumentation
- Analysis
- Simulation, analysis with the use of computers
- Demonstration, type of verification that does not require instrumentation
- Examination, visual inspection

Table 12.1 shows the requirement and the compliance method that will be used to verify if the requirement has been satisfied.

There are two innovative aspects to our design, namely the linkage of the flight hardware and distributed electrical propulsion (DEP). The goal is to have this aircraft certified under a single engine Private Pilot License, the reasoning on how this can be achieved is explained. After that some of the major tests that need to be performed for the DEP and the linkage are discussed.

The major tests that are envisioned in order to get DEP certified under a single-engine Private Pilot License are discussed. First of all, the chance of failure of one engine needs to be analysed and this probability should be below a certain value. Furthermore, as was explained in section 5.1, the aircraft is able to maintain its altitude with four engines operative instead of six engines. This should be analysed in further detail and full scale engine tests should be performed to validate the analysis. If this is validated, the possible event of an engine failure of one of the six engines in cruise would not result in an asymmetric thrust situation as the corresponding engine on the other side can be shut down. The best way to do this, is without a required pilot input, hence a system that assesses the thrust and automatically shuts down the corresponding engine in case of an engine failure should be developed and certified. Moreover, in the possible event of more engines failing on one side, the small DEP propellers that are normally used for landing and take-off can be switched on to create symmetric thrust. This needs to be analysed in more detail and validated by full scale tests, in a similar test setup as NASA's LEAPTECH. (Stoll et al., 2015). These tests should validate that the likelihood of an asymmetric thrust situation occurring is almost non-existent, such that the aircraft can be licensed under a single-engine rating.

Next to this, a full scale test with a similar test setup as NASA's LEAPTECH (Stoll et al., 2015) needs to be performed in order to analyse the effect of a broken propeller blade on the functionality of the other propellers. In this way it can be seen if this event sets in motion a domino effect that would ruin the functionality of the wing. These tests can then be used to re-iterate the design and make changes such as increasing the propeller pitch and/or leading edge sweep.

Table 12.1: Requirement Verification Method

Requirement	Verification Method	Requirement	Verification Method
CoW-Sys-Tech-1.1	Examination	CoW-Mis-Sus-1.Car	Simulation and test
CoW-Sys-Tech-1.2	Demonstration	CoW-Mis-Sus-1.Air	Simulation and test
CoW-Sys-Tech-1.3	Test	CoW-Mis-Sus-2.Car.0	Test
CoW-Sys-Tech-1.4	Demonstration	CoW-Mis-Sus-3.Car	Simulation and test
CoW-Sys-Tech-2.1	Examination	CoW-Mis-Sus-3.Air	Simulation and test
CoW-Sys-Tech-3.1	Analysis	CoW-Mis-Sus-4.1.1	Analysis
CoW-Sys-Tech-3.2	Demonstration	CoW-Mis-Sus-4.1.2	Analysis
CoW-Sys-Tech-3.3	Demonstration	CoW-Mis-Sus-4.1.3	Analysis
CoW-Sys-Tech-3.4.0,3.4.1	Demonstration	CoW-Mis-Sus-4.1.4	Examination
CoW-Sys-Tech-3.5.0,3.5.1	Test and Demonstration	CoW-Mis-Sus-4.1.5	Demonstration
CoW-Sys-Tech-3.5.2	Test and Demonstration	CoW-Mis-Sus-5.1	Analysis
CoW-Sys-Car-2.1	Test	CoW-Mis-Sus-5.2.Car	Analysis
CoW-Sys-Car-2.2	Test	CoW-Mis-Sus-5.2.Air	Analysis
CoW-Sys-Car-3.1	Examination		
CoW-Sys-Car-3.2	Demonstration	CoW-Mis-Mar-1.1	Analysis
CoW-Sys-Car-3.3	Demonstration	CoW-Mis-Mar-1.2	Analysis
CoW-Sys-Car-4.1	Demonstration	CoW-Mis-Mar-2.1	Analysis
CoW-Sys-Air-1.1	Simulation, analysis and test	CoW-Mis-Mar-2.2	Simulation
CoW-Sys-Air-2.1	Simulation and test	CoW-Mis-Mar-2.3	Simulation
CoW-Sys-Air-2.2	Simulation and test	CoW-Mis-Mar-2.4	Analysis
CoW-Sys-Air-2.3	Simulation and test		
CoW-Sys-Air-2.4	Simulation and test		
CoW-Sys-Air-3.2	Demonstration		
CoW-Sys-Air-3.3	Demonstration		
CoW-Sys-Air-3.4	Demonstration		

This is therefore a development test, however once the design is iterated another similar test has to be performed to validate the final product.

Moreover, as a total of nine engines present on each wing, a lot of high voltage electrical cables run through the wing box to all these engines. A test should be performed to determine the effect a short-circuit in one of the cables has on the other cables and hence the engines.

The linkage system consists of a mechanical part and an electrical part.

A failure test should be done on the mechanical part of the linkage in full scale. Normal and shear loads should be applied on the linkage until failure. With the road hardware being floor fixed the linkage should withstand the ultimate flight loads described in section 5.4.3. To test for redundancy failure load testing for the individual link/connecting point should be done. Even with one individual link/connecting point, the linkage system should still be able to withstand the ultimate flight load cases as well. The test results should conclude if the linkage will be able to carry the ultimate loads. With negative test results the design should be modified in order to withstand these loads after which it should be tested again and validated.

The idea/design of the electrical part of the linkage is based on train technology namely the train coupling system. This system is already designed, used and certified for train technology purposes, but not for aviation purpose. The design and certification of this coupling system will be outsourced.

The linkage is designed such that the flight hardware and the road hardware can be attached and detached within five minutes. To test and validate this operation a prototype of the vehicle will be used to measure the time and safety of this operation.

Further Research and Recommendations

In this chapter, recommendations are given for further research, and the planning of post-DSE activities is presented as well.

The current mass of the aircraft is 66 kg over the budget of 1600 kg. Advancements in Electronics, and improved structural design and materials are expected to shave off these 66 kg during the design phase. Another option would be to limit the range of the aircraft when it's flying on Ethanol, since this fuel is heavier. Improved accuracy of the LCA is also a point of concern.

13.1. Performance and Propulsion

Within the performance and propulsion section, particular uncertainties were still identified. These were primarily within the areas of DEP, the drive-train power density (especially the battery), engine certification, and landing performance. For DEP, it is recommended to conduct physical testing at low-speeds. This will establish clear results of DEP on the impact of thrust, drag, and lift. Especially with induced ground effect acting on the vehicle, this analysis will be useful. It is suggested that flaps with more drag than Fowler flaps are used to negate the effect of thrust by DEP. Some simple speed brakes were already assumed, but different pilot technique or other aerodynamic means should be investigated. This could perhaps entail different pilot techniques, control augmentation, or spoilers. Lastly, the discharge rate of the battery requires more investigation in order to optimise the drive-train power density. The fuel consumption has to be estimated more precisely by re-evaluating L/D ratio and engine specific fuel consumption. The fuel economy can be improved by flying slower or higher, since the highest L/D occurs at higher values of CL. This would require some sort of oxygen supply to fly above 8000 ft for extended periods of time, or simply a lower cruising speed.

13.2. Aerodynamics

Many assumptions were made due to uncertainties, in particular the effects of DEP on the lift curve and the non-linear effects at high angles of attack. First, the airfoil must be evaluated more precisely. Through considering the desired pressure distributions along the airfoil, the airfoil geometry can be computationally constructed through an inversely iterative process. Second, before manufacturing of the wing will start, the clean wing should be modelled more extensively. Through 3-Dimensional Computational Fluid Dynamics simulations, the fluid flow along the wing can be visualised and analysed more objectively. The effect of DEP, wing/propeller tip vortices, component drag estimation, and wing/fuselage interference can then be analysed and sizing can be performed accordingly. After CFD analysis, it is recommended to perform wind tunnel testing on the clean wing. This is essential in order to determine the relationship between the lift and angle of attack when the flow along the planform starts to separate. It is also recommended to perform static and dynamic testing of the wing with DEP. With testing, the effects of DEP on the wing's aerodynamic capabilities will be understood in more detail, allowing appropriate alterations in design and sizing if deemed necessary.

13.3. Stability and Control

During further research more detailed weight estimations of component should be used to optimize the c.g. range even more. The packaging of the car and hence the c.g. range was selected in such a way that the tail would have an

acceptable size. This however creates a fairly aft c.g. of the car during operations. Further research can be done on improving the car handling.

Semi-empirical relationships present in Torenbeek (1982) were mostly used in the analysis of longitudinal stability and control. It is recommended to perform a detailed analysis of the effects on DEP on these semi-empirical relations and to verify if DEP can be properly modelled in this way. Furthermore, the assumptions made in this analysis should be re-evaluated and the effects of thrust, drag and aeroelasticity should be taken into account for more accurate results. Moreover, the stick-free stability and minimum stick-force per loading factor should be analysed as well as the eigenmotions of the aircraft. Furthermore, an autopilot system can be analysed in further research.

13.4. Vehicle Structures

Since the wing has been simplified in the calculations, a lot of further research can still be done. First of all the wing box should be designed in more detail. The sheets should be checked for buckling in order to add webs and stringers to the box at the right places. Using the detailed design it is also advised to make a FEM(finite element method)-model both of the wing plus its skin and the skin of the vehicle to make a more accurate estimation of skin thicknesses and stress occurrences. The skin material choice might be reevaluated if it turns out to be too weak. Furthermore, it is advised to analyse the loads on the wing that have been neglected in this report, such as thrust and drag. Further research should also be done on the effect of aeroelasticity and the flutter of the wing. Once the design has been finished it is advised to have a full scale wing test and test the skin on impact forces.

The Flight Hardware (FH) truss structure was currently designed using many assumptions. For further research and design many of these simplification assumptions must be omitted. Furthermore, dynamic loads and vibrations must be included in the design of the FH structure. Another important consideration is analysing other failure modes. Considering ultimate failure was predicted due to buckling, failure due to bending, torsion and shear were not analysed as excessively. To help combat these failure modes, a load carrying skin was incorporated. This will lead the FH structure design towards a more traditional semi-monocoque design similar to other aircraft. Lastly, through deciding on new linkage points, the FH structure might be made stronger and lighter.

For the truss structure of the car many assumptions were made. In the next phase of the vehicle design, the thin sheet plates should be taken into account with shear loads acting through the plates. Considering the front glass shield will carry shear loads, the analysis of the glass shield should be taken into account as well. Furthermore, the calculations of the car cabin truss structures was beyond the scope of the preliminary design phase of this project. Due to the two big door holes and the desire to keep the aerodynamic shape of the vehicle, calculating the exact load transfer is difficult to model. The estimation of the beam area sizes should be tested on the ultimate tensile, compression and buckling load cases and should be adjusted based on the test results.

The possibility of a monocoque as a passenger cabin should be investigated and tested on ultimate loads in flight configuration. Nowadays monocoque are used in sports cars but are designed such that the driver does not get crushed during crash. Variations in design and purpose should, thus, be examined and optimised. Furthermore, for the next phase of the design, it is recommended to take all weights of all sub components into account for the design of the car.

13.5. Linkage Design

Both the the Scharfenberg coupling and electric/electronic coupling have been adapted from the train infrastructure. As mentioned before, these parts have never been designed and used for an aerospace application. A further research into the adaptability and integration of these parts should be done. If major problems arise, a potential totally new linkage system must be thought of. Furthermore, the design of the linkage lugs size and location has to be improved. Currently, the lugs are still over-designed. Smaller lugs are thus still possible. Decreasing the size will help a lot with packaging. This in turn can help with linkage locations on the RH. Which will in its turn can have positive effects on the structural design. Lastly, further design of the operations and logistics should be done to help refine the functions and create better detailed steps. It is also wise to set-up an user-manual on how to operate the linkage procedure.

13.6. Project Design & Development Logic

In order to make an estimation of the overall progress, and to reserve resources for further project development, the post-DSE activities need to be identified.

The diagram can be found in fig. 13.1 The diagram has been divided into three levels, many activities are conducted simultaneously, following the philosophy of concurrent engineering, the diagram shows similarities to Airbus. (Pardessus, 2004, Smyth, 2006) The three levels Aircraft, Production, Support are developed simultaneously. The time frames have been estimated, the total development to the start of production is estimated to take 7 years.

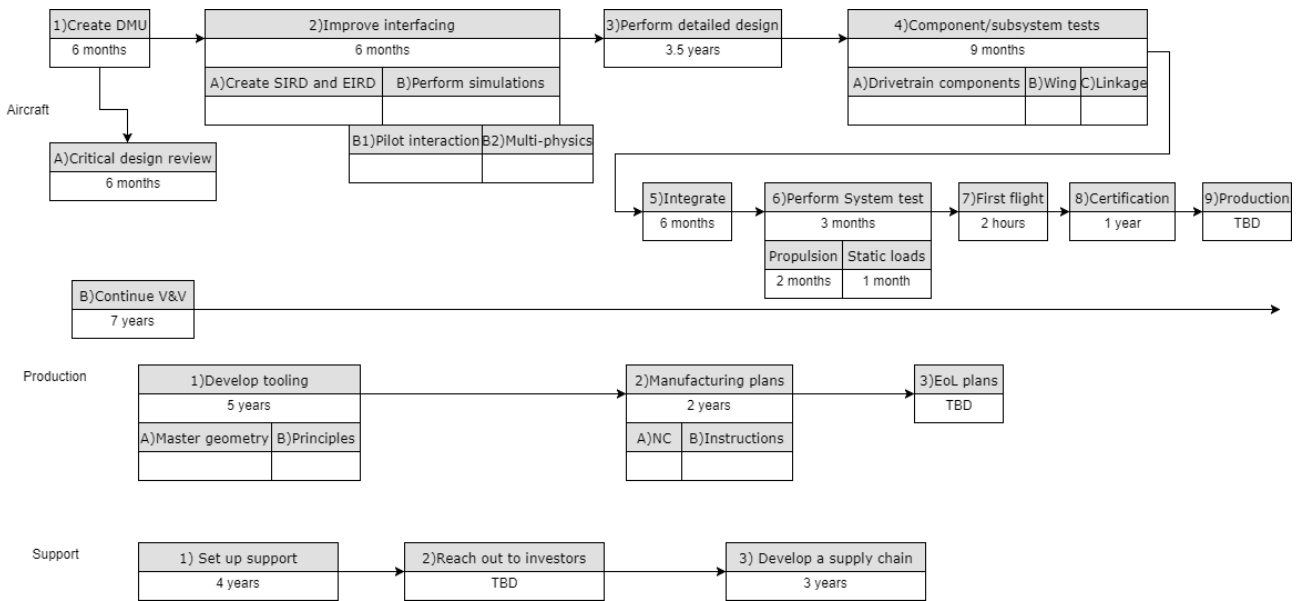


Figure 13.1: Project design & development logic.

SIRD is System Installation Requirements Document, EIRD is Equipment Installation Requirements Document. (Altfeld, 2010) DMU is Digital Mock-Up (which can be in SolidWorks or Catia.) The DMU has become a key concurrent engineering tool. This information gets shared to the departments and is updated regularly. With regular reviews, DMU allows validation of the product design, it ensures there is enough space, and that departments are on the same page regarding the design and its interfaces. Some stages may require some more explanation: "Integration" means the actual building of a testable model. "Support" are the airside resources, maintenance, and operations.

This future project development is also displayed in the form of a Gantt chart. This Gantt chart is shown in fig. 13.2

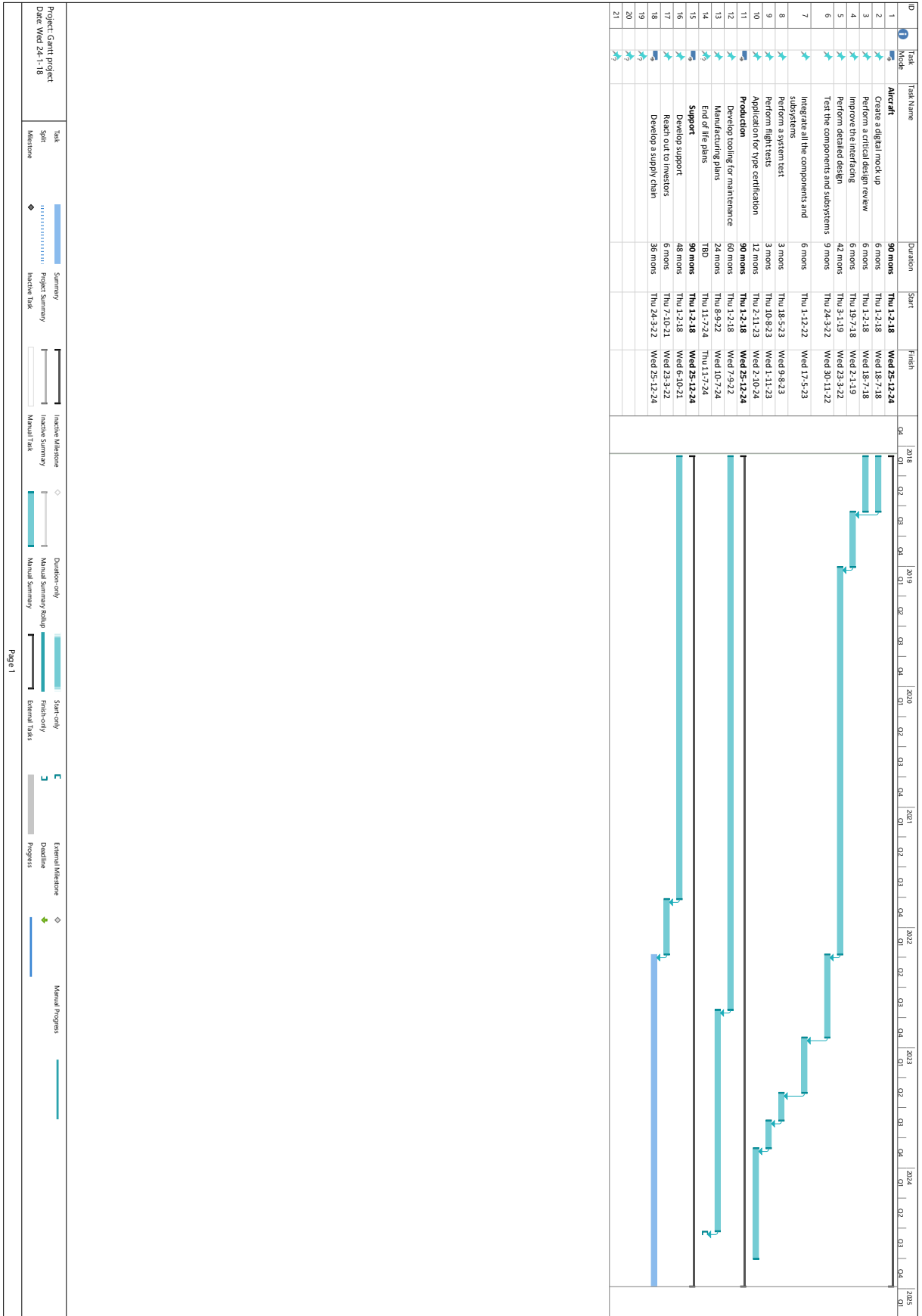


Figure 13.2: The project design and development logic in the form of a gantt chart

14

Conclusion

The aim of this project was to design an alternative concept for hybrid vehicles where the flight hardware is attached to a road vehicle at an airport. This concept has been presented as the Chesta. The design of the Chesta has been presented and discussed in this report. To see whether this aim has been met, it is necessary to review and gather the results.

The final design is a two-configuration vehicle that uses Distributed Electric Propulsion (DEP) and clip-on wings technology. The detachable flight hardware consists of the wings, the boom and the t-tail. Its automotive dimensions are 4.5 m, 1.85 m and 1.47 m in terms of length, width and height. This shows that it is much smaller in terms of size when comparing it to other hybrid vehicles, making it suitable for busier city traffic and using parking spaces. With the flight hardware attached, the new dimensions are 8.45 m, 11.96 m and 2.75 m in terms of length, width (wing span) and height. This shows that the wingspan is also longer than the competitors' as it is more optimised for flight. The current mass, however, is 1666 kg, which is 66kg above the budget. This can be improved through another iteration in the design phase in terms of structural design, materials, fuel capacity and electronics.

The wing has a surface area of 8.414 m^2 , an aspect ratio of 17, a root and tip chord of 0.782 m and 0.706 m and a leading edge sweep of 1.5° . The airfoil used in the wing is the NACA4418 and the airfoil used in the tail is the NACA0012. After analysing the aerodynamic characteristics due to DEP, it can be seen that it provides a good aerodynamic efficiency (L/D) at all flight configurations. The lift is much higher compared to the same flapped wing without DEP and the drag is much lower due to the slenderness of the wing, making it smaller than conventional wings. The overall drag of the aircraft however is higher due to the fuselage being car-shaped and not fully optimised for flight.

DEP also provides quiet performance and good optimisation opportunities. By utilising DEP propellers, the lift is greatly increased and the drag is decreased through the use of a smaller wing. A challenge for DEP is the landing condition; since thrust is used to create lift directly, the throttle can not be switched off before touchdown, leading to a larger landing distance of 462 m. This requires future research into means of creating drag, using different pilot technique or control augmentation, and utilisation of ground effect. The hybrid drive train allows for efficient operation both in the air and on the road, enabling the use of a smaller combustion engine. Challenges for the hybrid system in general is the power density of the battery, and design complexity. Range, speed, and takeoff distance comply with the requirements set.

Based on the packaging of the car and the final weights of the components, the operative empty weight centre of gravity of the full configuration was found to act at 38% of the fuselage length. A fully-movable tail was selected and this resulted in a horizontal tail surface area equal to 2.36 m^2 . From the directional and lateral stability and control analysis, the vertical tail surface has an area of 1.1 m^2 . This tail configuration is optimised for controllability during engine failure and landing with crosswind. The total tail has a weight of 31 kg.

The materials have been chosen for three parts of the vehicle: the truss structure, the wing and tail and the overall skin. Different kinds of aluminium and polyester with glass fibre shall be used. The wing box has been designed in such a way that it will not yield. The size of the wing is not optimal for the structural design of the wing which is why it turned out rather heavy at 200 kg. The wing will not yield during maximum load and will have a deflection of 0.2 m at the tip during cruise. The final design of the road hardware and tail will be a truss structure which is designed such that the

structure can withstand the ultimate manoeuvre loads. The simplified truss structure has a weight of 55.03 kg. The current designed four wedge shaped linkage lugs are as small and light as possible. Combined together, they weigh no more than 15 kg and the lugs shows no possible failure. Currently the threaded pins are considered the only fail point in bending. This shows that the linkage is up to the structural task. The linkage operation was designed around the advantages of using the wedge shape lugs, threaded pins and scaled-down train coupling. This helps insure a fast and autonomous linkage operation.

The integration of sustainable strategies, such as Cradle-to-Cradle and life cycle design throughout the DSE led to the use of environmentally friendly materials, and the use of E85 bio fuel. This reduces the environmental impact of flying by 70%. The shared use of the aircraft is also more sustainable than individuals owning the flight hardware. The aircraft complies on all sustainability requirements, with the only uncertainty being the recycling recovery rates for other means than traditional recycling, and the compliance to standards has to be determined in the post DSE phase.

There are uncertainties in the analysis of DEP. Assumptions have been made in terms of performance and aerodynamics. Further research and low-speed testing with DEP is needed to establish a more accurate representation of its effects on thrust, drag and lift. Computational Fluid Dynamics and wind tunnel testing is also recommended to visualise and analyse the fluid flow of the wing. More detailed weight estimations of the components should also be used to optimise the range of the position of the centre of gravity. Many assumptions were made in the structural analysis of the vehicle in order to make a first estimate of the structural performance. A more detailed analysis of the structural design should be conducted, preferably using the finite element method. Also, a full scale test of the major components needs to be conducted in order to test if the components can withstand the ultimate load case. As the coupling mechanism has never been used in aerospace application, further research into the adaptability and the integration of this mechanism should be performed. A full scale test of the linking method should also be conducted to check whether the linking method is indeed fail-safe.

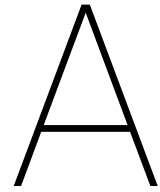
Bibliography

- Abbott, I. H. and A. E. V. Doenhoff
1959. *Theory of Wing Sections*. Dover Publications, INC. New York. Book.
- Ajaj, R. M.
2013. A conceptual wing-box weight estimation model for transport aircraft. *Aeronautical Journal*, Vol: 177 No 1191. Article.
- Altfeld, H. H.
2010. *Commercial Aircraft Projects*. Routledge. Book.
- Berdowski, Z. et al.
2009. Survey on standard weights of passengers and baggage. Technical report, EASA.
- Block, P. and G. L. Gentry Jr.
1986. Directivity and trends of noise generated by a propeller in a wake. Technical report, NASA Langley Research Center.
- Brezet, H. and C. van Hemel
1997. *A promising approach to sustainable production and consumption*. United Nations. Book.
- Bruhn, E.
1973. *Analysis & Design of Flight Vehicle Structures*. Jacobs Publishing, Inc. Book.
- Budynas, R. et al.
2010. *Shigley's Mechanical Engineering Design Ninth Edition*. McGraw-Hill Science/Engineering/Math. Book.
- CADDET Centre for Renewable Energy
1997. *Ethanol as an Aviation Fuel*. Technical brochure No.51.
- Dotz, T.
2011. Introducing the 787. Boeing slides.
- EASA
2010. Certification specifications for normal, utility, aerobatic and commuter category aeroplanes, CS-23 amendment 2. European Aviation Safety Agency. Regulations.
- Eastlake, C. N. and H. W. Blackwel
1999. Cost Estimating Software for General Aviation Aircraft Design. Paper presented at 2000 Annual ASEE Conference.
- EC
2005. DIRECTIVE 2005/64/EC on the type-approval of motor vehicles with regard to their reusability, recyclability and recoverability and amending Council Directive 70/156/EEC.
- Filipone, A.
2000. Data and performances of selected aircraft and rotorcraft. Technical report, Department of Energy Engineering, Technical University of Denmark.
- Hess, R. and H. Romanoff
1987. Aircraft airframe cost estimating relationships: All mission types. Technical report, The United States Air Force.
- Hettema, A.
2015. Vertical tail design, development of a rapid aerodynamic analysis method. Technical report, Technical University of Delft.

- Hibbeler, R.
2010. *Engineering Mechanics Statics 12th edition*. Pearson. Book.
- Hibbeler, R.
2011. *Mechanics of Materials 8th edition*. Pearson. Book.
- Holden, J. and N. Goel
2016. Fast-forwarding to a future of on-demand urban air transportation. Technical report, Uber.
- Howe, M.
1978. A review of the theory of trailing-edge noise. Technical report, NASA.
- JRC
2010. *International Reference System Life Cycle Data System (ILCD) Handbook 1st edition*. European Commission, Joint Research Center, European Platform for Life Cycle Assessment. Book.
- Koolstra, H.
2017. *Preventing Loss of Aircraft Control: Aiding pilots in manual recovery from roll-limited situations*. Delft University of Technology. Book.
- Kundu, A. K.
2010. *Aircraft Design*. Cambridge Aerospace Press. Book.
- LaRocca, G.
2017a. Systems Engineering and Aerospace Design (AE3211-I): Requirement Analysis and Design principles for A/C stability and control (Part 1). Delft University of Technology, Faculty of Aerospace Engineering. Lecture slides.
- LaRocca, G.
2017b. Systems Engineering and Aerospace Design (AE3211-I): Requirement Analysis and Design principles for A/C stability and control (Part 2). Delft University of Technology, Faculty of Aerospace Engineering. Lecture slides.
- LaRocca, G.
2017c. Systems Engineering and Aerospace Design (AE3211-I): Weight estimation and iterations in A/C design. Delft University of Technology, Faculty of Aerospace Engineering. s.
- Lotus Cars
2010. Vehicle mass reduction opportunities. Conference slides.
- Lutsey, N. P.
2010. Review of technical literature and trends related to automobile mass-reduction technology. Technical report, California Air Resources Board.
- Megson, T.
2007. *Aircraft Structures for Engineering Students 4th edition*. Elsevier. Book.
- Molenaar, C.
2015. *Why Customers Would Rather Have a Smartphone than a Car*. Taylor & Francis Ltd. Book.
- Moore, M. D.
2012. Distributed Electric Propulsion (DEP) Aircraft. NASA slides.
- Mulder, J., W. van Staveren, J. van der Vaart, E. de Weerd, C. de Visser, A. in 't Veld, and E. Mooij
2013. *Flight Dynamics*. Delft University of Technology. Course reader.
- Nita, M. and D. Scholz
2012. Estimating the Oswald Factor from Basic Aircraft Geometrical Parameters. Hamburg University of Applied Sciences. Lecture slides.
- O'Boy, D. J. and S. J. Walsh
2016. Automotive tyre cavity noise modelling and reduction. Technical report, Department of Aeronautical and Automotive Engineering, Loughborough University. Presented at Inter-Noise 2016, Hamburg.

- Pardessus, T.
2004. Concurrent engineering development and practices for aircraft design at airbus. ICAS 24TH International Congress of the Aeronautical Sciences. Scientific paper.
- Petermaier, K.
2015. Electric propulsion components with high power densities for aviation. Technical report, Siemens.
- Raymer, D. P.
1999. *Aircraft Design: A Conceptual Approach 3rd edition*. AIAA Education Series. Book.
- Roskam, J.
1997a. *Airplane Design Part I: Preliminary Sizing of Airplanes*. DARcorporation. Book.
- Roskam, J.
1997b. *Airplane Design Part II: Preliminary Configuration Design and Integration of the Propulsion System*. DARcorporation. Book.
- Roskam, J.
1997c. *Airplane Design Part VII: Determination of Stability, Control and Performance Characteristics*. DARcorporation. Book.
- Roskam, J.
2000a. *Airplane Design Part IV: Layout of Landing Gear and Systems*. DARcorporation. Book.
- Roskam, J.
2000b. *Airplane Design Part VI: Preliminary Calculation of Aerodynamic, Thrust and Power Characteristics*. DARcorporation. Book.
- Roskam, J.
2002. *Airplane Design Part VIII: Airplane Cost Estimation: Design, Development, Manufacturing and Operating*. DARcorporation. Book.
- Roskam, J.
2003. *Airplane Design Part V: Component Weight Estimation*. DARcorporation. Book.
- Ruijgrok, G. J.
2009. *Elements of airplane performance*. Delft Academic Press. Book.
- SAE International
2016. *Aerodynamic Testing of Road Vehicles - Testing Methods and Procedures*. Manual.
- Sinke, J., C. Vermeeren, and O. Bergsma
2004. *AE2-600 Materials & Manufacturing 2*. Delft University of Technology. Course reader.
- Slingerland, R.
2005. Prediction of tail downwash, ground effect and minimum unstick speed of jet transport aircraft. Technical report, Delft University of Technology.
- Smyth, R.
2006. Design and Development of Transport Aircraft Systems. Airbus slides.
- Steenhuizen, D. and A. Elham
2015a. AE2111-II aerospace design and systems engineering elements II: Wing design (part 3). Delft University of Technology, Faculty of Aerospace Engineering. Lecture slides.
- Steenhuizen, I. D. and D. A. Elham
2015b. AE2111-II aerospace design and systems engineering elements II: Wing design (part 2). Delft University of Technology, Faculty of Aerospace Engineering. Lecture slides.
- Stoll, A. M. et al.
2014. Drag reduction through distributed electric propulsion. Technical report, NASA.

- Stoll, A. M. et al.
2015. Comparison of cfd and experimental results of the leaptech distributed electric propulsion blown wing. Technical report, NASA.
- Torenbeek, E.
1982. *Synthesis of Subsonic Airplane Design*. Delft University Press. Book.
- Vogtländer, J.
2017. Idemattapp 2017. Online database.
- Vogtländer, J. G.
2014. *A practical guide to LCA for students, designers and business managers*. Delft University of Technology. Book.
- VOITH
2012. *Automatic Scharfenberg Coupler 010.616*. VOITH turbo Scharfenberg GmbH&Co. KG. User manual.
- Vos, R., J. Melker, and B. Zandbergen
2017. A/C Preliminary Sizing. AE1222 Aerospace Design and System Engineering Elements. Delft University of Technology, Faculty of Aerospace Engineering. Lecture slides.
- Voskuijl, M.
2016. AE2230-I Flight and Orbital Mechanics. Delft University of Technology, Faculty of Aerospace Engineering. Lecture slides.
- Williams, J. et al.
1978. The USAF stability and control digital datcom. Technical report, Wright-Patterson Air Force Base, Ohio.
- Yong, L., W. Xunnian, and Z. Dejiu
2013. Control strategies for airframe noise reduction. *Chinese Journal of Aeronautics*, vol:26;pages:249–260. Article.



Reference Aircraft Data

Table A.1: General aircraft aerodynamic characteristics

Aircraft	Gulfstream II	Gulfstream III	SR-22	Cessna Citation II	Average
C_L	0.45	0.45	0.3	0.419	0.405
C_D	0.0305	0.0262	0.0273	0.0584	0.0356
L/D	14.75	17.18	11	7.18	12.53

Table A.2: Reference aircraft lift data

Aircraft	B737-800	A320	B787-800	A380	A330-200	B777-200	B757-200	Average
C_L (Take-off)	1.09	1.01	1.10	1.18	1.03	0.958	0.892	1.04
C_L (Cruise)	0.56	0.466	0.51	0.586	0.538	0.484	0.428	0.510
C_L (Landing)	1.47	1.23	1.25	1.20	1.03	1.03	1.18	1.20

Table A.3: Reference aircraft drag data

Aircraft	B737-800	A320	B787-800	A380	A330-200	B777-200	B757-200	Average
C_D (Take-off)	-	-	-	-	-	-	-	-
C_D (Cruise)	0.065	0.053	0.055	0.021	0.038	0.035	0.03	0.0424
C_D (Landing)	0.080	0.061	0.065	0.06	0.052	0.051	0.062	0.0616

B

EcoDesign Strategy Wheel

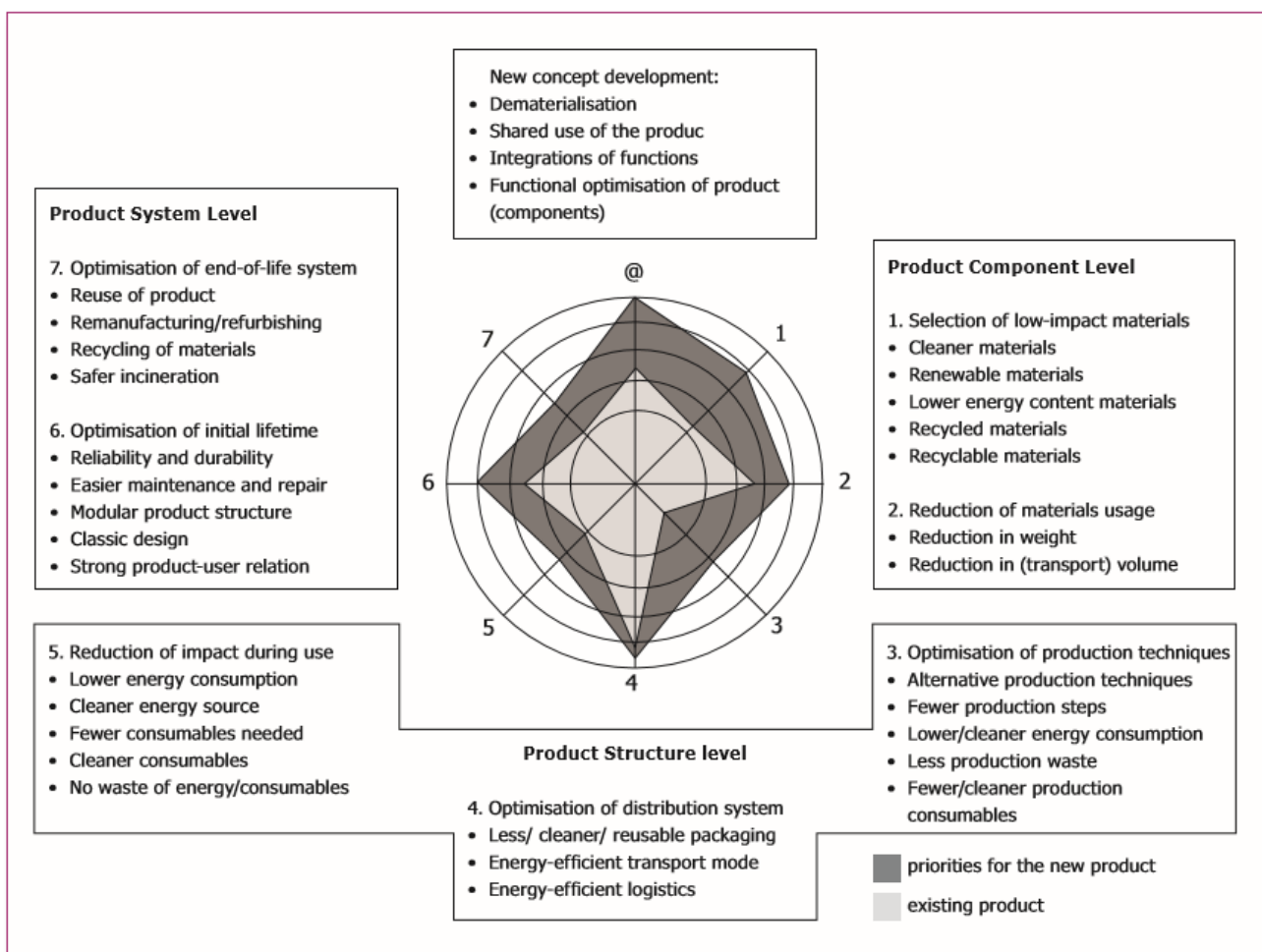
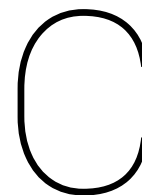


Figure B.1: The EcoDesign Strategy Wheel (Brezet and van Hemel, 1997)



Work Division

Name	Main written parts in report
Martin Ponson	Major functionalities, Electrical linkages, Flight Hardware structure, linkage design, Linkage lugs, Effect of aspect ratio on linkage, Linkage Operations, Further research FH structure and linkage design
Wessel Keijer	Propeller design, Noise performance, V-n diagrams, all SolidWorks renderings, The Final Product
Myra Nelissen	Materials, Wing box structure, Part manufacturing, Assembly, sensitivity analysis & recommendations for wing and materials
Sakariye Gudaal	Summary, Introduction, List of Requirements, Electrical System, Electrical Linkages, Aerodynamics, Compliance Matrix, Technical Sensitivity Analysis (Effect on Aerodynamics), Further Research and Recommendations (Aerodynamics), Conclusion
Mathieu Blanke	Market Opportunities, Linkage pins and threads, Operations, business case sections 1,2 & 3, Final Design (powertrain, structures, linkage)
Mark Huijstra	Market Opportunities, Aerodynamics (Airfoil Selection, Drag calculations, Verification), Business case, Financial Strategy, Final Product, Further Research and Recommendations
Juul Jongbloed	Directional and Lateral Stability and Control
Lindsay Veldkamp	Road Hardware structure, Car Suspension & Landing Gear, Technical Risk Assessment, Certification approach for linkage, Recommendations and Further Research for truss structure
Lars van der Heijden	Centre of Gravity Location, Longitudinal Stability and Control, Effect of aspect ratio on Horizontal Tail Size, Verification and Certification of the Product, Further research stability and Control, Data handling System
Pieter van Zelst	Flight performance and propulsion (Every section except flight envelope, noise performance and propeller design), Technical Resource allocation, System Sustainability, End of Life cycle and recycling, Project design and Development logic, sensitivity: effects on flight performance

Table C.1: Work Division